Tuning Surface Wettability Through Volumetric Engineering

by

Viraj Damle

A Dissertation Presented in Partial Fulfillment
of the Requirements for the Degree
Doctor of Philosophy

Approved December 2016 by the
Graduate Supervisory Committee:

Konrad Rykaczewski, Chair
Patrick Phelan
Jerry Lin
Marcus Herrmann
Robert Wang
Liping Wang

ARIZONA STATE UNIVERSITY

May 2017

ABSTRACT

Many defense, healthcare, and energy applications can benefit from the development of surfaces that easily shed droplets of liquids of interest. Desired wetting properties are typically achieved via altering the surface chemistry or topography or both through surface engineering. Despite many recent advancements, materials modified only on their exterior are still prone to physical degradation and lack durability. In contrast to surface engineering, this thesis focuses on altering the bulk composition and the interior of a material to tune how an exterior surface would interact with liquids. Fundamental and applied aspects of engineering of two material systems with low contact angle hysteresis (i.e. ability to easily shed droplets) are explained. First, water-shedding metal matrix hydrophobic nanoparticle composites with high thermal conductivity for steam condensation rate enhancement are discussed. Despite having static contact angle <90° (not hydrophobic), sustained dropwise steam condensation can be achieved at the exterior surface of the composite due to low contact angle hysteresis (CAH). In order to explain this observation, the effect of varying the length scale of surface wetting heterogeneity over three orders of magnitude on the value of CAH was experimentally investigated. This study revealed that the CAH value is primarily governed by the pinning length which in turn depends on the length scale of wetting heterogeneity. Modifying the heterogeneity size ultimately leads to near isotropic wettability for surfaces with highly anisotropic nanoscale chemical heterogeneities. Next, development of lubricant-swollen polymeric omniphobic protective gear for defense and healthcare applications is described. Specifically, it is shown that the robust and durable protective gear can be made from polymeric material fully saturated with lubricant that can shed all liquids irrespective of their surface tensions

even after multiple contact incidences with the foreign objects. Further, a couple of schemes are proposed to improve the rate of lubrication and replenishment of lubricant as well as reduce the total amount of lubricant required in making the polymeric protective gear omniphobic. Overall, this research aims to understand the underlying physics of dynamic surface-liquid interaction and provides simple scalable route to fabricate better materials for condensers and omniphobic protective gear.

To

Aai, Baba and Yoshita,

ACKNOWLEDGMENTS

At this point I can definitely say that I made the right choice three years back to come to ASU to pursue my PhD. It has been a fantastic journey. First of all, I would like to thank scientific support staff, office staff, and the entire ASU community for their wonderful support and encouragement.

I consider myself lucky that I got an opportunity to conduct my Doctoral research in Dr. Konrad Rykaczewski's research group. He has been nothing but a genuinely good adviser and a wonderful human being to me for the past three and half years. Surface wettability and 'how to conduct scientific research' are only a couple among the many other things I learnt from him. Working with him made this journey joyous! I definitely want thank my Doctoral committee members as well for their valuable inputs in my research. I would also take this opportunity to convey my sincere thanks to Dr. Maria Wieczynska for always being very kind to me (and for all the wonderful pastries). I am really thankful to the entire Rykaczewski research group for their support; especially, Dr. Xiaoda Sun who has been more than colleague to me.

I don't know what to say about my Mom and Dad but I will forever be grateful to them. Me getting a PhD was never 'my' dream, but it was 'our' dream. So it was never me alone who worked hard so that I can reach this milestone one day, but we, as a team, worked hard for more than last two and half decades because of which I have been able to complete my PhD successfully. There were times when giving up a career in science never looked impossible. But purely because of my parents' support and love I got strength to fight against all odds and carry on. There is another person to whom I will not thank: my better half Yoshita. She has witnessed this enjoyable yet demanding journey very closely with

me. She has supported me through all ups and downs and she has been a perfect partner one can hope to have in every aspect while I was on this endeavor. I am also sincerely grateful to my parents-in-laws for their unfading support.

Getting a PhD is never just about doing research and attending classes in graduate school for three years. It is moreover a culminating event of efforts and contributions from every individual at least a decade before that. I am honestly thankful to each and every person who contributed in my success in any way. But specially I would like to express my gratitude towards Bhooshan dada and Pallavi tai. May be it would have been a different story today have I not met them seven years back.

Close friends have always been an integral part of my life. They play a crucial role in my academic success. It's impossible to write everybody's name, but I really thank them from the bottom of my heart for being with me. Here, I would like to appreciate and not thank 'my family in the US' who was with me through all thick and thins. I cannot imagine myself in a graduate school in America without Shriniket, Devika, Herschel, Mugdha and Vinay being in this country. They have helped me in every possible way for the last three and half years. During my graduate school, I found three amazing new friends- Tanvi, Raja and Indira Gadgil who made my stay in Tempe extremely pleasant.

Finally, I feel honored to be in debt of all the elderly in my family and Maharaj for their blessings which has enabled me to successfully finish my PhD.

TABLE OF CONTENTS

Page

CHAPTER Page

CHAPTER Page

LIST OF TABLES

LIST OF FIGURES

Figure Page

Figure Page

Figure Page

Figure Page

CHAPTER 1

INTRODUCTION

1.1 Surface Wettability

Many engineering, healthcare and other applications require detail understanding of droplet-surface interaction. In a simplified view, these interactions can be boiled down to the question: when a droplet comes in contact or is condensed on a surface, does it stick or slip away? This phenomenon is governed by wetting properties of the surface that stem from liquid surface interaction. Specifically, it depends on the chemistry and topography of a surface and surface tension of the fluid. If size of a drop resting on a surface is below the capillary length (i.e. the length at which hydrostatic pressure and Laplace pressure inside the drop are equal) surface tension dominates over gravity and the shape of the drop assumes a spherical cap shape. As such, the drop geometry can solely be described using base radius and contact angle between the surface and liquid-air interface at the drop's perimeter. This so called equilibrium or static contact angle (θ) is a well-established measure to quantify surface wettability. If the contact angle is finite ($0°<\theta<180°$), the liquid partially wets the surface. In turn if static contact angle of a water drop is below and above 90°, the surfaces are referred to as hydrophilic and hydrophobic, respectively. Figure 1.1a shows the schematic of hydrophilic and hydrophobic surface.

Adhesion of a droplet to a surface can be independent of the surface's equilibrium contact angle. For example, in many cases water droplet may stick to a hydrophobic surface, even if it is placed vertically. In contrast, drop of ethanol on a lubricated nanotextured surface will have an equilibrium contact angle below 50°, but will slide off if the sample is titled just a few degrees. This surface tilt angle can be used as a measure

of a liquid's adhesion to the surface. Another common way to quantify "possibility of droplet sliding on the given surface" is the contact angle hysteresis (CAH). As shown in Figure 1.1b, CAH is defined as the difference between contact angle that the liquid makes while advancing on the surface (θ_a) and the contact angle that it makes while receding from the surface (θ_r). Surfaces with high CAH are "sticky" whereas those surface is low high CAH facilitate droplet shedding/rolling.

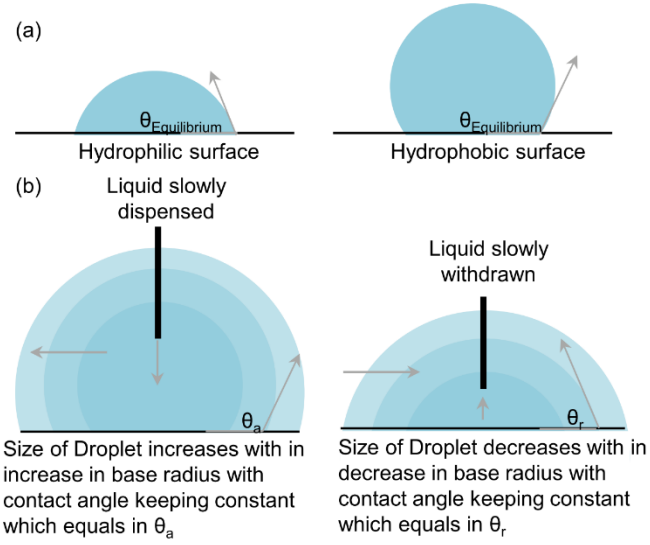

Figure 1.1 Schematic showing the difference between (a) hydrophilic-hydrophobic surface and (b) advancing-receding contact angle

On a flat surface, contact angle hysteresis evolves from the chemical and/or topographical imperfections on the surface. Whenever a droplet moves across a surface, three phase contact line (i.e. the perimeter of the droplet) pins at such heterogeneities. This causes a deviation in local contact angle from the equilibrium contact angle. This deviation is quantified in terms of contact angle hysteresis[1,2]. This explains why a chemically homogeneous rough surface offers more pinning sites, and thus has higher CAH, as compared to flat surface with similar chemical composition. Wenzel, in 1936, recognized

that in addition to altering CAH, surface roughness also changes equilibrium contact angle (θ) [3]. This modified 'apparent' contact angle (θ*) can be obtained by $cos\theta^* = r\,cos\theta$, where r is the ra (r=1 and r>1 for flat surface and rough surface respectively). Therefore, if a hydrophobic (θ>90° ~ Cosθ<-1) or hydrophilic (θ<90° ~ Cosθ<1) flat surface becomes rough, then it becomes further hydrophobic (θ*> θ) or hydrophilic (θ*< θ) respectively.

Surfaces with high CAH are undesired in many applications and surface engineering is used to reduce the CAH. These changes can include both alterations to the surface topography and surface chemistry. For example, nano/microscale pillars can be added to a hydrophobic surface so that when a water droplet is placed on such surface air pockets are trapped underneath it. This type of surface engineering reduces the CAH by solid-liquid contact at the perimeter of the drop as well as in the base area (see Figure 1.2d). This wetting state is referred to as superhydrophobic Cassie-Baxter state (θ>150° and CAH<10°). However, majority of liquids have a much lower surface tension than water, thus will have an equilibrium contact angle lower than 90° on most surfaces. Consequently, they will wet majority of superhydrophobic surfaces. In order to be omniphobic, textured surfaces must have re-entrant geometry[4,5]. However, in certain situations such as condensation or high velocity droplet impingement, droplet of any liquid will penetrate and wet the surface textured becoming pinned. For water drops on such surface will still have a high static contact angle, but have a very high CAH. This highly "sticky"' wetting condition shown in Figure 1.2b is known as the Wenzel state. To overcome this drawback, air pockets are sometimes replaced with liquid immiscible lubricant (Figure 1.2c)[6,7]. In this situation, termed often as Lubricant Impregnated Surface (LIS), droplet of almost any

liquid immiscible with the lubricant has a very low CAH because it is mostly in contact with the atomistically smooth lubricant surface.

Below, application of low CAH materials for steam condensation rate enhancement is described followed by fundamentals of droplet perimeter- surface interaction that is crucial in governing the droplet movement across the surface. Next application of low CAH materials for self-cleaning or easy to decontaminate protective fabrics for military and healthcare fields is described. Furthermore, necessity of rapid lubrication and re-lubrication methods for such materials is discussed.

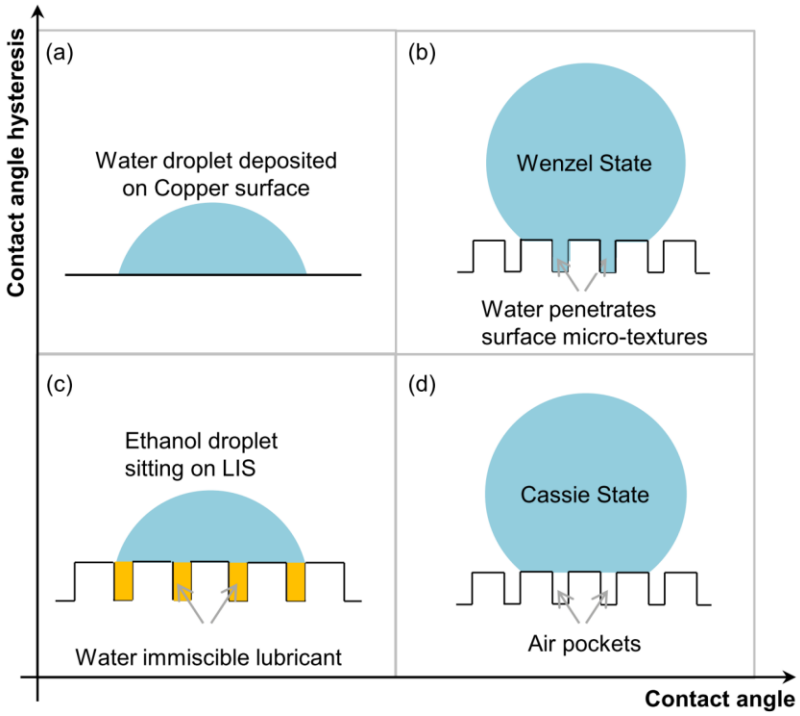

Figure 1.2 Schematic shows the droplet shape and corresponding wetting state for surfaces having (a) low CA- high CAH (b) high CA- high CAH (c) low CA- low CAH and (d) high CA and low CAH

1.2 Heat Transfer Enhancement by Promoting Dropwise Condensation

Steam condensers are fundamental components of about 85% of electricity generation plants and 50% of desalination plants installed globally.[8] As a consequence, finding routes to even moderately improve efficiency of the condensation process could lead to considerable economic savings as well as environmental and societal benefits. Two primary external condensation modes are filmwise (FWC) and dropwise (DWC). Promoting the condensation in dropwise mode improves the condensation heat transfer rate by preventing formation of a thermally insulating water film. Additionally, if the surface is mounted vertically then smaller spherical-cap shaped droplets coalesce and shed under gravity thus exposing more "bare" surface for condensation to occur on. Classically, only hydrophobic surfaces were thought to promote dropwise condensation. Recently, Rykaczewski et al[9] have demonstrated that this assumption is not necessarily true. Specifically, the authors demonstrated dropwise condensation on omniphobic surfaces of variety of low surface tension liquids that had $\theta<90°$ but low CAH<30°. In other terms, surface with low CAH will maintain DWC by facilitating droplet shedding prior to surface flooding.

On a flat surface, condensation takes place in four stages: (1) nucleation (2) growth of individual drops through direct vapor deposition followed by (3) growth dominated by droplets' coalescence and for titled surfaces (4) gravity-aided shedding. Sustained DWC or transition of FWC to DWC is primarily dependent on droplets coalescence dynamics during third stage of the condensation process. Specifically, on surface with high CAH, three phase contact line does not retract post coalescence. Thus coalesced drop primarily covers the outline of the droplets prior to coalescence. This leads to formation of water

puddle that ultimately results in transition of DWC to FWC. In the case of surfaces with low CAH, contact line retracts post coalescence. Thus, spherical cap shape of coalescing drops is maintained post coalescence which leads to sustained DWC. Hence low CAH surface not only assists droplet shedding under gravity but also promotes sustained DWC via inhibiting DWC to FWC transition. In order to engineer such durable surfaces with low CAH for dropwise condensation application, careful investigation of droplet surface interaction is essential.

1.3 Effect of Surface Heterogeneity on Wettability

Controlling of water droplet motion on a surface is important for facilitating or improving the efficiency of many applications such as anti-icing or condensation.[10–17] The resistance a drop poses to motion, typically quantified by the contact angle hysteresis (CAH), is thought to be dominated by the composition of the surface at the three phase contact line (TPCL). Specifically, the surface composition alters the CAH by changing the shape of this contact line.[18–20] Yet, despite of having been imaged already four decades back,[21] it is only recently that studies have began quantifying the effects of contortions in the TPCL. Specifically, role of TPCL contortions in reducing the depinning threshold[22] and effective adhesion[23] was recently pointed out.

Although the impact of micro-scale contortions on the value of the CAH has been recognized, effect of number and shape of these contortions that depend on the length-scale of the surface heterogeneity[24] is still largely unknown. Simply altering heterogeneity length-scale for instance from micro to nano-scale will increase the number of kinks per unit length of the TPCL by three orders of magnitude. Thus, surfaces with micro and nanoscale chemical or topographical heterogeneity can have significantly different CAH

despite having similar static wettability. Hence, there is a need to systematically investigate the effect of number of contortions in the TPCL on the CAH value.

1.4 Omniphobic Protective Gear

Personal protective gear used in healthcare and military applications is intended to separate a person from hazardous fluids in the surrounding because their penetration into the suit could have dire consequences. For example, human contact with even a small volume of liquid contaminated with biological threats such as the Ebola virus or chemical weapon agents (CWAs) such as Sarin can be deadly.[25,26] Both of these liquids pose a threat not only as macroscale drops but also as aerosols with microscale droplets.[25,26] In addition, Sarin and other types of CWAs are low surface tension organic liquids with a low vapor pressure (i.e., they can wet majority of common materials and do not evaporate readily, so they are likely to remain in liquid phase).[25] As a result, by staying on surfaces, CWA micro-droplets can readily be absorbed into different types of materials. Consequently, slow off-gassing of these dangerous chemicals from contaminated gear away from the direct exposure zone also poses a major health threat.[27,28] Thus, use of personal protection gear made from low CAH omniphobic materials that easily shed droplets of all sizes could provide enhanced protection from most hazardous liquids irrespective of their surface tension within a direct exposure zone, as well as facilitate post-exposure decontamination of the gear.

1.5 Rapid Replenishment of Lubricant in LIS

Liquid infused surfaces (LIS) consist of a porous or textured solid matrix infused with a lubricating liquid.[1–3] The presence of a thin film of the lubricant on the exterior surface dramatically facilitates shedding of a wide range of liquids and solids, making LIS

potential candidates for a variety of applications. However, recent studies have shown that loss of the lubricating liquid leads to degradation of the low adhesion characteristic of LIS. Consequently, before LIS can transition into industrial use, durability issues posed by lubricant loss need to be addressed and a scalable lubricant replenishment system is needed to sustain LIS performance through periodic re-lubrication.

1.6 Thesis Layout

Chapters 2 through 5 discuss the details of the research conducted, while Chapter 6 summarizes this dissertation and proposes the potential routes for future research. Specifically, Chapter 2 describes investigation of water condensation mode and wetting properties of mimicked metal matrix-hydrophobic nanoparticle composites with varied quantity of the hydrophobic phase. Next, studies on analyzing the dependency of surface wettability on length scale of surface heterogeneity is elaborated in Chapter 3. Chapter 4 describes simple scalable route to make durable omniphobic protective gear using lubricant impregnated fabric supported polymeric film. Further in Chapter 5, schemes for rapid and economical lubrication and re-lubrication of polymeric omniphobic protective gear are proposed. Lastly, Chapter 6 summarizes the research conducted along with the recommendations for future research.

CHAPTER 2

CAN METAL-MATRIX HYDROPHOBIC NANOPARTICLE COMPOSITES ENHANCE WATER CONDENSATION BY PROMOTING THE DROPWISE MODE?

2.1 Introduction

Since the 1930s, hydrophobization of metal surfaces has been known to increase heat transfer during water condensation by up to an order of magnitude,[29] whereby this surface modification switches the condensation mode from filmwise (FWC) to dropwise (DWC). As shown in Figure 2.1a, promoting the latter condensation mode improves the heat transfer rate by preventing formation of a thermally insulating water film. However, use of hydrophobic coatings required to promote DWC introduces an additional resistance to heat flow (see Figure 2.1b). Thus, in simplified terms, to increase the total heat transfer rate, thermal resistance introduced by the hydrophobic coating must be significantly smaller than that posed by the water film during filmwise condensation. Unfortunately, most hydrophobic surface modifiers have a low thermal conductivity and limited durability. For example, to withstand a steam environment within a power plant condenser during the projected lifetime of the power station (~40 years), a Polytetrafluoroethylene (PTFE) film must be at ~20 to 30 μm thick.[30] The thermal resistance added by this thickness of the polymeric film negates any heat transfer enhancement attained by promoting DWC, explaining why this condensation mode is not common in industry.

While there are many techniques to render surfaces hydrophobic to promote DWC,[30–40]most of the produced coatings suffer from longevity issues. Recently, several alternative methods have been proposed to render surface hydrophobic including rare earth oxides,[41] grafted polymers,[8] and lubricant impregnated surfaces (LIS).[9,42–44] Nevertheless,

applying these materials as thin films makes them susceptible to variety of degradation issues which could include polymer oxidation at defect sites, ceramic film delamination and, for LIS, slow lubricant drainage with departing water drops.

Metal matrix composites with hydrophobic particles have been proposed as a durable alternative to thin film hydrophobic surface coatings (see Figure 2.1c).[45] In particular, polished copper-graphite microparticle composites were reported to have a macroscopic water drop contact angle of ~87°.[45] The surface of this composite has heterogeneous wetting properties consisting of microscale hydrophobic patches on a hydrophilic background. Condensation and wetting on surfaces with microscale chemical and topological heterogeneities has been studied extensively,[17,20,44,46–64] and surfaces comparable to those of the composites with microscale hydrophobic features have been demonstrated to flood during condensation.[59] This mismatch between macroscale wetting properties and condensation mode stems from the multiscale nature of the phase change process: (1) nucleation (l_n~1 to 100 nm) and (2) growth of individual drops through direct vapor deposition (l_i~100 nm to 5 μm) followed by (3) growth dominated by droplets' coalescence (l_c~5 μm to 3 mm), and for titled surfaces (4) gravity-aided shedding (l_c~1 to 3 mm). The transition between the second and third stage occurs when the average droplet diameter reaches the average center-to-center spacing between closest neighboring drops after nucleation (i.e. the drops that will coalesce with each other). While dependent on a number of variables such as supersaturation and surface chemistry/texture, the length at which this transition occurs, l_{co}, is typically in the range of ~5 to 10 μm.[65–68] Consequently, hydrophobic particles with size comparable or larger size than l_{co} will have no impact on growth of individual drops as well as their coalescence. In other terms, flooding of surfaces

with microscale hydrophobic features occurs because droplets smaller than these features nucleate, grow, coalesce, and ultimately transition into a film on the hydrophilic background surface surrounding the hydrophobic phase.

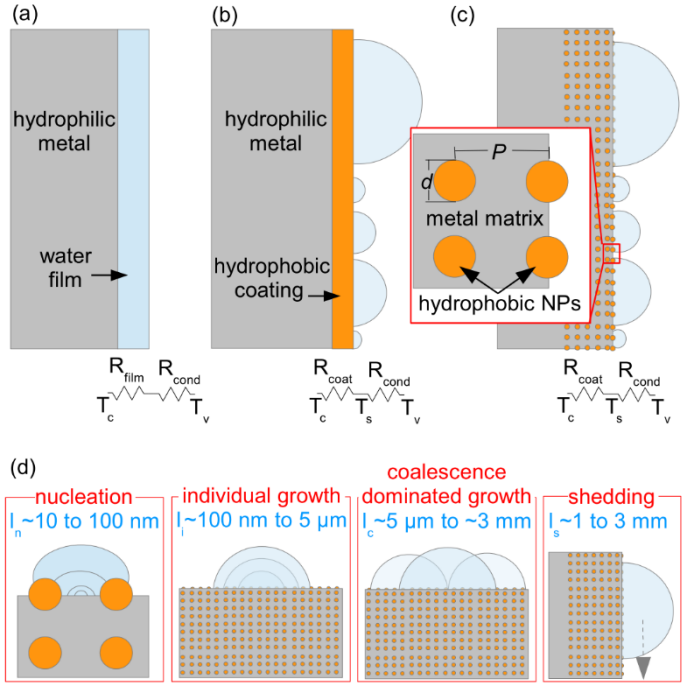

Figure 2.1 Schematic contrasting (a) filmwise condensation with (b) traditional method of promoting dropwise condensation using hydrophobic coating and (c) metal matrix-hydrophobic nanoparticle composites with nanoparticles with diameter d and pitch P; representative resistive heat transfer networks are also indicated with T_c, T_s, T_v, R_{film}, R_{coat}, R_{cond}, R_{comp}, and R_{cond} corresponding to bulk condenser, surface, and vapor temperatures and water film, hydrophobic coating, composite, and condensation thermal resistances, respectively; (d) schematics indicating length scales relevant to the four dropwise condensation stages.

In this thesis, it is proposed that flooding of composite surfaces during condensation can be prevented by engineering the materials on length scale greater than that of drop nuclei but significantly smaller than the average separation distance between closest neighboring microdroplet centers prior to onset of the coalescence dominated growth stage[65–68](l_{co}~5 to 10 μm[69]). In particular, the hypothesis was that dispersion of hydrophobic nanoparticles with diameters, *d*, much lower than l_{co} (i.e. *d* below ~500 nm) within the hydrophilic metal matrix will significantly disrupt individual droplet growth prior to as well as during onset of microdroplet coalescence (see schematic illustration in Figure 2.1c and 2.1d). In fact, the work by Lixin and co-workers demonstrated DWC on electrodeposited nickel-teflon nanoparticle coating. However, the lack of clear surface characterization makes it difficult to draw general conclusions about droplet dynamics in this early work.[70] This chapter describes theoretical and experimental exploration of how composition of metal matrix hydrophobic nanoparticle composites (MMHNPCs) affects droplet dynamics, effective thermal conductivity of the materials, and overall thermal transport during heterogeneous water condensation.

2.2 Experimental Methods

2.2.1 *Static and Dynamic Contact Angle Measurements*

A home-built goniometer composed of a stage 3D printed using Makerbot Replicator 2x, a CCD camera (Imaging Source DFK23U618) with high magnification lens (Navitar 6232A), a syringe pump (New Era Pump System NE-1000), and a diffuse light source (Dolan-Jenner MH-100), was used to measure the static and dynamic contact angles of water on all the fabricated specimens. For calculating the static contact angle, a 2 μL water drop was placed using a micro-pipette (Capp Bravo) on the sample. For each sample,

six different drops were dispensed, images were captured and analyzed to calculate the average static contact angle. Corresponding uncertainty values were calculated using a two-tailed T-student's distribution with 95% confidence interval. To measure the contact angle hysteresis, the liquid was gradually dispensed and retracted from tip of a syringe using the syringe pump. The specimen was kept on the stage and illuminated from the back via the diffused light source. Images captured during the experiment were stored and analyzed using ImageJ software.[27] Specifically, separate images were chosen to calculate six advancing (θ_{a1}, θ_{a2}, ..., θ_{a6}) and six receding (θ_{r1}, θ_{r2}, ..., θ_{r6}) contact angles. Average advancing and receding contact angle, θ_a and θ_r, respectively, were calculated using these values. The uncertainty values in θ_a ($\sigma_{\theta a}$) and θ_r ($\sigma_{\theta r}$) were calculated considering a two-tailed T-student's distribution with 90% confidence interval. Average contact angle hysteresis was later computed as $CAH = \theta_a - \theta_r$ with $\sigma_{CAH} = ((\sigma_{\theta a})^2 + (\sigma_{\theta r})^2)^{1/2}$.

2.2.2 *High Speed Imaging of Microscopic Condensation Dynamics*

To observe the microscopic coalescence dynamics, condensation experiments were performed under the optical microscope (Zeiss Axio-Zoom V16) and images were recorded using high speed camera (Photron Fastcam Mini UX-100) at 5000 fps. The experimental setup consisted of a glass humidity box with a custom acrylic top. Flow of nitrogen saturated with water was used to control the humidity around ~75 % ± 2%. The samples were cooled using a water-cooled Peltier element (Analog Technologies). The surface temperature was measured using a K-type thermocouple connected to data logger and was controlled by adjusting input current for the Peltier element. Temperature, relative humidity, and air velocity inside the box were recorded using (EK-H5 Sensirion) and

(Accusense UAS Sensor (UAS1100PC), Degree Controls, Inc), respectively. Images captured using high speed camera were post-processed using PFA (v1.2.0.0) software.

2.2.3 *Imaging of Steady-State Condensation Dynamics on Vertically Mounted Samples*

The Peltier element cooled with flow of cold water supplied by circulating chiller (AP28R-30-V11B, VWR) was held vertically using the 3D printed mount in the environmental chamber set at 25°C ± 1°C and 92% ± 3%. The specimens were attached to the Peltier element using thermal grease (TG-2, Thermaltake). To determine the droplet departure radii steady-state condensation experiments were conducted for at least 1h for each sample. The sample temperature was monitored and controlled in same way as described in Section 4.2.2. The surface subcooling was adjusted to ~20 to 25 K. Images of the condensation process were captured with 1 s interval using DFK 23UP031 camera (ImagingSource) with 3.5-10.5 mm lens (Computar). The droplet departure radius was calculated by analyzing the captured images using ImageJ software. Specifically, six pre-drop departure images were chosen to measure the departure diameter of the liquid droplet. In the event of multiple droplets with diameter d_1, d_2…, d_n, having volume v_1, v_2.. v_n, merging to form a bigger shedding drop, volume of the departed drop was set to $v_1+v_2+\ldots+v_n$. The diameter of the detached drop was then calculated from using this volume assuming a spherical cap geometry with $v = \frac{\pi(R/\cos\theta)^3}{3}(1-\cos\theta)^2(2+\cos\theta)$ as given by Whyman et al. (where θ is the static contact angle R is the base radius of the liquid droplet).[28]

2.2.4 *Sample Characterization and Post Processing of Images*

The fabricated samples were characterized using SEM (FEI XL-30 with field emission gun) and AFM (Bruker Dimension). Specifically, AFM images were recorded for

each sample over the area 5μm x 5μm and 10μm x 10μm. The captured images were analyzed using Nanoscope Analysis v1.40 (Bruker Corporation) to quantify the diameters and the spacing of the nanospheres. In particular, ~30 measurements of the inter-spherical center-to-center distance along the row of nanospheres (a), the distance between neighboring spheres in the parallel rows (b), and the diameter of the spheres (d) were recorded. Based on these 30 data points, average values a_{avg}, b_{avg}, d_{avg} with corresponding the standard deviations σ_a, σ_b, and σ_d were calculated. The 'b' parameter is roughly governed by the Thorlabs master gratings spacing whereas the 'a' distance is determined by the dynamics of dewetting induced by heating the thin film of PTFE precursor solution spin coated on the silicon wafer above the glass-transition temperature. Using these three parameters, surface fraction of nanospheres was translated into volume fraction (vf) of the mimicked MMC using $\frac{4}{3}\pi(\frac{d}{2})^2/ab\frac{a+b}{2}$. In turn, the corresponding uncertainty of the volume fraction was calculated as $\sigma_{vf} = \sqrt{(\frac{\partial vf}{\partial a}\sigma_a)^2 + (\frac{\partial vf}{\partial b}\sigma_b)^2 + (\frac{\partial vf}{\partial d}\sigma_d)^2}$. In addition to the AFM characterization, SEM images were captured to confirm the uniform fabrication of the nanospheres across the entire 1 cm^2 substrate area.

2.3 Results and Discussion

2.3.1 *Surface Wetting and Bulk Thermal Conductivity Vs. Composite Composition: Theoretical Considerations*

Hydrophilic surfaces with millimeter scale hydrophobic patterns were first explored for condensation heat transfer enhancement by Tanaka and co-workers.[71] More recent work has focused on wetting[20,46,47,50–52] and condensation[17,44,52–64] of surfaces with both chemical and topological microscale features. The Cassie-Baxter equation is

commonly used to predict the apparent contact angle of water droplets, θ_c, sitting on such surfaces.[24,72] In particular, the $cos\theta_c = \sum_{i=1}^{i_{max}} f_i cos\theta_i$ where f_i and θ_i, are the liquid-solid interfacial area per unit plane base area and the water contact angle of individual phases present on the surface (subscript s, a, and r are used for static, advancing, and receding contact angles and H and M for hydrophobic and matrix phases, respectively). For spherical hydrophobic particles with θ_{Hs}~100° (e.g. PTFE or ceria[41]) with diameter (d) distributed uniformly on corners of a cubic lattice with a center-to-center pitch (P), a hydrophobic composite is achieved for a P/d (nanoparticle volume fraction) of 1.15 (0.34) and 1.35 (0.2) for copper and aluminum matrices with θ_{Ms}~60° and 80°, respectively. The corresponding effective thermal conductivities estimated using Maxwell's formula for copper matrix is k_{eff}~180 W/mK, which is dramatically higher than that of PTFE (~0.25 W/mK) or ceria (~17 W/mK) and comparable to pure aluminum (~200 W/mK). Thus, according to these calculations MMHNPC could provide the highly desired high thermal conductivity hydrophobic materials for improved condensation.

Nevertheless, the predictions of thermodynamic models of composite surfaces' static contact angles often do not correspond to condensation behavior. For example, macroscopically superhydrophobic surfaces can be easily flooded by water condensate and careful nanoengineering is required to promote DWC on those surfaces.[61,69,73–89] Furthermore, Anand et al.[43] and Rykaczewski et al.[9] recently demonstrated DWC of water and wide array of low surface tension liquids with static contact angles significantly below 90°, but with very low contact angle hysteresis (the CAH is the difference between advancing and receding contact angles). Consequently, low CAH not necessarily hydrophobicity of surface ($\theta_{cs} > 90°$), is a better criterion for predicting whether a

material is suitable to promote DWC. The volume fraction of hydrophobic nanoparticles within metal matrix required to reduce the CAH sufficiently to promote DWC might be different from the values predicted using static contact angle calculations which need to be experimentally investigated. Since fabrication of metal matrix composites can be quite complex and the resulting particle distribution across the metal matrix is random,[45,90] condensation on surfaces with well-defined ordered nanoscale heterogeneities that mimic those of MMHNPCs are studied below.

2.3.2 *Mimicked Composite Morphology*

The heterogeneous surfaces of the composites were mimicked by fabricating ordered arrays of PTFE nanospheres on silicon substrates using a modification of the procedure given by Park et al.[91] (see Figure 2.2a). Specifically, after fabrication of the nanospheres via directed dewetting of liquid PTFE precursor using soft lithography and thermal annealing (steps i-iii), residual PTFE thin film was removed using oxygen plasma etching (step iv), and adjusted the wetting property of the silicon background using vapor phase deposition of Octyldimethylchlorosilane (ODMCS) (step v). I tailored the ODMCS deposition procedure to achieve background (i.e. measured on flat silane modified wafer without nanospheres) static water contact angles of 65° ± 4° and 77° ± 3° to fabricate samples that mimic surfaces of composites with "Cu-like" (θ_{Ms}~60°) and "Al-like" (θ_{Ms}~80°) matrix, respectively. To mimic different volumetric fractions of the hydrophobic nanoparticles, PTFE nanosphere arrays with varied pitch were fabricated by tuning the geometry of the polydimethylsiloxane (PDMS) soft stamps. In particular, stamps with parallel nano-grooves with line spacing (*ls*) of ~280 nm, ~420 nm, ~550 nm and ~830 nm were fabricated by spin-coating uncured elastomer on optical gratings having

corresponding *ls*. The Scanning Electron Microscopy (SEM) images in Figures 2.2b to 2.2e show typical PTFE nanosphere arrays resulting from thermal curing of spin-coated liquid PTFE precursor pressed by these four types of parallel groove PDMS stamps. The fabricated PTFE nanospheres have diameters in the range of ~120 to ~190 nm and are not arranged on a perfectly square grid. However, all average grid dimension values presented in Table 2.1 are below ~650 nm, being at or below the upper bound of the length scale regime I want to study. Based on direct image analysis of SEM and AFM data, the samples fabricated with ~280 nm, ~420 nm, ~550 nm and ~830 nm line spacing gratings had PTFE area fractions of ~0.09, ~0.12, ~0.13, and ~0.17, respectively. I note that the AFM analysis revealed that oxygen plasma treatment flattened the nanospheres to a thickness of ~20 to 50 nm (for consistency I continue referring to these discs as spheres). Importantly, the produced PTFE particle arrays uniformly covered entire ~1 cm^2 sample area and could be reproduced with high repeatability. In all, wetting properties and condensation dynamics on samples with four different PTFE nanosphere distributions with Cu-like and Al-like background and, as reference, bare and PTFE as well as silane modified silicon are studied.

Table 1 Geometrical parameters of PTFE nanosphere array fabricated with soft stamps made from gratings with indicated line spacing (ls). 'a-b', d, Afc and Afm stand for the average values of rectangular grid sides, PTFE nanosphere diameter, and calculated and measured area fractions, respectively.

	830			560			420			280		
parameter	a	b	d	a	b	d	a	b	d	a	b	d
	328	664	135	420	603	190	209	451	120	258	319	158
	±129	±42	±53	±108	±35	±31	±61	±41	±13	±72	±28	±27
A_{fc}	0.065±0.058			0.11±0.047			0.12±0.045			0.24±0.11		
A_{fm}	0.088			0.12			0.13			0.17		

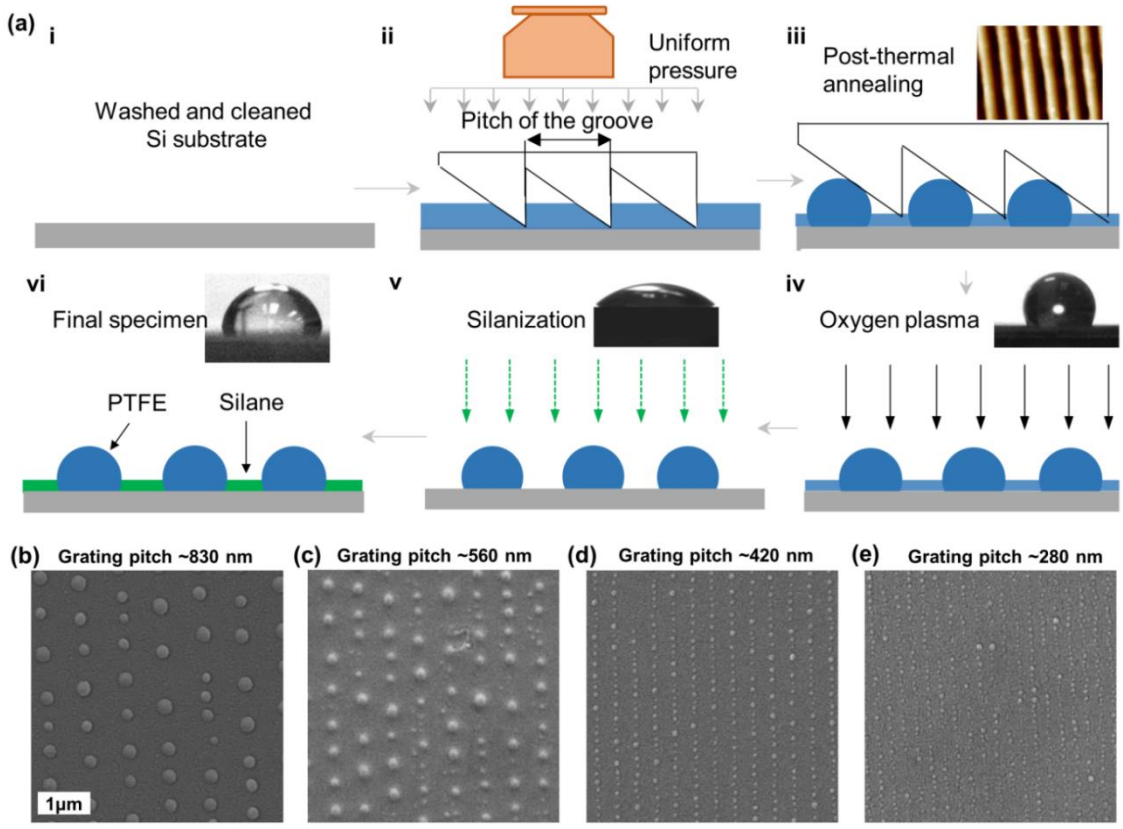

Figure 2.2 (a) Schematic of the mimicked composite fabrication procedure with inset images showing corresponding static water contact angles with silicon, PTFE, and ODMCS indicated with gray, blue, and green colors, respectively; the inset in iii shows example AFM image of a PDMS soft stamp surface; (b) to (e) SEM images of PTFE nanosphere arrays fabricated with different grating pitch soft stamps; Morphology of the grounding metal thin film required for high quality imaging is also visible in-between spheres.

2.3.3 *Wetting Properties of Mimicked Composites*

The presence of the nanosphere arrays on the ODMCS modified samples did not appreciably alter the static contact angle of water drops but had a major effect on their contact angle hysteresis. Specifically, the plot in Figure 2.3a shows that for all mimicked

Cu-like and Al-like composites the measured static contact angles were within ~5° of ~65° and ~80°, respectively. This observation is not surprising if area fraction of the PTFE nanospheres is taken into account which is at most 0.2. For such area fraction the Cassie-Baxter equation predicts a static contact angle increase below 5° for θ_{Ms} equal or greater than ~40°. On the contrary to the static contact angles, the CAH was found to decrease significantly with increasing density of the hydrophobic phase. The plot in Figure 3b shows that the CAH was reduced by ~10° (~33% to 42% reduction) with addition of the highest density of PTFE particles compared to the bare ODMCS modified wafer. In particular, the CAH is reduced from ~25° to ~15° for θ_{Ms}~77° and from ~30° to ~20° for θ_{Ms}~65°. This decrease is more substantial than predicted (below 5°), by area fraction based Cassie-Baxter arguments but it could be explained by considering the effect of the hydrophobic phase on motion of the solid-liquid-air contact line around the perimeter of the drops.[19,20,92,93]In this perspective, the contribution of the hydrophobic phase in Cassie-Baxter equation is evaluated per unit length of the drop perimeter not per unit base area. The hydrophobic phase contribution is much more substantial when dynamic contact angles are evaluated using per contact line arguments ($fl_H \sim d/P$) thanper base area arguments that scale with $f_H \sim 0.25\pi(d/P)^2$. Substituting the f_H and fl_H and advancing and receding contact angle values for PTFE and ODMCS into Cassie-Baxter relation, a CAH change obtained from adding the densest distribution of PTFE discs can be estimated. Using the per base area and per contact line arguments I estimate a CAH decrease of ~4° to ~5° and ~9° to ~12°, respectively. Thus, I assert that even a small addition of ~0.2 area fraction of nanoscale hydrophobic patches onto a hydrophilic matrix can substantially reduce the CAH of macroscale water drops by altering the contact line motion dynamics.

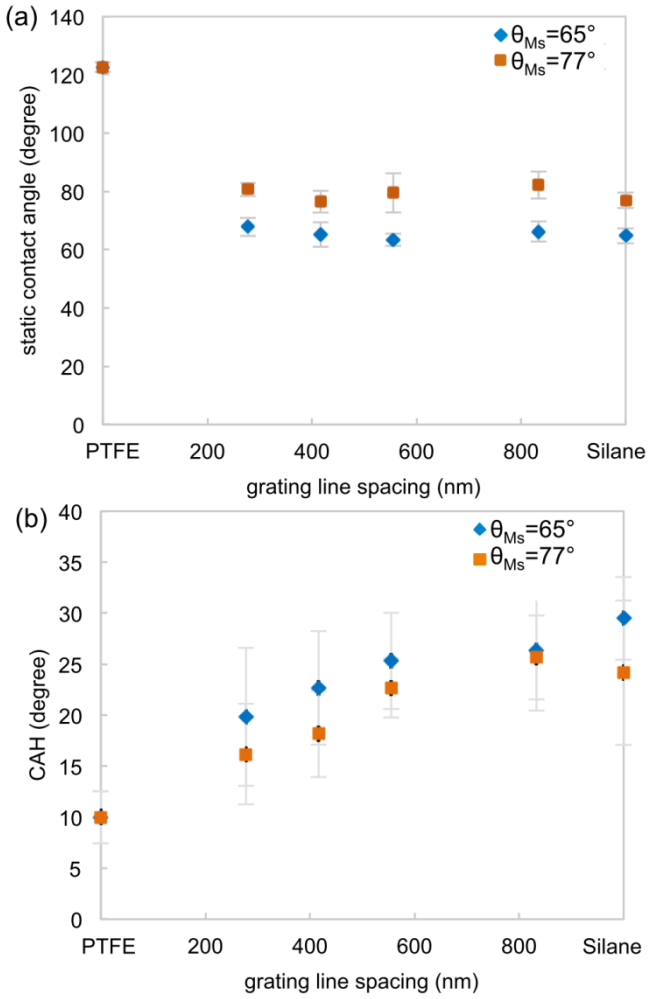

Figure 2.3 (a) Static contact angles and (b) contact angle hysteresis (CAH) of the mimicked composites.

2.3.4 *Microscale Condensation Dynamics*

Onset of this second growth stage occurs when droplet diameters become comparable to the average separation distance between closest neighboring droplet centers (i.e. l_{co}~5 to 10 μm).[66,67,69,94,95] To image the details of water condensation on this length scale occurring on the sample set described in Section 2.2.1, I used a custom humidity chamber coupled to a high speed camera mounted onto a high magnification optical

microscope. To provide perspective, I illustrate droplet dynamics on bare plasma cleaned (Figure 2.4a) and PTFE coated (Figure 2.4b) silicon wafers, what might be referred to as the bounding cases of rapid DWC-to-FWC mode and sustained DWC mode, respectively. Because the first sample has a receding contact angle below 5°, the outer part of the water droplets' contact line does not move after a coalescence event. This leads to rapid formation of highly distorted puddles (perimeter circularity, p_c<<1) that eventually merge into a continuous film. In contrast, microdrops formed by coalescence on the PTFE coated silicon recoil into equilibrium spherical cap shape with circular perimeter within ~0.1 ms (p_c~0.9). On macroscale, this sample has a high receding contact angle (~110°) and very low CAH (~10°). The rest of the images in Figure 2.4 show that on both Cu-like and Al-like samples increasing contact line fraction ($fl_H \sim d/P$) of the PTFE nanospheres from 0.27 to 0.55 (fabricated with gratings with line spacing of 830 nm to 280 nm) significantly reduces contact line pinning. Specifically, images in Figures 4c and 4e show that, after merging, drops on composites with fl_H~0.27 are highly deformed and essentially cover the outline of pre-coalescence drops (the compound drops in bottom images of Figure 2.4c and 2.4e have p_c~0.6 to 0.7). In contrast, images in Figures 2.4d and 2.4f show that within 0.4 ms after droplets merging on composites with fl_H~0.55, contact line retracts to form drops with high circularity (p_c~0.8 to 0.9). Thus, by increasing the amount of nanoscale hydrophobic patches on our composite samples, not only macroscopic CAH was significantly decreased but also microdroplet coalescence dynamics was altered to nearly resemble those occurring during sustained DWC mode on the fully PTFE coated sample.

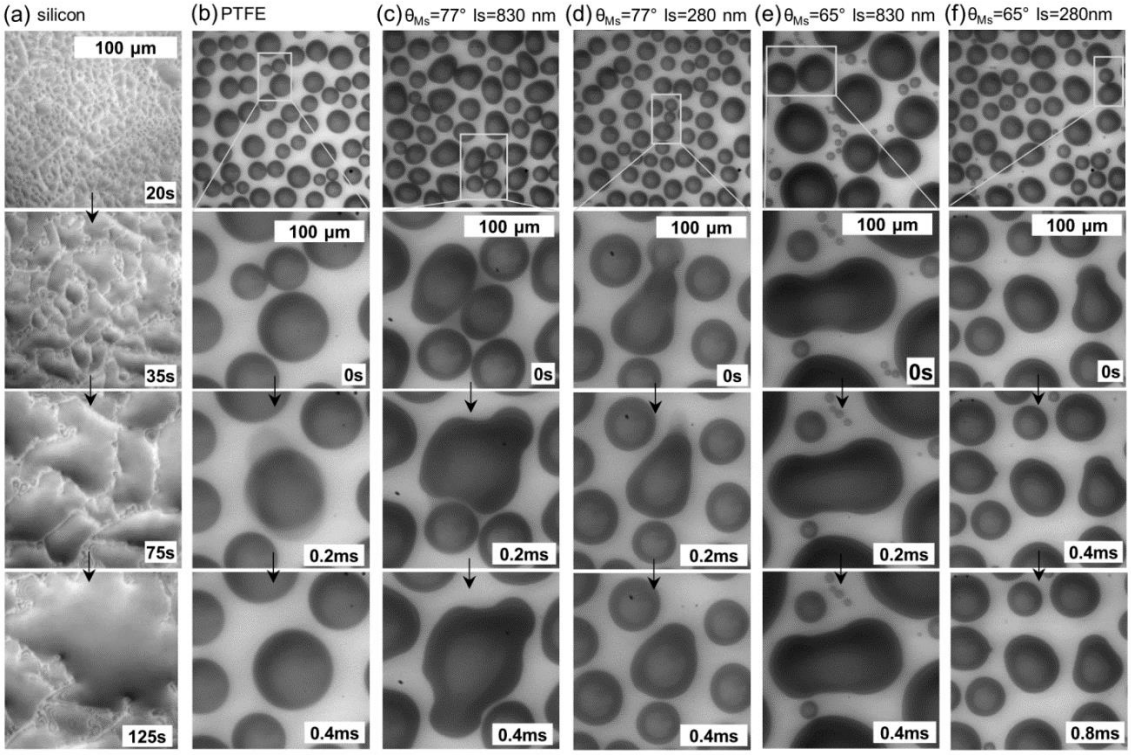

Figure 2.4 Sequence of optical images showing microscale droplet dynamics during water condensation on horizontally mounted (a) plasma cleaned silicon, (b) PTFE coated silicon, and (c) to (f) mimicked composites with PTFE nanospheres arrays fabricated with grating with 830 nm and 280 nm line spacing (ls) on ODMCS modified silicon wafer with Cu-like (θ_{Ms}~65°) and Al-like (θ_{Ms}~77°) wetting properties.

2.3.5 *Macroscale Condensation Dynamics*

The heat transfer rate during sustained DWC increases with decreasing drop departure radius.[30] To quantify how surface configuration of our mimicked composites impacts the drop departure radius, I conducted steady state condensation experiments on vertically mounted specimen. The experimental details are given by Damle et al[96]. Figure 2.5a shows examples of pre- (images in left column) and post-drop departure (images in right column) drop distributions on PTFE coated silicon as well as on Al-like composite

with coarse (grating line spacing of 830 nm) and dense (grating line spacing of 280 nm) PTFE nanosphere arrays. From Figure 2.5 bit is evident that, as the CAH, the drop departure radius decreases with increasing PTFE fraction on the surface. I observed that the specimen fully coated by PTFE had the smallest drop departure radius of ~1 mm, while the ODMCS coated samples without any PTFE nanospheres had the largest drop departure radii of ~1.6 to 1.7 mm. Addition of the densest PTFE nanosphere array reduced the drop departure radii to ~1.3 mm and ~1.45 mm for the Al-like and Cu-like composites, respectively. This change corresponds to ~40% of possible reduction towards the minimum reference departure radius set by drops shedding off the PTFE coated silicon. The presence of the PTFE nanosphere array made from grating with line spacing of ~440 nm had less pronounced effect, while presence of coarse arrays (grating with line spacing of 550 nm and above) did not alter the departure radius. Furthermore, increase of hydrophobic phase density led to lower departure radius on the composite with higher static contact angle such as θ_{Ms}~77°. This observation is in agreement with the absolute CAH of the Al-like composite being lower than that of the Cu-like composite. Despite lack of any hydrophobic phase, the solely ODMCS modified silicon wafers were also found to promote sustained DWC. The reason behind this 'non-filmwise-mode' condensation might be the atomistically flat topography of the silicon wafer. In industrial setting, metal surfaces displaying a similar static contact angle have at least a microscale roughness that significantly increases CAH. To illustrate the effect of this roughness on condensation mode I conducted a control experiment on mirror polished copper with static contact angle of 64° ± 5° and CAH of 37° ± 5°. I observed that this sample rapidly transitioned into FWC mode. To summarize, the mimicked MMHNPCs promoted DWC and with a threshold

density of hydrophobic phase facilitated drop shedding. In the next section the interplay between heat transfer enhancement, drop dynamics, and thermal conductivity of composites with varied hydrophobic phase densities is explored.

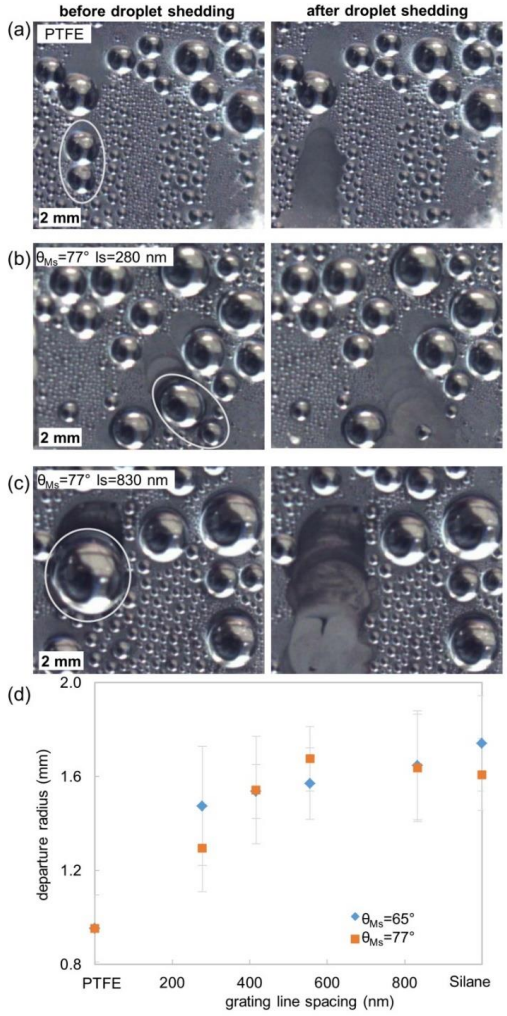

Figure 2.5 Sequential images captured 1 s apart of condensation on vertically mounted (a) PTFE coated silicon and ODMCS modified silicon with nanosphere arrays made with ls of (b) 280 nm and (c) 830 nm showing sample before and after gravity assisted drop shedding; (d) Plot of average departure radius for different mimicked composites as well as ODMCS and PTFE modified wafers.

2.3.6 *Estimation of Heat Transfer Enhancement During the Condensation Process*

I estimated the condensation heat transfer coefficient for different composites by substituting experimentally observed contact angles and departure drop radii into DWC model developed by Kim and Kim.[79] This model was initially developed for modeling of DWC on superhydrophobic surfaces (θ_c>>90°), but was recently adapted for and experimentally validated by Rykaczewski et al.[9] for DWC with drops with θ_c<90°. The model predicts heat transfer through a drop with radius r and contact angle θ:[97]

$$q_d = \frac{\Delta T \pi r^2 \left(1-\frac{r_c}{r}\right)}{\left(\frac{\delta}{sin^2\theta k_{coat}}+\frac{r\theta}{4k_w sin\theta}+\frac{1}{2h_i(1-cos\theta)}\right)} \quad (1)$$

where ΔT, r_c, h_i, δ, k_{coat}, and k_w are the surface subcooling, critical nucleation radius, interfacial liquid-vapor heat transfer coefficient, thickness of the coating, and thermal conductivities of the coating and liquid water, respectively. The overall heat transfer rate per unit area for different surface subcooling was obtained by integrating the product of q_d and drop size distribution, $n(r)$, from r_c to the departure radius of curvature $r_d = r_{base}/sin\theta$:

$$q" = \int_{r_c}^{r_d} q_d \, n(r) dr \quad (2)$$

The total condensation heat transfer coefficient, h, is obtained through a linear fit of the calculated heat transfer rate per unit area for modeled surface subcooling range. The effect of the hydrophobic nanoparticle filler on the overall heat transfer was incorporated using equivalent thermal conductivity of the composites calculated using the Maxwell model (δ and k_{coat}). I estimated the volumetric fraction of spherical PTFE nanoparticles corresponding to the PTFE nanosphere arrays on our mimicked composites by assuming a cuboid lattice with sides a and b (see Table 2.1) and height of (a+b)/2. Even the upper

bound of the highest estimated volume fraction corresponding to densest PTFE nanosphere array is only 0.15. Thus, our experiments suggest that the volume fraction of hydrophobic nanoparticles required to promote DWC on MMHNPC is substantially smaller than the theoretically estimated volume fraction of nanoparticles required to make the composite surface hydrophobic (see Figure S1b). Furthermore, the plot in Figure 2.6a shows that 0.15 volumetric fraction of PTFE nanoparticles would only cause a minor ~0.2 reduction in k_{eff}/k_M. However, as it was pointed out in previous section, metal samples will have a roughness higher than that of the nearly perfectly smooth silicon wafers. Consequently, a larger volumetric fraction of hydrophobic particles will likely be needed to promote DWC using these composites. To account for this possibility, heat transfer on composites with volumetric fraction of hydrophobic particles three times higher than the upper bound set by our experiments (i.e. 0.45) was also modeled.

The calculated heat transfer coefficients for different thicknesses of aluminum, copper, and nickel (another common condenser material with k_M~91 W/mK) matrix composites with PTFE nanoparticle filler with volume fraction between 0.03 and 0.45 are shown in Figure 2.6b. The heat transfer coefficients for DWC occurring on a PTFE and ceria films (departure radius of ~1.35 mm[41]) with different thicknesses are also plotted. For reference, lines indicating heat transfer coefficient for filmwise condensation of water occurring in same conditions calculated using the Nusselt model and twice this value are also indicated.[9,98] In agreement with literature,[30] this theoretical analysis predicts that benefits of enhancing DWC using a low thermal conductivity polymer such as PTFE are annulled when the film is thicker than ~6 μm. In turn, a 6-fold and a 3-fold heat transfer enhancement over FWC can be achieved by using higher thermal conductivity ceria film even with a

thickness of ~10 μm and ~100 μm, respectively. However, the mismatch of thermomechanical properties of metals commonly used in condensers and ceria would likely lead to delamination of the ceramic film. Such failure mode might be avoided with use of MMHPCs. Our heat transfer analysis suggests that the 5-fold heat transfer enhancement over FWC achieved by using these materials can be sustained even with composite thicknesses of 100 to 200 μm. Furthermore, about a 2-fold heat transfer enhancement can be obtained with essentially bulk-like composites with thickness of 1 mm or more. Most importantly, the condensation heat transfer enhancement achieved by use of the composites with thicknesses below ~1 mm is nearly independent of the volume fraction of hydrophobic nanoparticles (within the modelled 0.03 to 0.45 range). This result highlights the benefit of using metal matrices with high thermal conductivity. Even when reduced by half of the matrix material's conductivity by presence of hydrophobic nanoparticles, Cu and Al based composites have thermal conductivities much greater than that of ceria and PTFE ($k_{Cu0.45PTFE}$ ~177 W/mK and $k_{Al0.45PTFE}$ ~105 W/mK vs. k_{ceria}~17 W/mK for ceria). Consequently, even if it turns out that a higher content of hydrophobic nanoparticles than projected by our experiments is required to promote DWC on metal matrices with industrial surface finish (i.e. not perfectly flat), this is unlikely to significantly reduce achieved heat transfer enhancement.

Our heat transfer modeling results can also be used to roughly quantify a threshold thermal resistance posed by DWC promoter coating, $R_t^{"}$~L/k, that negates the advantages of DWC and reduces the net heat transfer rate to level attained by FWC without any coating (i.e. when in the modelled saturation conditions h_{DWC}/h_{FWC}~1). Specifically, for both PTFE and ceria $R_t^{"}$~2.5x10^{-5} K/W ($R_t^{"}$~6x10^{-6}/0.25~4.8x10^{-4}/17~2.5x10^{-5} K/W). For a promoter

material with given thermal conductivity, this value of threshold thermal resistance can be used to quickly estimate threshold thickness of the coating ($L_t \sim R_t^{"}k$) when $h_{DWC}/h_{FWC} \sim 1$. From the industrial point of view, it can be assumed that at least a two-fold heat transfer enhancement should be attained by promoting DWC ($h_{DWC}/h_{FWC} \sim 2$) in order to justify cost of the DWC promoter coating. For both PTFE and ceria films, $h_{DWC}/h_{FWC} \sim 2$ is attained when $L \sim L_t/3$ (i.e. $R^{"} \sim R_t^{"}/3$). Using these simple arguments, I estimate that copper and aluminum matrix composites fully loaded with PTFE nanoparticles (experimental limit of ~0.64[99]) can be used to promote DWC and at least double heat transfer rate over FWC if they are thinner than 800 μm and 500 μm, respectively.

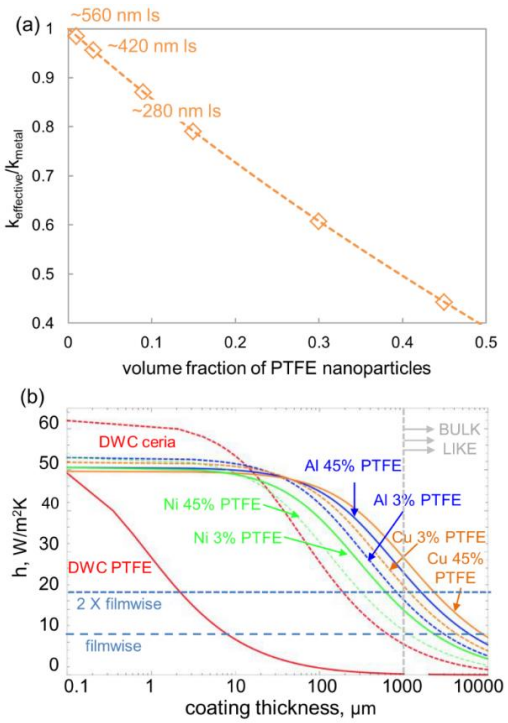

Figure 2.6 (a) Ratio of effective thermal conductivity of a composite to thermal conductivity of matrix metal as a function of different volume fractions of hydrophobic PTFE nanoparticles. Volume fractions corresponding to different nanosphere line spacing (ls) of the mimicked composites are indicated; and (b) modeled heat transfer coefficient for different thickness hydrophobic coatings consisting of PTFE film (red continuous), ceria film (red dashed), and different composition Al-PTFE NP (blue), Cu-PTFE NP (orange), and Ni-PTFE NP (green) composites with volume fraction between 0.03 to 0.45 (3 to 45%). For reference, lines indicating heat transfer coefficient for filmwise condensation occurring on bare copper and twice that value are also shown.

2.4 Conclusions

In this work I argued that metal matrix composites with hydrophobic nanoparticles could provide an attractive alternative to hydrophobic thin film materials for enhancing

water condensation rate by promoting the dropwise mode. The key findings of our experimental and theoretical investigation are:

(i) To alter condensation mode from FWC to DWC hydrophobic nanoparticles need to have diameters and spacing much smaller than average center-to-center spacing in-between closest neighboring drops prior to coalescence dominated growth stage (e.g. diameters of ~100 to 200 nm as in our experiments).

(ii) To promote DWC of water, surfaces do not necessarily have to have static contact angle greater than 90° (i.e. be hydrophobic), but rather need to have a low CAH.

(iii) Our experiments suggest that the desired low CAH can be attained with significantly lower hydrophobic nanoparticle density than that required to make the surface hydrophobic. The likely explanation for this observation is that the hydrophobic phase on the surface facilitates movement of the drop contact line during coalescing and gravity assisted shedding.

(iv) Our calculations show that a substantial heat transfer enhancement (two fold and higher) can be achieved even by using copper and aluminum matrix composites fully loaded with PTFE nanoparticles (maximum volume fraction ~ 0.64) to promote DWC if their thickness is below ~0.5 mm. The maximum volumetric fraction is four times higher than the upper bound of volumetric fraction needed to facilitate droplet shedding in our experiments. Use of a higher nanoparticle density might be needed to reduce the CAH of rough surface composites (in contrast to flat silicon wafer used as base for our mimicked composites). However, I provided arguments showing that using much higher nanoparticle density will not annul the heat transfer enhancement attained via DWC.

CHAPTER 3

WHEN CHEMICALLY ANISOTROPPIC SURFACE SHOWS NEAR ISOTROPIC WETTABILITY

3.1 Introduction

Controlling of water droplet motion on a surface is important for facilitating or improving the efficiency of many applications such as anti-icing or condensation.[10–17,100] Irrespective of the external force inducing the motion, surface wettability plays a vital role in this process. Advances in nanomanufacturing provide an unprecedented ability to modify surface chemistry and topography, however, quantification of how such changes alter some aspects of wettability, and with that drop motion, are still an active area of research. The role of the composition of the interfacial liquid-solid area on shape of a sessile drop, measured through static contact angle, is well established.[100–102] In contrast, the resistance a drop poses to motion, typically quantified by the contact angle hysteresis (CAH), is thought to be dominated by the composition of the surface at the three phase contact line (TPCL). Specifically, the surface composition alters the CAH by changing the fine structure of this contact line.[18–20] Yet, despite of having been imaged already four decades back,[21] it is only recently that studies have began quantifying the effects of contortions in the TPCL. Specifically, role of TPCL contortions in reducing the depinning threshold[22] and effective adhesion[23] was recently pointed out.

Although the impact of micro-scale contortions on the CAH magnitude has been recognized, effect of number and geometry of these contortions that depend on the length-scale of the surface heterogeneity[24] is still largely unknown. Simply altering heterogeneity length-scale for instance from micro to nano-scale will increase the number of kinks per

unit length of the TPCL by three orders of magnitude. Thus, surfaces with micro and nanoscale chemical or topographical heterogeneity can have significantly different CAH despite having similar static wettability. For example, recently Damle *et al*. reported that the CAH decreases with decreasing the size of nano-scale hydrophobic features on hydrophilic background where all the specimens had similar static wettability.[96] Hence, there is a need to systematically investigate the effect of number of contortions on the CAH value.

In this Chapter, the relation between the CAH and the number of contortions is experimentally investigated using striped surface having alternating hydrophobic-hydrophilic strips with size varied over three orders of magnitude (~100 μm to ~400 nm). In particular, the number of kinks were varied with ~2R/w where R and w are radius of the drop and strip width respectively. While characterizing the effect of number of kinks on static and dynamic wetting properties, it was observed that the droplet shape rather than number of kinks, plays the dominant role in defining the value of CAH where both droplet shape and number of kinks depend on the strip width. Our experiments further revealed that the nano-striped surface exhibits near isotropic wettability which is confirmed via comparing experimental results of droplet impact, condensation and droplet sliding experiments on striped and chemically homogeneous surface. Further, the isotropic and anisotropic droplet motion on ~400 nm and ~100 μm striped surface respectively, are studied using high speed camera. Moreover, two distinct mechanisms by which TPCL recedes parallel and perpendicular to striping during droplet evaporation on 100 μm striped surface are described. While moving in perpendicular direction, pinning force acting on TPCL was found to contradict with Shanahan's theory of stick-slip motion.[103]

3.2 Experimental Methods

In this Chapter, striped surfaces of width varying between 400 nm to 100 μm were fabricated on glass substrate using contact printing lithography. Specimen fabrication was confirmed using AFM or breath figure imaging or both. Later, static and dynamic surface wettability was characterized followed by condensation, droplet impact and droplet sliding and evaporation experiments. Below, the details of specimen fabrication protocol and experimental methodology are described.

3.2.1 *Sample Fabrication*

Silicon masters having parallel grooves of width varying from 400 nm to 100 μm were purchased (LightSmyth, Inc. and ASU Cleanroom facility) and were coated with hydrophobic material (ShieldGuard, IST, Inc.) through vapor deposition at 150W, 300mTorr for 45 min using BlueLantern (IST, Inc.). Next, pre-mixed and degassed PDMS elastomer and curing agent mixed in the ratio 10:1 was poured on the silicon masters. In order to remove any air-bubbles generated during pouring and to completely fill the master grooves with PDMS, the samples were held under vacuum for ~ 10 minutes. After curing at 120°C for 10 minutes, the soft PDMS stamps were manually peeled off from the substrate to complete the fabrication process. For fabrication of the nano-scale stamps, h-PDMS layer supported by soft PDMS backing was made using the protocol given by Qin et al.[104] The PDMS stamps were brought in contact with vapor of (Tridecafluoro-1,1,2,2-Tetrahydrooctyl) Trichlorosilane (Gelest, Inc.) for 5 minutes. The PDMS stamps decorated with silane molecules were carefully placed on glass slides (Ted Pella, Inc.) for about 10 seconds. Care was taken to ensure that the PDMS stamps did not shear across the surface when being peeled off the glass. The AFM images and breath figures in Fig. 1a-e clearly

show the parallel line patterns were successfully transferred for all sample sizes. Furthermore, the fabricated patterns could be produced repetitively and uniformly over 1cm x 1cm area. All the experiments were conducted on freshly fabricated samples. In addition, two control specimens were also made. One being glass slide completely covered with the silane molecules and other being bare untreated glass slides. Next I describe the experimental methodology.

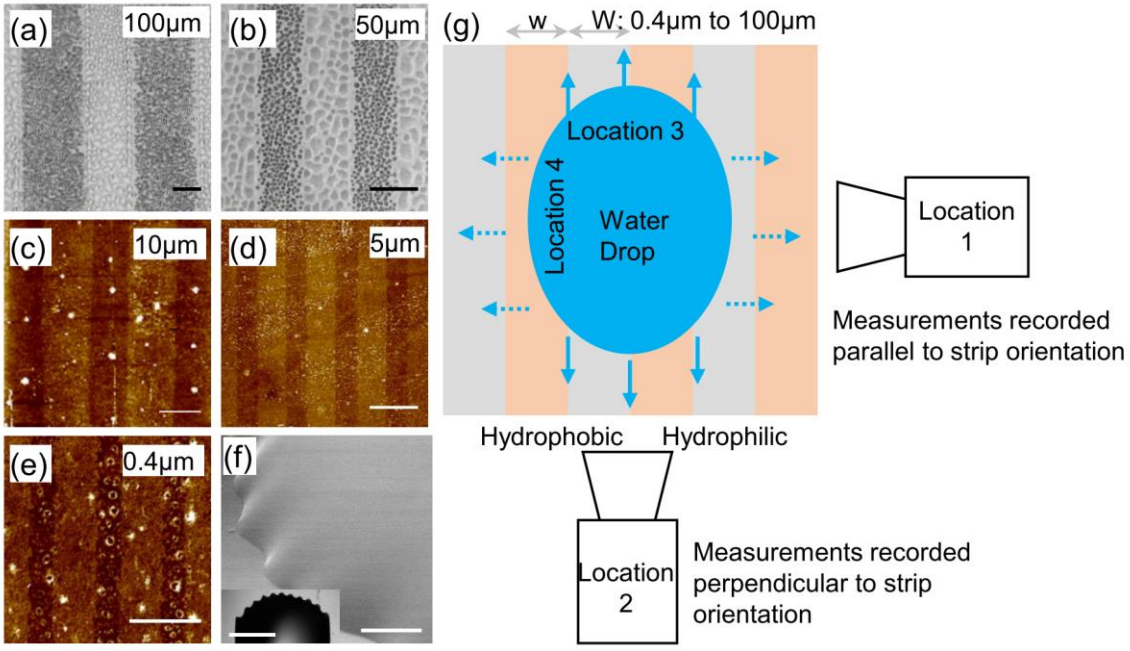

Figure 3.1 Breath figure patterned formed on specimen with strip width (a) 100 μm and (b) 50 μm (Scale bar- 50 μm). AFM scan of specimen with strip width (c) 10 μm, (d) 5 μm (Scale bar- 10 μm) and (e) 0.4 μm (Scale bar- 1 μm). (f) Kinks in the TPCL of a drop imaged using environmental scanning electron microscope (Scale bar- 50 μm). Inset shows an image recorded using optical microscope (Scale bar- 1 mm). (g) Schematic of the liquid droplet placed on a chemically heterogeneous striped surface.

3.2.2 *Wettability Characterization*

Static and dynamic wettability of the fabricated samples was tested using Goniometer (Rame-Hart) parallel and perpendicular to striping from location 1 and 2 respectively as shown in Fig 1g. First, four different ~ 2 µl drops were deposited on the specimen to measure the average value of static contact angle with two standard deviations. Then to quantify dynamic wettability via measuring CAH, separate images were chosen to calculate eight advancing (θ_{a1}, θ_{a2}, ..., θ_{a8}) and eight receding (θ_{r1}, θ_{r2}, ..., θ_{r8}) contact angles. Average advancing and receding contact angle, θ_a and θ_r, with uncertainty $\sigma_{\theta a}$ and $\sigma_{\theta r}$ respectively, were calculated using these values. Average contact angle hysteresis was later computed as $CAH = \theta_a - \theta_r$ with $\sigma_{CAH} = ((\sigma_{\theta a})^2 + (\sigma_{\theta r})^2)^{1/2}$. Above mentioned procedure was repeated during three independent experiments on three different sample sets.

3.2.3 *Sliding Angle Measurement*

At least nine different 20 µL water droplets were deposited on the substrate mounted on the goniometer stage. Goniometer stage was tiled gradually at 1° per second and the inclination of the stage at which the receding TPCL of the droplet started moving was recorded as a sliding angle. Three independent experiments on three different sample sets were conducted where sliding angle was recorded parallel and perpendicular to striping to calculate average values with two standard deviations.

3.2.4 *Micro-Scale Condensation Experiments*

In-situ condensation experiments were conducted on the sample set fabricated in custom-made humidity chamber under light microscope. The samples were brought in contact with horizontally mounted Peltier element (Analog Technologies) kept in the custom made humidity chamber attached to the environmental chamber (ETS) under light

microscope (Zeiss). Temperature and relative humidity in the humidity chamber were maintained constant at ~30 °C and ~90% respectively using the environmental chamber. Peltier element was kept at the contestant temperature of ~5 °C using temperature controller to achieve subcooling of ~30 K. Three separate experiments were conducted on the same sample at different locations for ~30 minutes while images were recorded every 10 seconds using the camera mounted on the microscope. Further, images were analyzed using ImageJ to quantify the minimum circularity of the condensed micro-droplets.

3.2.5 *ESEM Experiments*

Samples were mounted on the in-house-made stub attached to the Peltier element in the SEM operated in the environmental mode (XL-30, FEI). Temperature of the Peltier element and water vapor pressure in the ESEM chamber was maintained at ~3 °C and ~10 mTorr respectively. A ~2 µL water drop was deposited on the pre-cooled sample using pipette before loading the sample into ESEM chamber. Droplet morphology near the three-phase contact line was imaged using electron beam and GSED detector at 15 keV to investigate the kinks in the three-phase contact line and the perturbation height as shown in Fig 1f where inset shows the optical microscope image of kinks.

3.2.6 *Droplet Impact*

Impinging droplet- striped surface interaction was imaged using a high speed camera. In particular, ~2.5 mm diameter water droplet, created using a syringe pump (New Era Pump System NE-1000), was allowed to impinge on the striped surface through hydrophobized needle (Hydrobead) from ~1 cm height and recorded simultaneously at 5000 fps. Interaction was made visible using a light source (Litepanels ENG light) mounted on top of the setup. For each sample, eight different droplets were impinged on the surface,

images were captured and analyzed to calculate the average values of droplet aspect ratio at fully stretched and retracted states with two standard deviations.

3.2.7 *Droplet Evaporation*

Water droplet evaporation was investigated using Optical Microscope and Laser Scanning Confocal Microscope. Specifically, using optical microscope, image sequence of ~1 µl water droplet evaporating at room temperature was recorded at 0.1 fps. Process was repeated 3 times for each specimen. Further, ~1 µl droplet of water, fluorescently labeled with Alexa Flour 488 (Thermofisher), was deposited on a 100 µm striped surface mounted on Laser Scanning Confocal Microscope. Three different image sequences were recorded in XZT mode at ~0.5 fps while droplet was allowed to evaporated at room temperature.

3.2.8 *Droplet Shape Analysis*

Images of 8 different ~2 µl water droplets were captured with light microscope for each sample. Pinning length and length of the droplet parallel and perpendicular to striping were recorded to calculate average value and two standard deviations.

3.3 Results and Discussion

3.3.1 *Static Wettability Characterization*

Static and dynamic wettability of the sample set is characterized. As liquid droplet placed on a striped[47,50,105,106] or on a grooved surface[21,107–109] show high static and dynamic wetting anisotropy, droplet wettability was studied parallel and perpendicular to striping from locations 1 and 2 respectively as shown in Fig 1g. Contact angles and CAH recorded using goniometer from location 1 and 2 are termed as '$\theta^{\perp}, CAH^{\perp}$' and '$\theta^{\parallel}, CAH^{\parallel}$' respectively. Static contact angles measured parallel ($\theta^{\parallel}$) and perpendicular ($\theta^{\perp}$) to strip orientation are shown in Fig 2a. Each data point corresponds to average of 12

measurements with 2 standard deviations recorded on three different sample sets. $\theta^{\parallel}$ for all the specimens was ~70° and found to correspond well with the theoretically predicted value using Cassie-Baxter equation: $\cos\theta^* = \sum f_i \cos\theta_i$. However, $\theta^{\perp}$ was found to increase with increase in the strip width. It is worth highlighting that the difference between $\theta^{\perp}$ and $\theta^{\parallel}$, which is a degree of static wetting anisotropy, decreases with decrease in the strip width. Ultimately anisotropy was found to nearly disappear ($\theta^{\perp} - \theta^{\parallel} < 5°$) for nanoscale strip width. Next it is explored if strip width has similar effect on CAH.

3.3.2 *Dynamic wettability characterization: Parallel direction*

Figure 3.2b shows the CAH, where CAH is defined as $\Delta\cos\theta = \cos\theta_{receding} - \cos\theta_{advancing}$, measured in parallel ($CAH^{\parallel}$) and perpendicular ($CAH^{\perp}$) direction calculated using the average of 18 $\theta_{advancing}$ and $\theta_{receding}$ each measured on three separate sample sets. It can be seen that the $CAH^{\parallel}$ barely changes as the strip width was varied over three orders of magnitude. Since, the contortion density in the TPCL is maximum perpendicular to striping (location 3) as compared to parallel orientation (location 4) due to sharp wetting contrast of the underlying surface, effect of the number of contortions, if any, should reflect in $CAH^{\parallel}$ value. Therefore, the number of contortions in the TPCL was concluded not to have a strong influence on the CAH. This observation was found to be in agreement with the literature. Specifically, in an experimental study, the hysteresis ($\Delta\cos\theta$) was observed to vary between 0.2 to 0.32 with size of the hydrophilic feature on hydrophobic background altered between 6 to 60 μm.[110] Furthermore, adhesion or hysteresis energy caused by the periodic contortions in the triple phase contact line of a suspended droplet placed on a superhydrophobic surface has been shown to be predominantly dependent on the non-dimensional phase fractions.[23]

3.3.3 *Dynamic Wettability Characterization: Perpendicular Direction*

Unlike $CAH^{\parallel}$, $CAH^{\perp}$ decreased remarkably with reduction in strip width which finally lead to near loss of dynamic wetting anisotropy for nanoscale strip width. Specifically, the difference in $CAH^{\perp}$ and $CAH^{\parallel}$ was found to reduce from $\Delta\cos\theta \sim 0.5$ to ~ 0.06 with alteration in strip width from 100μm to 0.4μm where the similar difference for bare glass slide and glass slide homogeneously covered with silane was ~ 0.01 and ~ 0.02 respectively.

As the magnitude of the CAH indicates the amount of pinning, effect of strip width on the net pinning force acting at the TPCL while droplet moving perpendicular to striping is investigated. Net pinning force is a product of pinning force per unit length and actual pinning length of the TPCL. Figure 2c and 2d show absolute values of advancing and receding contact angle and the pinning force per unit length at the advancing and receding TPCL, defined as $\gamma \times (\cos\theta_{receding} - \cos\theta_{Static})$ and $\gamma \times (\cos\theta_{Static} - \cos\theta_{advancing})$ respectively where γ is the surface tension of water. It can be seen that, irrespective of the strip width, the pinning force acting at the receding edge is at least three times more than that at the advancing edge. Moreover, reduction in the difference between static and receding contact angle leads to decrease in the pinning force acting at the receding TPCL with decrease in the strip width. Effect of strip width on net pinning length is investigated further.

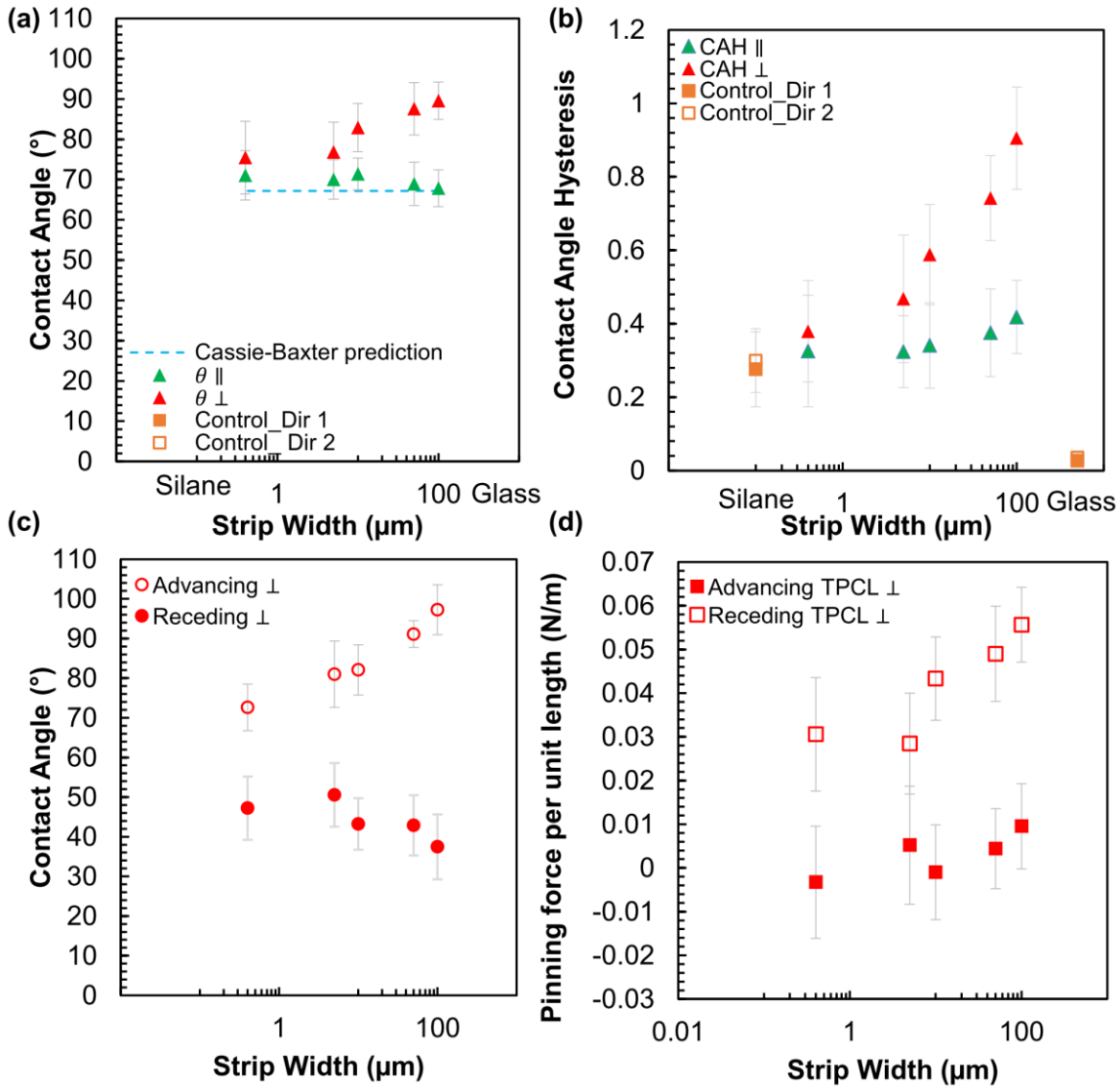

Figure 3.2 (a) Static contact angle and (b) contact angle hysteresis for specimens with difference strip width. (c) Advancing and receding contact angle measured perpendicular to striping and (d) pinning force acting per unit length at the advancing and receding TPCL.

Inset of figure 4a shows 2 µl water drop placed on a striped surface of width ~100 µm. The droplets placed on a striped surface had common features: straight edges parallel to strip (at top and bottom) and corrugated TPCL perpendicular to strips (at the left and right). While moving perpendicular to strips, TPCL pins at the straight edge. Hence this

pinning length is important in determining the net force acting on the TPCL where pinning length depends on the droplet shape that in turn is a function of strip width. In agreement with the literature[106], it was noted that the aspect ratio (AR) of the droplet, where AR is the ratio of the length of the drop parallel to striping to its width, approaches unity with reducing the strip width. Given the pinning force is proportional to the local length of the TPCL,[111] effect of strip width on droplet aspect ratio (L/w) and pinning length (Lp) was systematically investigated as shown in the Figure 3.3a. Furthermore, combining pinning length with the pinning force per unit length of the TPCL (Fig 2d) gives net force acting on the TPCL as shown in Fig 3.3b. It can be seen that, altering the strip width over three orders of magnitude changes AR barely 1.5 times which is sufficient to modify the pinning length and the net pinning force over two orders of magnitude. Pinning length stems from the straight line shape of the TPCL which is due to the periodic nature of the energetic barriers in this direction and pinning of the triple phase contact line at the linear border between the hydrophobic and hydrophilic stripes.[105,106,112] Bliznyuk et al.[112] proposed that, as in case of surfaces with linear grooves,[113] in order move across a hydrophobic strip, a droplet needs to first form a nucleus on the subsequent hydrophilic line that bridges across the hydrophobic one (similar mechanism was also observed in simulations[114]). Once the nucleus is formed, the drop simultaneously starts “filling” these two stripes (i.e. contact line spreads laterally across these two stripes). Explaining increase of both the static and advancing contact angle in perpendicular direction with the strip size, the energetic barrier for the formation of such nucleus increases with the degree of local contact line distortion required for the bridging to occur (i.e. strip width).[112]

Based on these results, droplet shape can be argued to be a principal factor in determining the CAH compared to the number of kinks in the TPCL as the former reduces over 2 orders of magnitude where latter varies only ~2 times on altering the strip width from 100µm to 5µm. Even though, the length scale of heterogeneity alters the CAH, CAH gets modified through variation in the shape of the droplet rather than increase in the number of kinks. Below, series of droplet impact, condensation and droplet sliding experiments conducted are described to confirm that nano-striped surface show near wetting isotropy.

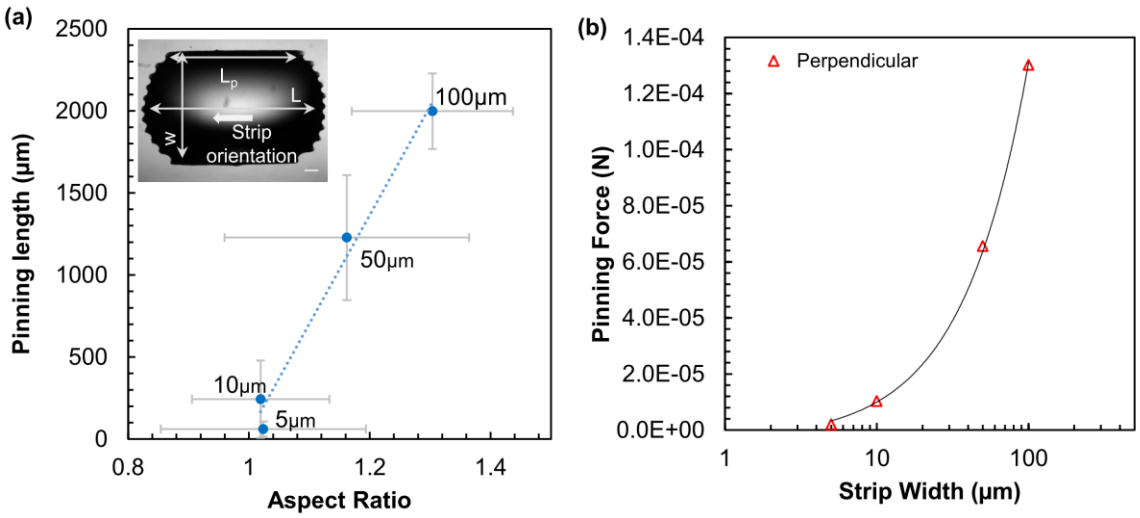

Figure 3.3 (a) Variation in pinning length (Lp) and aspect ratio of the drop (L/w) as a function of Strip width. Inset shows the 2 µl water drop placed on surface with 100 µm strip width and definitions of Lp, L and w. (b) Pinning force at TPCL while droplet moves perpendicular to strip orientation.

3.3.4 *Water Droplet Sliding Experiment*

Next, water droplet sliding experiments were performed as elaborated in section 3.2.6. Gravitational force acting on the water droplet deposited on an inclined surface when

exceeds the pinning force acting at the TPCL, droplet slides across the surface. Therefore, measuring the sliding angle is a good measure to assess the CAH and the overall pinning at the TPCL. As explained earlier, difference in CAH measured in two orthogonal directions was $\Delta \cos\theta \sim 0.06$ for nano-striped surface. If $CAH^{\parallel}$ and $CAH^{\perp}$ are similar, the angle at which droplet slides off the surface should also be nearly same which was confirmed with experiments in Fig 3.7.

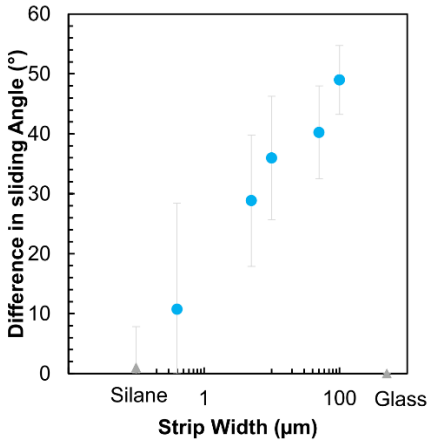

Figure 3.4 Difference in sliding angle recorded when 20 µl water drop slides across the surface parallel and perpendicular to strip orientation.

3.3.5 *Condensation Experiments*

Later, condensation experiments were performed at a very high subcooling in a custom made humidity chamber placed under optical microscope as described in section 3.2.4. As in the case of droplet impact, advancing and receding contact angles play a crucial role in condensation. Specifically, during droplet growth via mass transfer, advancing contact angle is important whereas during coalescing event receding contact angle is of significance. Figure 8a shows the microdrops generated through condensation on the sample set after ~1min into the experiment. Sample uniformly coated with silane show

nearly circular water microdrops as shown in the Fig 3.6a. On the contrary, water puddles were found to form on bare glass slide (not shown in the figure). It could be seen that samples with 50 μm and 100 μm strip width had elongated microdrops because of preferential coalescence along the hydrophilic strips. For specimens with strip width < 10 μm microdrops were reasonably circular. Effect of strip width on circularity was quantified by averaging the circularity of 6 droplets with minimum circularity. Considering the importance of advancing and receding contact angle in droplet growth during condensation, increase in circularity with reduction in strip width highlights the near same CAH along and perpendicular to strip orientation.

3.3.6 *Droplet Impact Experiment*

The impact of droplet on the fabricated sample set was imaged using a high speed camera placed under the sample as shown in Fig 3.5a. Figure 3.5b shows a sample image sequence that was further used to measure the aspect ratio (AR) of the drop, defined as ratio of length of the drop parallel to striping (blue) to its width (orange), in fully stretched and fully retracted states. Value of the AR, if more than unity, indicates the preferential wetting of the drop parallel to strips. On the contrary, aspect ratio less than unity implies width of the drop to be more than its length. For the nano-striped specimen, the droplet aspect ratio in fully stretched and retracted states are not only similar to those corresponding to homogeneous surface but AR is close to unity. Therefore, droplet appears to maintain its circularity even while moving across the surface. Taking this observation into account along with the similar magnitudes of $CAH^{\parallel}$ and $CAH^{\perp}$, it can be concluded that the droplet motion is nearly isotropic for nano-striped surface which is studied next using a high speed camera (Photron Fastcam Mini UX-100).

3.3.7 *Dependence of "Motion Anisotropy" On Strip Width*

Figure 3.7 shows the droplet movement on 100 μm and 0.4 μm striped surface. On 100 μm specimen, while the TPCL advanced or receded perpendicular to striping, discontinuous stick-slip events were observed. Conversely, parallel to striping, TPCL moved continuously without any stick-slip events. However, for nano-striped surface, TPCL movement was nearly continuous irrespective of striping orientation. Therefore, "motion anisotropy" was found to be negligible for nano-striped surface.

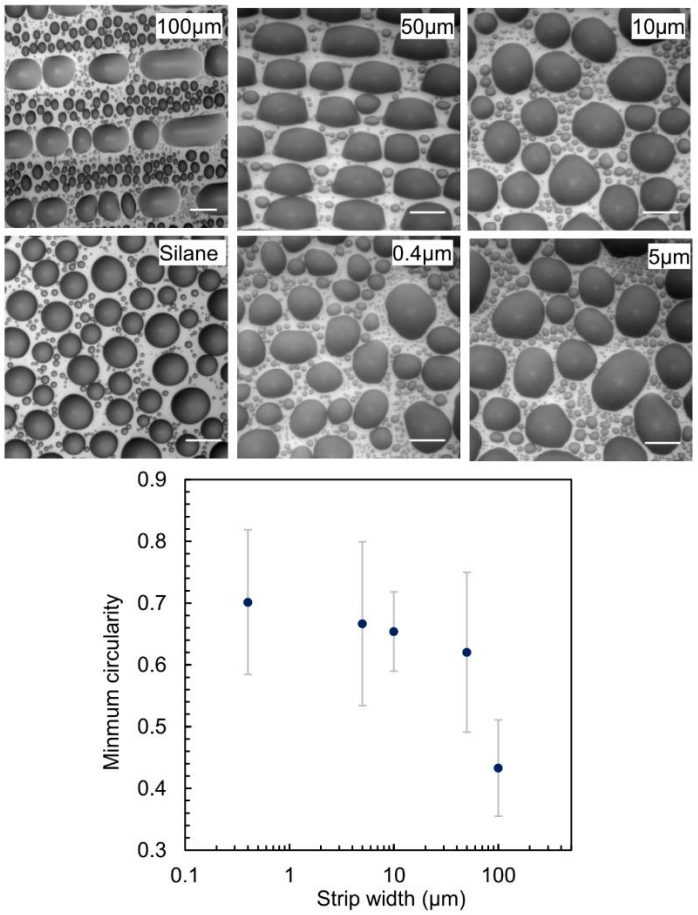

Figure 3.5 (a) Micro-droplets generated on chemically heterogeneous surface with different patterning length scales. (Error bar: 100 μm) (b) Minimum circularity of condensed micro-droplets.

Two distinct modes of TPCL movement on 100 µm striped surface were investigated further, where a water droplet evaporation was imaged with an optical microscope as shown in Fig 3.8a. Specifically, contorted TPCL receded smoothly parallel to strips where in perpendicular direction, jerky movement of TPCL without any contortions was observed. It should be noted that, at the micro-scale, motion of TPCL in parallel orientation may still have local stick-slip events, but these are invisible or have negligible effects on macroscale. It is interesting to note from the image sequence shown in Fig 3.8a that the distance between adjacent stick-slip events in perpendicular direction is proportional to the strip width. Hence the interdependence of the strip width and the slip length was further studied using Laser Scanning Confocal Microscope (LSCM). An image sequence of a droplet evaporation observed with confocal microscope is shown in Fig 3.8b. It is confirmed that, the distance travelled by TPCL during the subsequent stick-slip events is nearly twice the strip width. Specifically, the droplet gets pinned at the edge of the hydrophilic strip. After evaporation, once the depinning force exceeds the pinning force, droplet depins and rapidly moves across the hydrophobic strip before the TPCL again gets pinned at the next hydrophilic strip. It should be noted that, the macroscopic receding contact angle measured using goniometer, shown in Fig 3.2c, is substantially different than the actual receding contact angle, indicated by 'α' in Fig 3.8b, measured using LSCM. Moreover, the prior value matches closely with the apparent angle 'β' shown in Fig 3.8b. Evaporation experiment was also conducted on specimen with 50 µm strip width to further confirm the observation that slip length is nearly twice the strip width. However, for specimens having strips smaller than 10 µm, droplets were very circular and slip length could not be measured accurately from the evaporation experiments. Slip distance and the

pinning force acting at the TPCL, which was calculated earlier, are interdependent according to the theory of stick-slip motion which is discussed next.

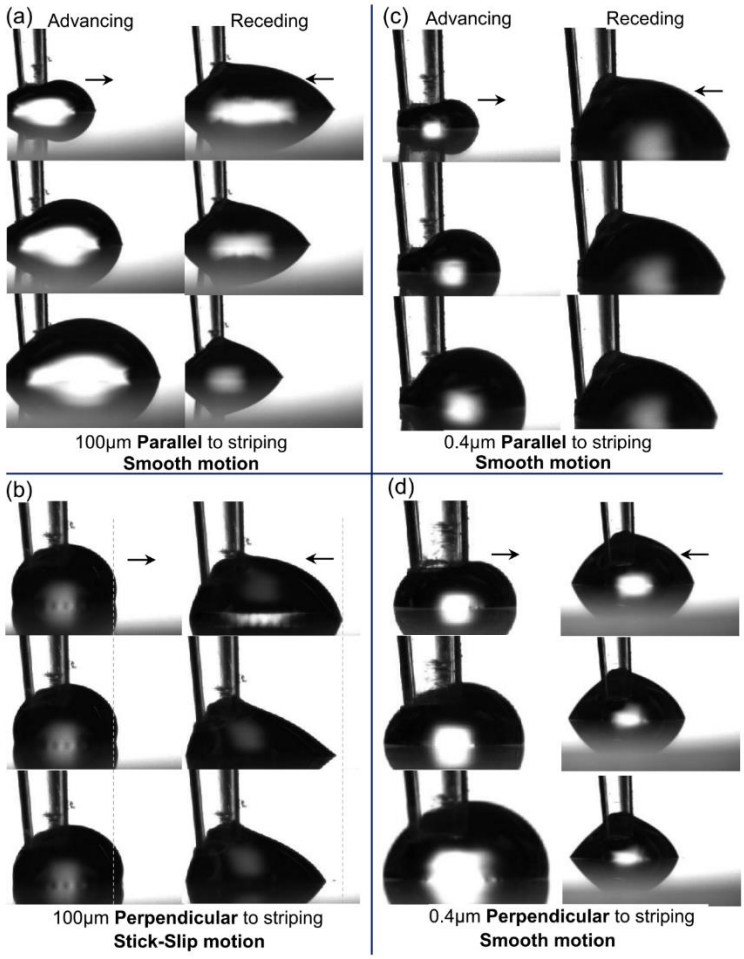

Figure 3.6 (a) TPCL advancing and receding smoothly parallel to striping on 100 µm surface (b) while TPCL shows discontinuous stick-slip motion while moving perpendicular to striping. (c-d) On nano-striped surface, TPCL moves continuously irrespective of striping orientation.

3.3.8 *Theory of Stick-Slip Motion*

According to the theory of stick-slip motion proposed a couple of decades back by Shanahan,[103] force acting on the TPCL or free energy available per unit length of TPCL 'U' (N or J/m) was given by:

$$U \sim \frac{(\delta r)^2 \gamma (\sin\theta)^2 (2+\cos\theta)}{2R} \tag{3}$$

where δr,γ,θ and R are the distance between adjacent equilibrium positions, liquid-air interfacial energy, equilibrium contact angle and radius of the droplet respectively. It is experimentally confirmed that δr ~ 2w for 100 μm and 50 μm striped surface. Furthermore, R was found to be reasonably constant for all the samples whereas static contact angle, hence the corresponding value of $(\sin\theta)^2(2+\cos\theta)$, was found to vary between 75° - 90° and 2.1 – 2 respectively. Therefore, equation 3 indicates the net force acting on the TPCL to vary as a function of square of strip width at least for 100 μm and 50 μm striped surface. Conversely, experiments show near linear dependence of net pinning force on strip width (Fig 4b).

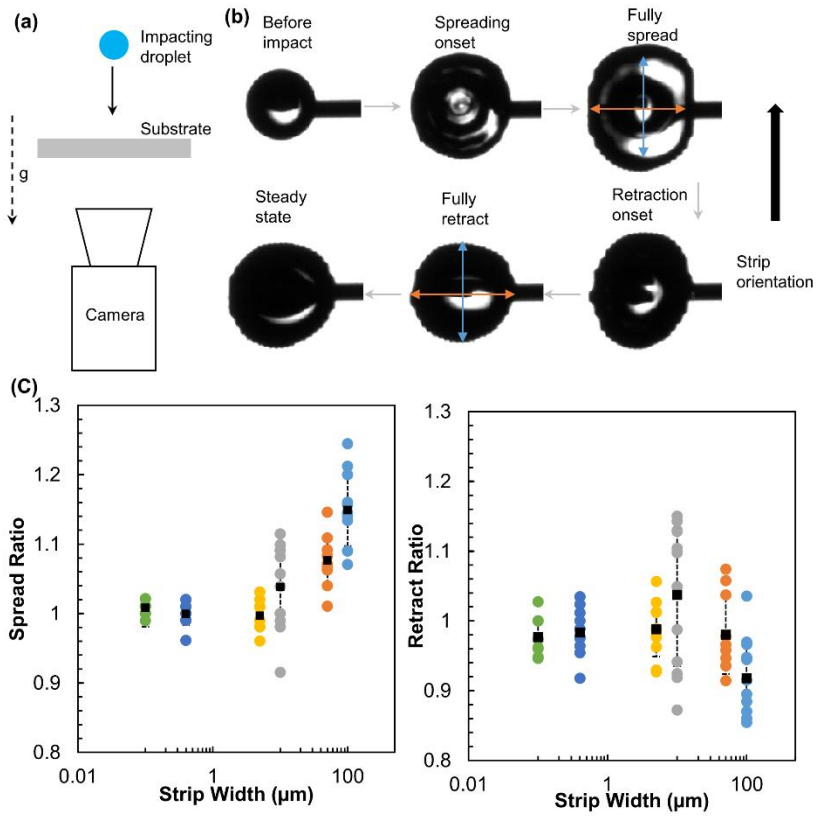

Figure 3.7 (a) Schematic of the experimental setup used during the experiment (b) Image sequence of the droplet-surface interaction (c) Aspect ratio of the drop while droplet is fully stretched and fully retracted for different strip widths.

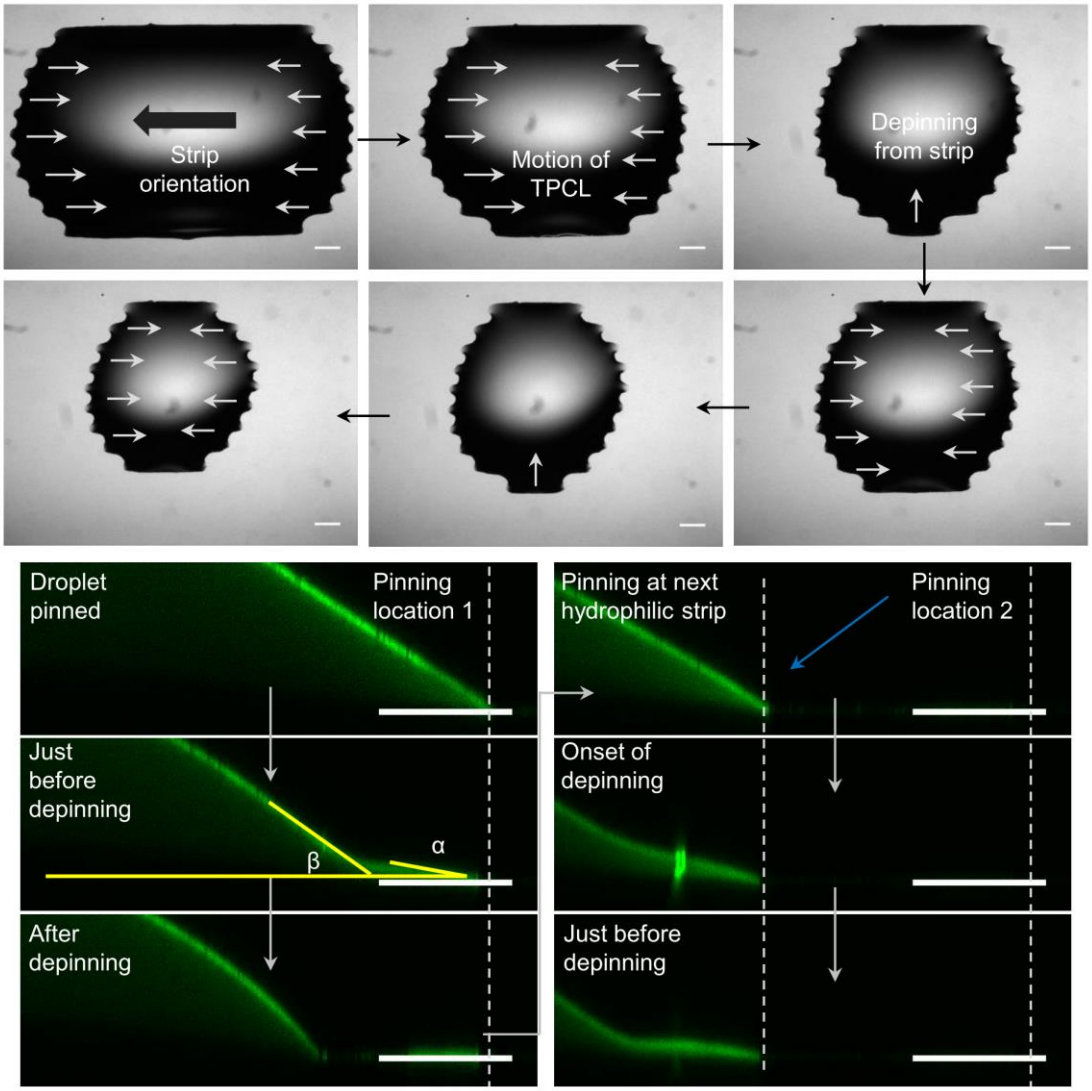

Figure 3.8 (Top) Time lapse image sequence showing movement of three phase TPCL during evaporation. (Bottom) Image sequence of movement of three phase TPCL during water droplet evaporation obtained using XZT mode imaging of Laser Scanning Confocal Microscope. (Error bar: 100 µm)

This discrepancy between theory and experiment could be explained based on the two possible reasons. According to Shanahan's theory, a droplet evaporates equally from all the sides on a homogeneous surface whereas TPCL either recedes parallel or

perpendicular to strips during evaporation on a striped surface at a given time point. Moreover, according to the theory, there is a natural selection for the next equilibrium position on a homogeneous surface. In particular, after the TPCL slips from the original location, energy dissipates due to the droplet movement which when goes below a threshold value droplet pins as the pinning force exceeds the depinning force. In the case of striped surface, next equilibrium position is altered externally. Therefore, there is a definite need to conduct an elaborate investigation to study the liquid droplet motion on striped surface which is beyond the scope of this chapter.

3.4 Conclusions

In summary, here the effect of number of contortions in the TPCL on CAH is investigated by varying the width of alternate hydrophilic-hydrophobic strip over three orders of magnitude (0.4 μm to 100 μm). It was concluded that the number of kinks do not have a significant impact on modifying the CAH value compared to the shape of the droplet where both number of kinks and shape of the droplet depend on the strip width. Furthermore, altering the droplet shape leads to the reduction in the pinning length of the TPCL over two orders of magnitude, which results in near wetting isotropy for nano-striped surface. Loss in wetting heterogeneity was subsequently confirmed via performing series of droplet impact, condensation and droplet sliding experiments. Further, two distinct mechanisms observed while TPCL receded parallel and perpendicular to strips during droplet evaporation are described. In particular, motion parallel to striping was continuous where TPCL motion had discontinuous stick-slip events in perpendicular direction. It should be noted that, contrary to the Shanahan's theory, pinning force acting on the TPCL was found to vary linearly with strip width while moving perpendicular to striping.

CHAPTER 4

"INSENSITIVE" TO TOUCH: FABRIC SUPPORTED LUBRICANT-SWOLLEN POLYMERIC FILMS FOR OMNIPHOBIC PERSONAL PROTECTION GEAR

4.1 Introduction

In healthcare and military applications, use of personal protection gear made from omniphobic materials that easily shed droplets of all sizes irrespective of surface tension of the fluid is of unparalleled importance. Such gears should provide enhanced protection from most hazardous liquids within a direct exposure zone as the penetration of hazardous fluids in the surrounding into the suit could have dire consequences. Additionally these gears also need to facilitate post-exposure decontamination because slow off-gassing of these dangerous chemicals from contaminated gear away from the direct exposure zone also poses a major health threat.[27,28]

Since micro-porous polytetrafluoroethylene (PTFE) fibers were introduced in the early 1970's,[115] most of the modern liquid repelling fabrics have been made of low surface energy materials with nano- and micro-scale morphology.[92,116–123] The resulting materials can have superhydrophobic properties manifested through sessile water drops with static contact angle greater than 150° and contact angle hysteresis (CAH) below 10°. [1,124] The low adhesion of water drops residing on top of these materials stems from a composite liquid-fabric interface that includes air cavities (i.e., the non-wetting Cassie-Baxter state).[47] A combination of low surface energy fibers with re-entrant geometry can also be used to make oleophobic[125–128] and even omniphobic[4,5,129,130] fabrics that repel liquids with surface tension down to ~25 mN/m and ~15 mN/m, respectively. However, textured superhydrophobic surfaces are easily wetted by low surface tension liquids, while

omniphobic surfaces with re-entrant texture can be flooded during condensation.[94] Furthermore, the latter surfaces have been demonstrated to shed macroscale drops of low surface tension liquid, but might be penetrated by a mist and/or spray with microscale droplets whose sizes are comparable to that of the texture.

Lubricated textured materials, on the other hand, can overcome some of the challenges posed by textured omniphobic materials by replacing the air trapped within cavities of the surface roughness with a low surface energy lubricant. This oil impregnated into the structure must be immiscible and must not react with any of the liquids that the material is supposed to repel.[6,131]Lubricated materials, in general, have been reported to possess self-cleaning, self-healing, and omniphobic properties,[6,131–133] and have been proposed for numerous applications, including condensation rate enhancement;[42–44,94,134] frost prevention;[135–137] ice,[135,138,139] bacteria,[140,141] and salt scale[142] accumulation; as well as reduction of drag and drop adhesion [7,143–146] and most recently manipulation of individual[147] and composites drops.[148,149] Shillingford et al.[150] recently extended the concept of lubricated surfaces to lubricated fabrics. Specifically, they demonstrated that omniphobic fabrics can also be achieved by impregnating a lubricant into micro-fibers coated with hydrophobic nanoparticles.

Durability is a key issue for fabrics since their expected use involves constant mechanical perturbation of the material. To simulate fabric wear expected in typical applications, Shillingford et al.[150] performed two types of durability tests. In the first set of experiments the authors observed how rubbing non-lubricated nanoparticle coated fabrics with a wipe affects the ability of the material to repel water. They found that the rubbing action induced some damage to the nanoparticle coating but did not affect the hydrophobic

characteristics of the fabrics. In the second set of experiments, Shillingford et al.[150]evaluated how water drop sliding angle is affected by repeated twisting of lubricated nanoparticle coated fabrics. In a majority of the cases, twisting induced damage to the nanoparticle coating and increased the water sliding angle. However, the ability of the lubricated fabrics to shed low surface tension liquids (i.e., remain omniphobic) during a typical application has not been tested. In addition to failure due to physical damage to the fibers' coating, omniphobic characteristics of lubricated materials can also be compromised by oil depletion. For example, the anti-icing performance of the lubricated nanotextured surfaces was found to degrade during frosting-defrosting cycles due to the rapid draining of the lubricant into a growing network of nano-icicles.[136] This observation raises a key question about performance of lubricated fabrics: *Can the lubricant be wicked away from the fabric when brought into contact with other materials (e.g., a second fabric, a wall, a chair, or, in the case of military operations, sand)?If so, what is the impact of lubricant depletion on the fabric's liquid-repelling characteristics*?

In this work, I investigate the depletion of lubricant from impregnated fabrics in contact with highly absorbing porous media and the resulting changes in the wetting characteristics of the fabrics by representative low and high surface tension liquids. In particular, the loss of the lubricant and the dynamic contact angles of water and ethanol on lubricated fabrics upon repeated pressurized contact with highly absorbent cellulose-fiber wipes at different time intervals is quantified. It is demonstrate that, in contrast to hydrophobic nanoparticle coated micro-fibers, fabrics encapsulated within a polymer that swells with the lubricant retain the majority of their oil and have the ability to easily shed water and ethanol, even after having multiple contacts with the high absorbing wipes.

4.2 Experimental Methods

4.2.1 *Specimen Fabrication*

Sample set used in this work had six fabric architectures for which the 100% cotton and 100% polyester (PET) were modified in three different routes. Specifically, these base fabrics were either conformally coated with hydrophobic alumina nanoparticles (referred to as NP-cotton and NP-PET samples), vacuum infused with Polydimethylsiloxane (PDMS) mixture (i-cotton and i-PET), or sandwiched in-between PDMS mixture with nearly flat exterior surfaces (s-cotton and s-PET). I note that control experiments were also conducted on bare fabrics and fabrics coated with both nanoparticles and solid PDMS. The latter sample was fabricated by encapsulating fabrics already coated with nanoparticles into a solid PDMS matrix. Further details of the sample fabrication process and experimental methodology discussed below are given by Damle et al.[151]

4.2.2 *Experimental Details*

Using the sample set described above, I conducted three types of experiments in this work: 1) measurement of lubricant absorption during soaking in oil bath 2) measurement of oil depletion during contact with absorbing media and 3) ethanol spraying and air-blowing experiment.

In the absorption experiments, the specimens were soaked in 10 ml of 100 cSt silicone oil at 15 minute intervals. Between each soaking interval, the samples were removed from the oil, excess oil was removed off the surface and weighted using the electronic weight scale. This procedure was repeated 6 times (2 h experimental duration and 1.5 h cumulative soaking time). In addition, samples were allowed to soak in oil for 20 h to see how much more oil they absorbed when compared to the 1.5 h soaking time.

In the second type of experiments, the specimens were soaked in 10 ml of 100 cSt silicone oil for 2 h to saturate the samples with oil. Excess oil was then removed from the fabric surface using the same procedure as described in Section 2.2. The contact experiments were conducted on the saturated specimen by placing the samples between two absorbing wipes and then pressing on them using a 200 g weight at pre-set time intervals of 30 s or 60 s. After each time interval, used wipes were replaced with new ones and the same specimen was again pressed against the wipes for the same time interval. This procedure was repeated 2 and 4 times or 5 and 10 times for pre-set times of 30 s and 60 s, respectively.

In order to conduct the ethanol spray experiments, 5 cm by 5 cm square pieces of s-cotton and NP-cotton and a square piece of a thick nitrile rubber acid-protection glove as a reference sample were used. Slightly smaller square pieces of cellulose wipes were placed behind the specimen before the stack was fixed to a vertical surface using an electrical insulation tape. Control experiments were conducted to ensure that the cellulose wipes were not directly exposed to the ethanol spray and were not stained by ethanol wicking in from the edges of the samples. Ethanol dyed blue using methylene blue (Sigma-Aldrich) was sprayed continuously onto the specimen as a fine mist and later it was removed from the specimen by blowing compressed air over the specimen. After completing the experiment, excess ethanol was carefully wiped from the area surrounding the specimen. Subsequently, the samples were carefully removed to expose the wipes mounted behind them.

4.3 Results and Discussion

These two base fabrics i.e. 100% polyester (PET) or 100% cotton were selected because Shillingford et al.[132] have shown that densely woven micro-fibers provide most robust omniphobic characteristics when coated by hydrophobic nanoparticles and soaked in a lubricant. The base cotton and PET fabrics had varying topology with the PET fibers closely aligned with the direction of the weave while the cotton fibers were more randomly dispersed (see Figure 3.1a and 3.1b). To provide an architecture similar to the nanoparticle coated fabrics described by Shillingford et al.,[150] the base fabrics were conformally coated via vapor-phase deposition of ceramic nanoparticles and thin locking matrix (see fabrication schematic and images of NP-cotton and NP-PET samples in Figure 3.1c). This treatment was followed by vapor-phase hydrophobization of the entire sample.[152] Silicon and metal substrates modified using this procedure have been previously used as a robust base for stable lubricated materials for anti-icing[136] and condensation enhancement applications.[94]

As an alternative to the lubricated NP-coated fabrics, the two base fabrics were modified with a polymer that can readily absorb and swell with a variety of oils. Our hypothesis was that use of such lubricant swollen polymer coating will decrease the oil release rate upon contact with other porous solids. Fabrics that retain more oil should have more robust omniphobic characteristics. PDMS was selected as the polymer coating because its swelling behavior is well known to significantly slow down release of a variety of oils.[153–160]The release dynamics of oils from oil-soaked PDMS paints have been investigated during biofouling experiments since the late 1970's.[141,153–160]In addition to slowing down release of the lubricant, use of an elastic polymer instead of a nano-ceramic

should also reduce the potential for cracking in the fiber's coating reported by Shillingford et al.[150] From an application perspective, use of fabric and polymer combination instead of just a free standing polymer film is beneficial because the woven fibers provide a robust backbone to the otherwise relatively fragile and thin (~100 μm to ~500 μm) PDMS film. PDMS and the fabrics were combined along two routes. The first route produced a composite fabric with topography closely following that of the original fiber weave. It was achieved this by forcing the PDMS mixture into the fabrics with vacuum infusion (see fabrication schematic and images of the i-cotton and i-PET samples in Figure 3.1d). Conversely, the second fabrication route resulted in elastomer penetration primarily around the outer fibers and, with the exception of a few residual craters resulting from trapped air bubbles, a smooth exterior surface (see fabrication schematic and images of the s-cotton and s-PET samples in Figure 3.1e). In addition to the fabric containing samples, I also made pure PDMS slabs with flat exterior surfaces and thicknesses of 100 μm, 500 μm, and 2 mm.

In order to complete fabrication of the lubricated fabrics, all the specimens were soaked in 100 cSt silicone oil bath followed by removal of excess of oil. I note that the latter step was not performed for the nanoparticle coated fabrics because it was found that even this brief procedure could remove oil from within the fabric. The plots in Figure 1f and 1g show normalized soaked sample mass ($\bar{m}_s$) that is defined as the soaked sample mass divided (m_s) by the dry sample mass (m_d) for different cumulative soaking times. The i-cotton and i-PET samples had significantly higher $\bar{m}_s$ than the s-cotton and s-PET samples as well as the plain PDMS slabs with comparable thickness to the fabrics. The i-cotton and i-PET samples also were saturated with the oil within first 30 minutes of

soaking, while the other samples showed another ~0.05 to 0.1 increase in $\bar{m}_s$ after the extended 20 h soaking. However, since the rate of silicone oil absorption was about 10 times slower in the later soaking stages for the latter samples, I capped the soaking time at 1.5 to 2 h for all the subsequent experiments. The nanoparticle coated samples impregnated rapidly with the oil to reach a normalized soaked mass of 1.87 ± 0.03 and 1.81 ± 0.11 for the NP-cotton and NP-PET samples, respectively (soaking time did not affect the $\bar{m}_s$). All coated fabrics were hydrophobic prior to soaking in the lubricant. However, the nanoparticle-coated fabrics were penetrated by ethanol, while the surfaces of the fabrics modified with a solid PDMS matrix were partially to fully wetted by the ethanol. Lubrication rendered all the fabrics omniphobic with CAH less than about 5° for both of the liquids.

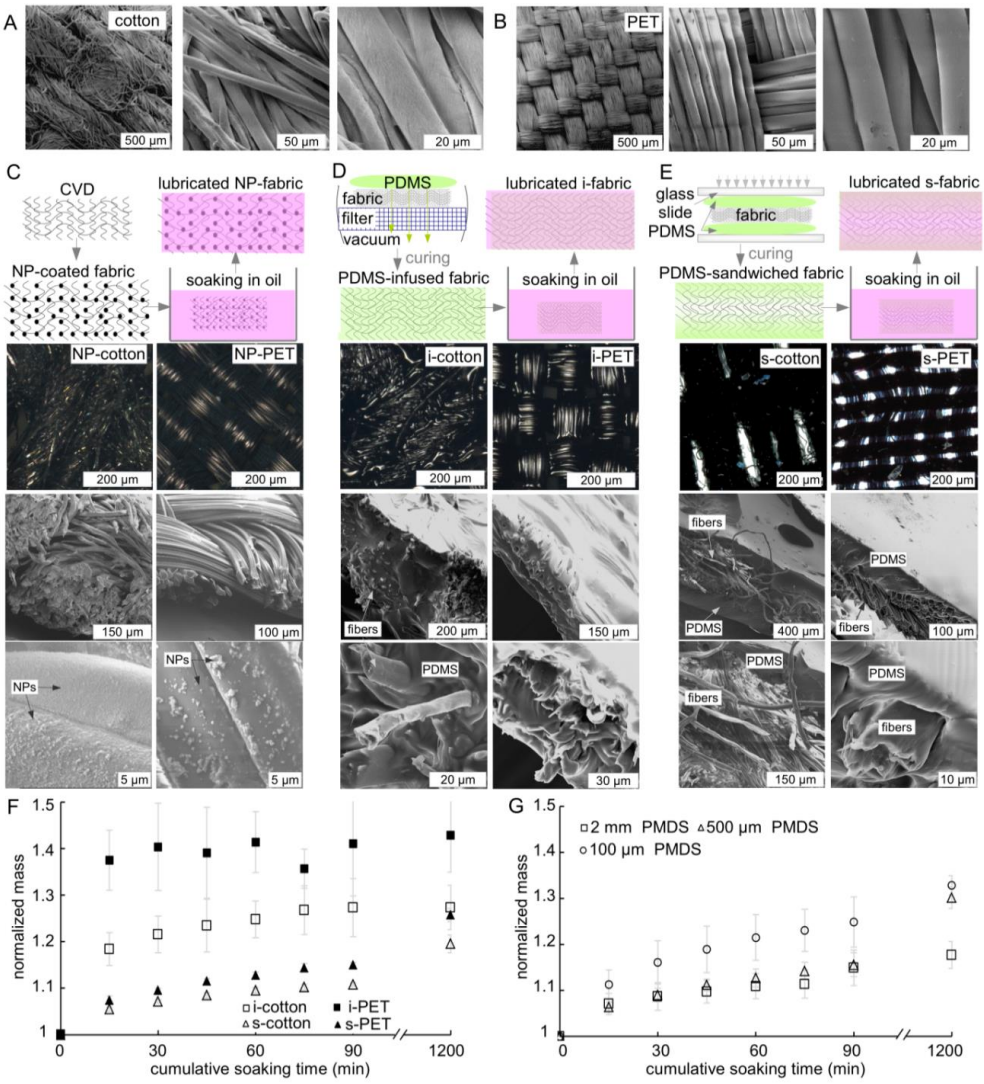

Figure 4.1 Optical and SEM images of densely woven (A) cotton and (B) polyester (PET) fabrics prior to modification, (C-E) fabrication process schematics of, top-down post-fabrication optical images, and cross-sectional post-fabrication SEM images of cotton and PE PET (C) nanoparticle coated (NP-) fabrics, (D) vacuum PDMS infused (i-) fabrics, and (E) PDMS sandwiched (s-) fabrics (i.e. fabrics supported PDMS slabs), images show samples prior to soaking with silicone oil; (F-G) measured silicone oil absorption quantified in terms of normalized soaked mass ($\overline{m}_s$) for the (F) fabrics and (G) flat PDMS slabs with thickness comparable to the fabrics.

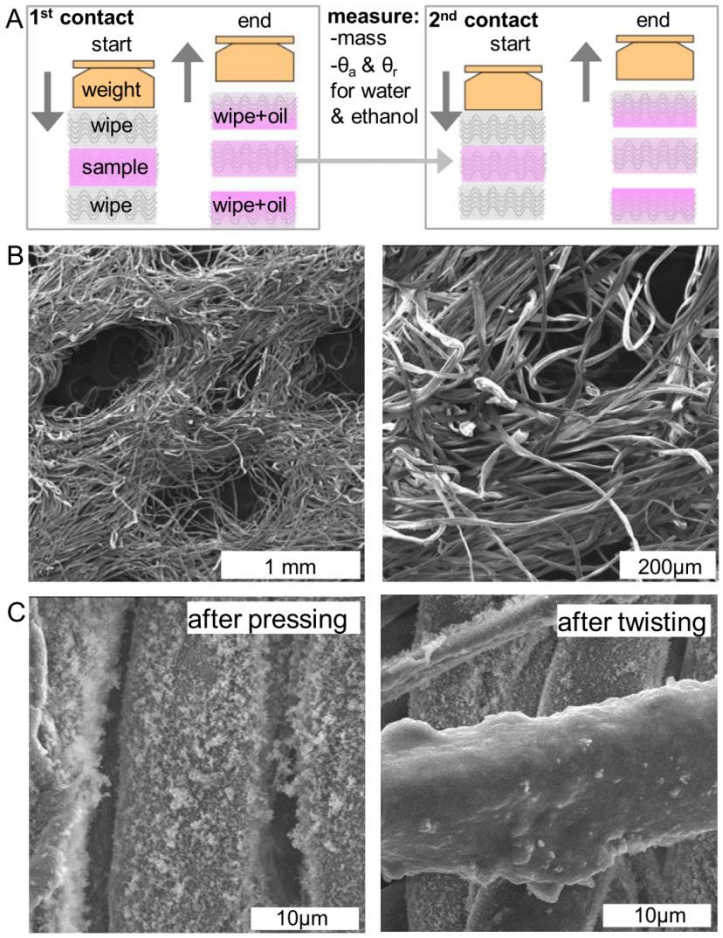

Figure 4.2 (A) Schematic of the multiple contact experiments with silicone oil and the absorbing cellulose wipes depicted in pink and gray, respectively, (B) SEM images of the cellulose wipes, and (C) SEM images of nanoparticle coated cotton fibers after pressing (no damage) and twisting (visible damage).

To estimate the fabrics' wetting characteristics upon contact with other objects, the samples soaked in silicone oil was placed between two cellulose fiber wipes (see schematic in Figure 3.2a and SEM images of the wipes in Figure 3.2b). These highly absorbing wipes were selected to provide a very conservative, "worst-case" scenario estimate of the lubricated fabric performance (could be representative of fabric on a chair). To simulate the typical force exerted by a person in contact with an object, I used a weight placed on

the top cellulose fiber wipe to induce additional pressure on the sample. The average surface areas of human bodies are on the order of ~1.5 m^2 to ~2 m^2 for adult females and males, while the average corresponding weights are ~60 kg and ~70 kg, respectively.[161] Thus, persons resting completely flat on their backs would exert a pressure of ~700 Pa. However, a person may also touch objects by partial contact, for example during sitting or resting against a wall. To account for this possibility, ~ 8 times higher pressure of ~5400 Pa was applied by placing a 0.2 kg over the ~3.6 cm^2 surface area of the top cellulose wipe. As schematically illustrated in Figure 2a, I conducted the experiments by bringing the fabrics in contact with the wipes for intervals of 30 s and 60 s with up to 10 contact instances. The SEM images in Figure 3.2c show that, in contrast to twisting and rolling, pressing the NP-fabrics did not degrade the fiber nanoparticle coatings.

The plots in Figure 3.3a and 3.3b show lubricant loss induced by multiple contact experiments for lubricated fabrics and, as a reference, oil-soaked PDMS slabs. I quantified the results in terms of normalized sample mass after contact ($\bar{m}_c$) that is defined as the ratio of sample mass after contact (m_c) to fully soaked sample mass before contact (m_{sf}). The most severe lubricant depletion was measured for both nanoparticle coated fabrics, with a $\bar{m}_c$ of0.8–0.85 and 0.8 after the 2 and 10 contact experiments, respectively. Multiplying the final normalized soaked mass of the samples ($\bar{m}_{sf}$) by $\bar{m}_c$ yields the ratio of masses of the fabric with retained oil to the dry fabric ($(m_{s_f}/m_d)(\, m_c/m_{s_f}) = m_c/m_d$). For NP-cotton and NP-PET, this ratio (referred to as $\bar{m}_r$) was ~1.4, implying that while these fabrics lose about half of the impregnated oil upon just 1 and 2 contacts (from normalized soaked mass of 1.8), a large amount of the lubricant is retained within the fabric (about 0.4 fraction of dry fabric's mass). In contrast, after 10 contact experiments the $\bar{m}_c$ ($\bar{m}_r$) was

0.97 (1.07), 0.96 (1.1), 0.86 (1.21), and 0.89 (1.1) for s-cotton, s-PET, i-cotton, and i-PET, respectively (see Figure 3.3a for all measured $\bar{m}_c$ values). So more oil was depleted from the i-fabrics than from the s-fabrics, whose oil retention was comparable to the PDMS slabs (compare left and right plots in Figure 3.3a). These results indicate that the fabrics modified with solid PDMS retain a higher fraction of the absorbed oil when brought into contact with the absorbing wipes. However, the PDMS modified fabrics also absorbed less of the oil during soaking (see Figure 3.1f), and thus in absolute terms had less stored oil when compared to the nanoparticle-coated fabrics, even after multiple contacts with the wipes. This difference likely stems from the oil occupying the space between fibers within the nanoparticle coated fabrics. In the case of the PDMS modified fabrics the corresponding space can only be partially filled with oil because it is mostly occupied by the elastomer (oil is stored within this space when the elastomer swells with it). Storage of oil deep within the nanoparticle-coated fabrics could also explain why significant lubricant depletion from these samples occurs only during first and second contact with the wipes. The wipes during these initial contacts are likely to remove oil stored near the top and bottom surfaces, resulting in the formation of air cavities between the remaining oil and the exterior of the fabric. These air gaps below the surface of the NP-fabrics effectively shield the oil stored near the center of the NP-fabric from contact with subsequent wipes, explaining negligible oil loss after the second contact experiments.

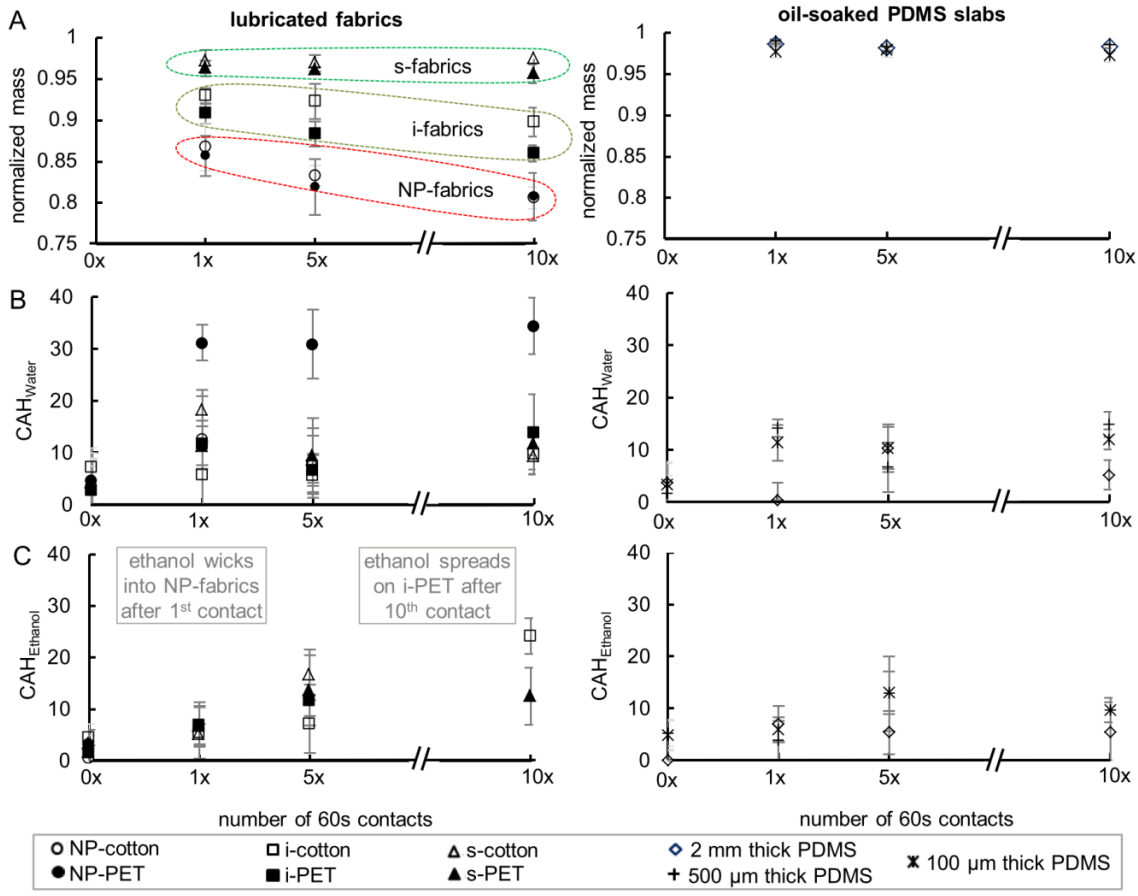

Figure 4.3 (A-C) plots of (A) normalized mass after contact with wipes ($\overline{m}_c$) (B) water contact angle hysteresis (CAH), and (C) ethanol CAH for the six types of lubricated fabrics and, as reference, oil-soaked PDMS slabs with different thicknesses.

Testing the wetting properties of specimens after contact with the absorbing wipes revealed dramatic changes. The plots in Figure 3.3b show that for the majority of the samples the water CAH increased from < 10° to < 20° after first contact with the wipes, but it remained unaffected by further contacts. The only exception was the NP-PET sample, which had the water CAH increase to ~30°. The images in Figure 1c show that the polyester fibers were not as well coated by the hydrophobic nanoparticles as the cotton fibers and without the lubricant also had very large water CAH of ~67° ± 4°. The plots in Figure 3.3c

show that for the ethanol experiments, not only did the CAH increase significantly, but the liquid also wicked into the NP-fabrics after just a single pressurized contact with the absorbing wipes. This observation provides further evidence that contact with wipes depletes oil only near the top surface of the NP-fabrics (but some oil remains stored within the center of the fabrics after the first contact). As a result, ethanol can spread on textured fibers that are exposed at the surface. For the fabrics modified with solid PDMS prior to soaking in oil, the change in ethanol wetting was dependent on the fabric architecture. The surface of the s-fabrics, as well as all of the PDMS slabs, remained omniphobic even after 10 contact experiments. The minor increase of ethanol CAH on the s-fabrics and PDMS slabs from initial ~5° to below ~15° was likely caused by few crater-like surface imperfection that were exposed after oil depletion. In contrast, for the i-cotton, the CAH increased nearly linearly with the number of contacts, settling on ~25° after the 10^{th} contact (see left plot in Figure 3.3c). Moreover, the i-PET sample had a CAH below 10° after the first and the fifth contact experiments, but was fully wetted by ethanol after the 10^{th} contact experiments. As in the case of the nanoparticle coated fabrics, the change in wetting properties mostly correlates with values of the normalized mass after contact ($\bar{m}_c$): the wetting properties of the i-fabrics degrade as they lose oil near the surface, while the fabrics-supported PDMS films, which retain higher fraction of absorbed oil, remain omniphobic. Another factor contributing to the difference between the i-and s-fabrics is their different surface topology. The i-fabrics have topology closely following that of the underlying fabrics, while the s-fabrics are mostly flat. The i-fabrics take in more oil (see Figure 3.1f), which is absorbed into the polymer as well as stored between the topological features. However, as in the case of the lubricated nanoparticle-coated fabrics and solid

textured materials,[133] the oil stored between the microscale topological features is most easily removed. Thus, despite the PDMS slowly releasing stored oil within its matrix, large microscale topological features are exposed by the contact experiments (see schematic in Figure 3.4a). As demonstrated by the strong pinning of water droplets on the partially de-lubricated i-cotton fabric highlighted in Figure 3.4a, the exposed topological features act as droplet pinning sites. Pinning by microscale topological features has also been previously observed for deposited[133] as well as condensed[43,133] droplets on solid nano/micro-textured lubricated surfaces. In addition, it was also observed water drop pinning on the i-fabrics prior to soaking in oil. While measuring the advancing contact angles, the images of drops advancing and receding after relaxation from pinning were selected and not at the rather sparse pinning site (separation of ~100-200 μm). In contrast, water drops advancing on the nearly smooth fabric supported PDMS films (i.e., s-fabrics) did not display any pinning (Figure 3.4b). Further, the fabric-supported PDMS films easily shed drops of ethanol even after 10 contact experiments because of the combination of a smooth surface and continual re-lubrication by oil that is released from the PDMS matrix.

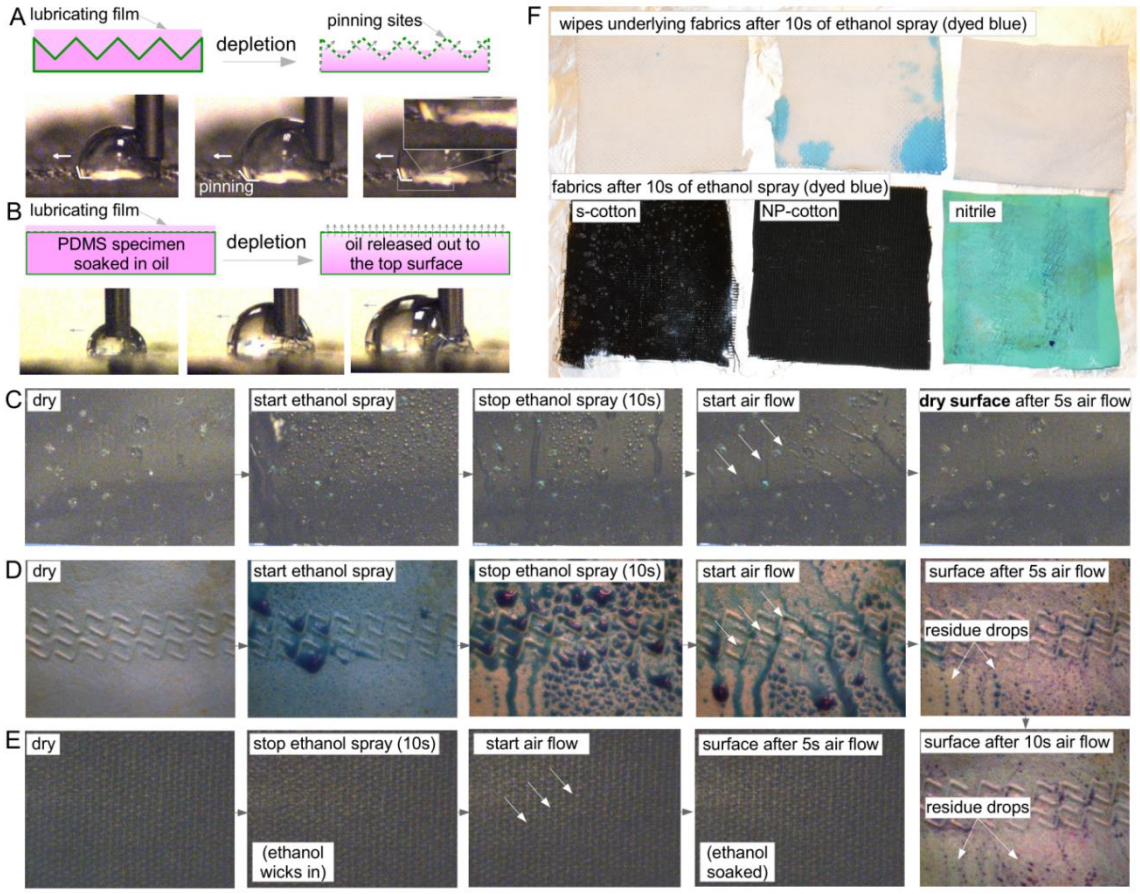

Figure 4.4. (A-B) Schematics of oil depletion process and sequential images of water droplet advancing on partially depleted (A) lubricated PDMS infused cotton fabric and (B) lubricated s-cotton fabric; (C-E) Sequence of close-up images of large (~25 cm2) samples of (C) lubricated s-cotton, (D) thick nitrile rubber used for personal protection gloves, and (E) lubricated NP-cotton during 5s ethanol spraying (dyed blue) followed by 5-10s cleaning air flow step. Prior to spraying top surface of the lubricated fabrics was brought in contact with absorbing wipe; (F) image showing fabrics and absorbing wipes that were underlying the three fabrics during the spraying experiments.

To illustrate the potential of the best performing lubricated s-fabrics as omniphobic, durable, and easy to decontaminate personal protection gear, dyed ethanol mist was

sprayed on larger (~25 cm^2) vertically mounted fabric samples for 5s and tried to clean the liquid off from the samples using a moderate air flow. As reference, I also sprayed and attempted to air dry a piece of a thick nitrile glove, which is a common component of personal protection gear. Before being mounted with tape, the lubricated samples were brought into contact with a large absorbing wipe under light pressure for 1 min. In addition, absorbing wipes with surface areas smaller than that of the fabrics were mounted under the samples before start of spraying experiments (for further details see Support Information). The images in Figure 3.4c to 3.4d show that while ethanol droplets formed on the rubber and lubricated s-cotton samples, ethanol spread onto the lubricated NP-cotton sample. Furthermore, the image in Figure 3.4f shows that ethanol penetrated through the NP-cotton sample and stained the underlying wipe. In contrast, the s-cotton and nitrile samples not only prevented penetration of ethanol, but also were cleaned from majority of the deposited ethanol with moderate air flow. However, while 5s of air flow was sufficient to entirely remove ethanol droplets from the s-cotton sample (i.e., completely dry surface), residual micro-droplets of ethanol remained on the nitrile glove even after 10s of air flow.

4.4 Conclusion

It is demonstrated that oil retention near the exterior surface as well as surface topology dictate whether lubricated fabrics remain omniphobic after contact with highly absorbing porous solids. Previously proposed nanoparticle coated fabrics remain hydrophobic, but, lose their omniphobic properties due to significant oil depletion near the fabric surface. This depletion is induced by a single, short, lightly pressurized contact with the absorbing wipe. In contrast, the oil-soaked fabrics modified with solid PDMS that swells with the oil lose less of the absorbed oil, and consequently have more robust

omniphobic characteristics. In addition, I demonstrated that the PDMS modified fabrics with flat rather than micro-textured topology that followed the fabric weave performed significantly better, retaining most of their oil and remaining completely omniphobic even after 10 contact experiments (cumulative contact time with highly absorbing medium of 10 minutes). My experiments also illustrated that the lubricated fabric supported PDMS films not only resist penetration of ethanol spray but also can be completely cleaned off from ethanol micro-droplets within a few seconds of moderate airflow. Fabrication of the robust and durable omniphobic s-fabrics is simple and easily scalable. Their lubrication or re-lubrication can be done within ~1.5 to 2 h, making them easy to maintain. Lastly, I note that PDMS and the silicone oil combination was used in this work to illustrate that polymers swollen with a lubricant could provide robust omniphobic surfaces. Naturally, the choice of the lubricant and the absorbing polymer, which can be designed to absorb the specific lubricant,[162] should be tuned to the specific application.

CHAPTER 5

RAPID AND SCALABLE LUBRICATION AND REPLENISHMENT OF LIQUID INFUSED MATERIALS

5.1 Introduction

Liquid infused surfaces (LIS) consist of a porous or textured solid matrix infused with a lubricating liquid.[6,7,131] The presence of a thin film of the lubricant on the exterior surface dramatically facilitates shedding of a wide range of liquids and solids, making LIS potential candidates for a variety of applications including prevention of fouling,[140,141,158,163–165] scaling[142,166], icing,[135,136,138,139,167] staining,[150] corrosion,[168–173] and chemical weapon absorption[151] as well as enhancement of the condensation rate of water[42–44] and other industrial liquids.[9] However, recent studies have shown that loss of the lubricating liquid leads to degradation of the low adhesion characteristic of LIS (see illustrative impinging water drop experiments on saturated and depleted LIS in Support Information).[133,136,141,151,174] Consequently, before LIS can transition into industrial use, durability issues posed by lubricant loss need to be addressed.

The functional liquid can drain away from the exterior of LIS in a variety of ways such as through shedding of lubricant "cloaked" condensate drops,[43] through slow evaporation at elevated temperatures,[141] through shear stresses posed by external fluid flow,[143,158,175,176] and through contact with another absorbing material[151] or even frost.[136,174] The degradation of the wetting characteristics of the outer surface of LIS can be temporarily slowed down by storing additional lubricant within the matrix[141,177] or by decreasing its release rate by selecting a polymeric matrix that swells with the lubricant.[139,141,151,158,164,165,167,178–180] Ultimately, however, a scalable lubricant

replenishment system is needed to sustain LIS performance through periodic re-lubrication. To date, the lubricant was most commonly infused into the matrix using "outside-in" approach that consists of soaking of the entire sample in a bath of the liquid (see schematic in Figure 1a). However, need of a bath that is larger than the sample makes adoption of approach outside of laboratory setting unlikely. As in the case of lubrication of the Nepenthes pitcher plant by rain,[181] other lubricating liquids could also be periodically sprayed to replenish the depleted LIS (see schematic in Figure 1a). Unfortunately, many liquid aerosols can pose health hazards; consequently, spray application of the lubricant might not be widely applicable.

An alternative to the "outside-in" re-lubrication method is an "inside-out" approach that resupplies the lubricant via an internal fluidic network within the matrix material. Provided a porous matrix, the liquid will diffuse from the inside of the fluidic channel through the matrix to re-lubricate the depleted exterior surface (see Figure 1b). Recently, internal lubricant replenishment systems consisting of microchannels within Polydimethylsiloxane (PDMS) mimicking vascularity of a plant leaf[141] and cotton microfibers encapsulated in the same type of polymeric matrix have been proposed. [151] In both of these cases, silicone oil was used as the lubricant because PDMS swells and slowly releases this liquid. Besides replenishing of the lubricant after depletion, an internal fluidic network within a polymeric matrix could also be used for rapid initial delivery of the lubricant. Ability to do so is particularly important in the case of LIS based hazardous material suits ("hazmat" suits) that are used for personal protection against chemical and biological threats. [151] In general, personal protective gear can be stored for extended periods of time without use. This results in a high possibility of lubricant loss from hazmat suits

that have been pre-lubricated during initial fabrication. In addition, personal protective gear is used in emergency situations and needs to be deployed rapidly. However, full saturation of a polymeric LIS using the "outside-in" lubricant bath approach can take several hours.[151] The schematic in Figure 1c shows that both of these issues could be addressed by integrating a lubricant distribution system directly within the hazmat suit and storing the liquid in an external pouch. With this setup, the user could lubricate or re-lubricate the suit by applying pressure to the pouch (e.g. stepping on it) just prior to deployment. In this work the impact of design of the vascularized solid polymeric matrix on lubrication dynamics and altering the wettability of the exterior surface is studied. Solid PDMS lubricated with Silicon oil is used as an illustrative lubricant-polymer LIS pair. Surface lubrication was studied by silicone oil using the "inside-out" mode from internal channels in a solid as well as microporous PDMS matrix (see schematics in Figure 1b). A third "inside-out-in" configuration is also proposed in which the lubricant is released from the internal channel onto the exterior surface through large periodically spaced vias (see schematic in Figure 1d). With proper geometrical design of the internal channels and via spacing, rapid flooding of the entire surface with a lubricant layer should be possible. Once on the surface, the liquid should instantaneously provide lubrication (i.e. provide non-adhesive properties) and slowly absorb into the polymer to provide a reserve in case of surface oil depletion. Prototypes of each of the illustrated three internal lubricant delivery systems were fabricated and to experimentally evaluate how effective they were at lubricating the exterior surface.

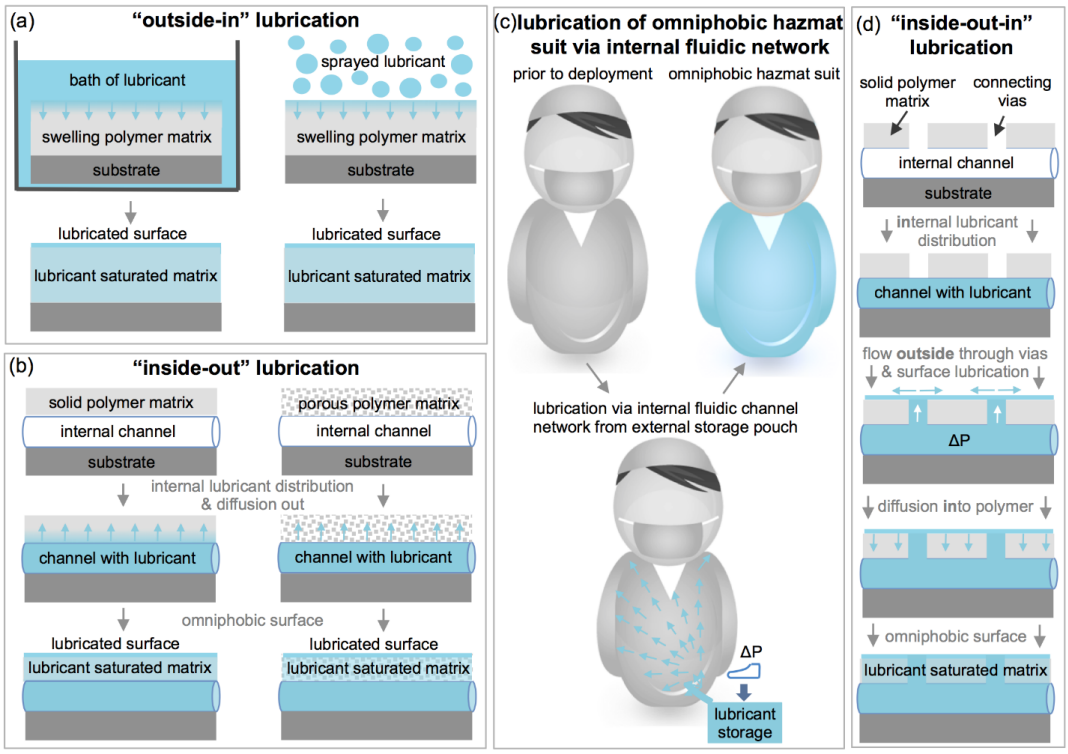

Figure 5.1. Schematics of various lubrication methods of liquid infused surfaces: (a) the common "outside-in" lubrication method achieved by soaking sample in bath of the liquid or alternatively spraying of the surface with the liquid, (b) "inside-out" lubrication method in which liquid is distributed through an internal fluidic network and diffuses through either the solid or microporous matrix to the external surface, (c) illustration of how such internal fluidic network could be applied to rapid lubricate a LIS based hazardous material (hazmat) suit, and (d) the proposed "inside-out-in" lubrication method in which lubricant is rapidly delivered to the surface from the internal channel using large periodically spaced vias.

5.2 Experimental

To fill in an internal channel, the silicone oil needs to travel length of the channel, L, within the filling time t. For a soon to be deployed hazmat suit, L and t were assumed to be ~1 m and ~20 s respectively, resulting in average flow velocity of $u_m \sim L/t \sim 0.05$ m/s. For

this average velocity, the flow of silicone oil with kinematic viscosity, ν, in the range of 5 to 100 cSt is laminar (i.e. Reynolds number, $\mathrm{Re}=u_m d/\nu<2000$) even with channel diameter, d, up to 0.2 m. To drive the flow of silicone oil in this viscosity range in channels with d of 10 to 100 μm, a pressure gradient, $\Delta P=32\rho\nu u_m L/d^2$ (ρ~1000 kg/m^3 is the oil density),[182] of ~1 GPa to ~1 MPa is needed. For a circular channel embedded within a rectangular PDMS slab such an internal pressure would lead to principal stresses within the solid that significantly exceed the tensile yield strength of the elastomers (for further discussion on this topic see finite element simulations results in Supporting Information). In contrast, in a millichannel with d of 1 mm only a ΔP of ~10 to 150 kPa is required to drive the flow, which would not lead to failure of the surrounding elastomer. Furthermore, a hazmat user can easily exert pressure in the range required to flow the oil through the millichannels by stepping on a small oil storage pouch or using a small mechanical pump. Consequently, the internal lubricant distribution system of a LIS based hazmat suit should consist of millichannels rather than the previously proposed microchannels. The latter design is more fitting for smaller systems such as microfluidic sensors or components of protective gear, such as lubricated gloves.

Prototypes of the three different internal lubrication schemes with 1.5 mm internal diameter channels were fabricated using Liu et al.[183] approach. In particular, mixed and degassed uncrosslinked PDMS was poured into a 3D printed 2.5 cm by 7.5 cm Acrylonitrile butadiene styrene (ABS) mold pierced with one or more 1.5 mm diameter stainless steel shafts. After thermal curing at 120°C for 15 min, the millichannels were created by manually removing the shafts from the rectangular PDMS slabs with thickness of ~3 mm (see Figure 2a). To fabricate the microporous matrix with interconnected ~1 to

200 μm diameter inclusions, a microdroplet-elastomer emulsion was created through high speed mixing of uncured 7.5 g of PDMS with 5 g of water at 5000 rpm for 10 minutes using overhead stirrer (Caframo, BDC6015).[184] During thermal curing within the ABS mold, the microdroplets evaporate leading to formation of interconnected micropores in the PDMS (see Figure 2b). To create a flat exterior surface, a glass slide was put on the top of the mold during curing. In turn, to fabricate a prototype of the "inside-out-in" architecture, ~400 μm diameter vias connecting the internal cylindrical channel to the top of the solid PDMS slab were manually fabricated by puncturing the elastomer using stainless steel syringe needles. The vias openings were separated by ~10 mm, which was iteratively determined as optimal separation distance for our particular sample size.

5.3 Results and Discussion

The change in wettability of the exterior surface of the samples due to subsurface lubricant transport was quantified through periodic contact angle hysteresis (CAH) measurements. Specifically, the schematic in Figure 2d shows that the prototypes were filled with 10 cSt silicone oil (Sigma-Aldrich) using a constant pressure syringe pump (Harvard apparatus) with imposed pressure. To test for any possible effects of the internal pressure, the experiments were conducted with imposed gauge pressure in the range of 1.3 to 37 kPa (10 to 280 mmHg). The contact angles were measured on a flat area that was immediately next to the bowed area above the pressurized channel (see Figure 2d). In order to simulate a realistic application, gravity effects were accounted for by lightly tilting the samples to ~5-10° during the experiments. The CAH was quantified by measuring advancing and receding contact angles using a goniometer (Rame-hart, model 290) with 6 repetitions per point (the shown error bars correspond to two-tailed T-student's distribution

with 90% confidence interval). The plot in Figure 2e shows that all samples initially had a high CAH in the range of 45 to 55° that corresponds to "dry" PDMS surface.[24] For the "inside-out" prototypes consisting of the solid PDMS matrix the value of the CAH remained mostly unaltered throughout the duration of the experiment (even up to 480 min, see also Figure S3a in SI), irrelevant of the imposed internal pressure. This result indicates that the lubricant did not diffuse through the 1.5 to 2 mm thick solid PDMS film separating the channel from the exterior measurement area (located to the side of the channel) within that time. This result is in agreement with the silicone oil diffusion dynamics observed during gravimetric analysis of the lubricant infusing from a bath into solid PDMS slabs (see Figure S3b in SI). Consequently, the large time scale for silicone oil diffusion through solid PDMS makes the "inside-out" approach impractical for rapid lubrication of larger systems such as a hazmat suit (that would require millichannel rather than microchannels to distribute the oil due to limits imposed by the pressure gradient needed to drive the flow). In addition, our further experiments have shown that use of the microporous PDMS did not resolve this issue for two reasons. First, oil transport throughout the slab was only mildly enhanced by presence of the micropores (see images in Figure S4). This likely occurs because the micropores interconnecting the spherical cavities in the matrix shrink due to PDMS swelling.[185,186] Second, in numerous tested samples, spontaneous leakage of the lubricant occurred due to a localized rupture of the matrix under pressure (see Figure S4). While the rapid transport of the oil to the surface caused by this failure is desired, the spontaneous and unpredictable rupture of the sample is not. The distribution of the oil using the new "inside-out-in" scheme also results in nearly instantaneous release of the liquid onto the exterior surface, however, in a highly controlled manner and without any damage

to the solid matrix. Naturally, release of the lubricant decreases the CAH from the "dry" range of 45° to 55° to the "wet" state that is below 5° (see Figure 2e). However, all the CAH gradually increased because the excess oil drained away from the surface prior to full saturation of the PDMS matrix. To illustrate the effects of excess oil draining, ~1.5 mL of the oil was released onto the surface in two routes: single pulse with 4 s duration and four pulses with 1 s duration each separated by 60 min intervals. Within 30 and 60 min of the single 4 s pulse, the CAH increased to ~20° and ~30°, respectively. A nearly identical trend was observed after the first 1 s pulse, indicating that the amount of oil released during the longer pulse was excessive. Similarly, the dramatic CAH decrease followed by its gradual increase was observed after each of the subsequent 1 s pulses. However, the maximum value of the CAH decreased with each pulse, settling on ~10° after the 4^{th} pulse. Since this low CAH value is in the range observed for fully silicone oil saturated PDMS,[24] releasing of the oil in four shorter pulses provides a better approach than does the single longer pulse.

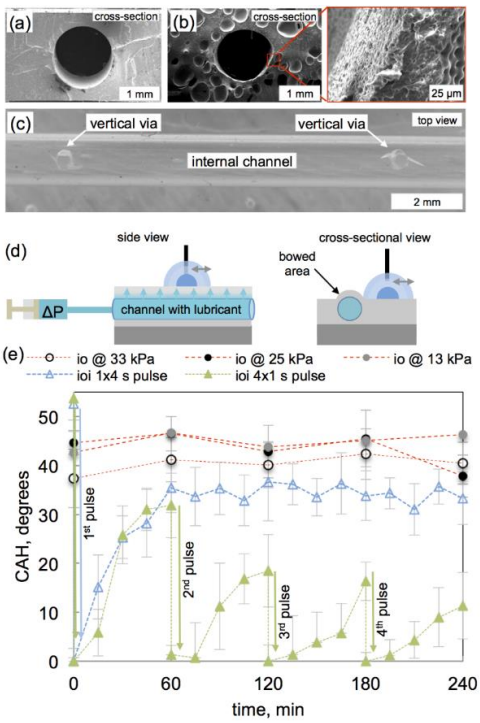

Figure 5.2 Fabricated prototypes and contact angle hysteresis (CAH) measurements: cross-sectional SEM images of sample architecture for the "inside-out" (i-o at different internal pressures) lubrication method with cylindrical millichannel in (a) solid and (b) microporous PDMS; (c) optical top down image of sample architecture for the "inside-out-in" (i-o-i) lubrication method illustrating periodically spaced vertical vias to the internal channel; and (d) schematic and (e) results of the contact angle hysteresis measurements.

To further contrast the dynamics of the "inside-out" and "inside-out-in" LIS lubrication approaches, multichannel prototypes were fabricated and tested. The schematic in Figure 3a shows that these samples were mounted vertically and exposed to a short spray of dyed water.[24] Figure 3b and 3c show images of water drops that adhered to the surface of the two prototypes after exposure to the spray at different stages of the lubrication process. In the case of the "inside-out" prototype pressurized to 37 kPa, the adhered droplet distribution remaining after spray tests conducted in 1 h intervals did not change

appreciably for the first 3 h. In particular, the threshold drop diameter for shedding was 5.2 ± 0.4 mm, 4.9 ± 0.4 mm, and 5.1 ± 0.3 mm at the start, and after 1 h and 2 h of the experiment, respectively. After 3 h of the experiments, the sprayed drops began to predominately shed in the valleys in-between the channels. It is schematically illustrated in Figure 3d that this likely occurred because the tops of the channels were bowed and by that time slippery (see also Movie 1). In contrast the rapid release of the oil onto the surface in the "inside-out-in" prototype led to a dramatic decrease in total number and size of sprayed drops adhering to the surface in the "dry" and "wet" state (see Figure 3c and Movie 2). In this case the threshold drop-shedding diameter decreased from 5.4±0.1 mm in the dry to state to 0.26±0.03 mm in the wet state within just a few seconds of the lubrication process. This value of the threshold drop-shedding diameter is the same as the one measured for a fully saturated PDMS sample (0.23±0.07 mm after 24 h oil soaking). In agreement with the CAH experiments, after the dramatic initial decrease, the threshold drop departure diameter gradually increased, reaching a value of 3.7±0.1 mm after 1 h. Consequently, multiple short lubrication pulses are required to fully saturate the polymer with the lubricant and induce robust low adhesive characteristics of the LIS.

Rapid discharge of the lubricant could lead to excessive liquid loss due to gravitational draining. In order to estimate conditions that would minimize lubricant waste, oil absorption rate was measured into 2.5 by 2.5 cm PDMS films. When exposed to a bath of a lubricant from a single side, oil absorption into PDMS is linear in the first 30 min, with an absorption flux of about 12 $\mu g/cm^2 s$ (for longer time scales the absorption rate decreases[24]). Next, absorbed retention of silicone oil released onto PDMS slabs was measured. Specifically, the 0.93 g (1 mL) of oil was dripped, which is estimated to be

required to fully saturated the top part of the samples, onto PDMS slabs at rates of ~15.5 to 1550 μg/s. The 2.5 by 7.5 cm slabs were tilted at 45°, which resulted in the dripped oil spreading over about 50% of the sample area and dispensing fluxes in the range of 1.7 to 170 μg/cm^{2}s (oil dispensed from individual vias can cover such area, see further discussion in Support Information). By measuring the mass of the sample before and after oil release, it was possible to determine the amount of retained oil. The highest oil retention of about 35% occurred at the lowest dispensing flux of 1.7 μg/cm^{2}s. With increased dispensing rate, the oil retention rate decreased nearly exponentially, settling at about 5% for 170 μg/cm^{2}s (see Support Information for further details). Therefore, conservation of the lubricating liquid dispensed onto a tilted sample is possible only at very low dispensing rates that are balanced by the absorption rate. At these low dispensing rates full saturation of the polymer takes as much time as lubrication using the "inside-out" approach. Consequently, the latter approach is preferred for applications in which lubricant conservation is more important than the lubrication time.

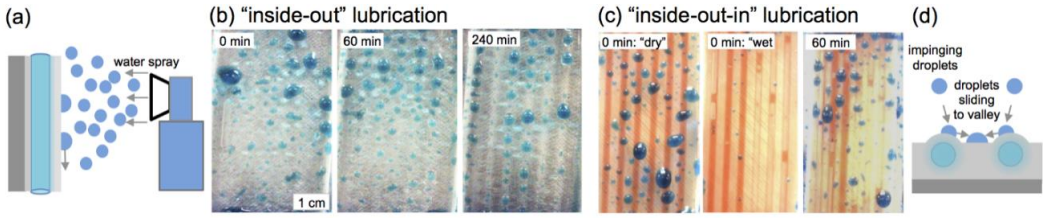

Figure 5.3. (a) schematic and (b & c) images of sprayed water drops adhering to PDMS samples with multiple internal millichannels at various stages of (b) inside-out and (c) inside-out-in lubrication, and (d) schematic showing mechanisms of sprayed droplet migration to valleys in-between bowed channels. In (c) silicone oil was dyed red to facilitate interpretation and parts of the channel were filled with air once the lubricant in the pump was depleted.

5.4 Conclusions

In summary, the "inside-out-in" system for rapid lubrication or re-lubrication of polymeric LIS is introduced. The system consists of an internal millichannel distribution network connected to the surface using periodically spaced vias and could be used to, for example, lubricate LIS based personal protective gear. Our experiments showed that this system lubricates the exterior LIS surface nearly instantaneously resulting in a CAH below 5° and threshold drop departure diameter below 0.3 mm. In addition, this system provides a possibility of prolonged LIS performance due to lubricant absorption into the exterior surface of the polymer over multiple oil pulses. In contrast, the previously discussed "inside-out" system without the connecting vias only partially lubricated the surface within 8 h, irrelevant of the applied internal pressure of the oil. It is also shown that use of microporous polymer matrix does not necessarily improve the performance of "inside-out" system. In particular, the fabricated microporous PDMS prototypes were prone to mechanical failure under the imposed pressure and unpredictable oil release. While an alternative fabrication approach could produce a more robust microporous matrix around the millichannels, fabrication of the introduced "inside-out-in" architecture is simple and inherently includes the flat exterior surface desired for low CAH.[24]

It should be noted that prior to use of the "inside-out-in" system, analysis tailoring its design to the specific application should be performed to avoid excessive flow rates that could lead to waste of the liquid. For example, if the released oil can be drained due to gravitational forces, periodically sequenced multiple short oil pulses must be applied to saturate the polymer. However, our experiments showed that even at slow oil dispensing rates, slow absorption rate of silicone oil into PDMS will result in waste of majority of the

oil. Consequently, the "inside-out" approach should be implemented for applications in which lubricant conservation is more important than the lubrication time. In another example illustrated in Figure S7 and S8, excessive liquid velocities across a via can lead to jetting, rather than the desired filmwise spreading, of the lubricant. Since $u_m = \Delta P d^2/\rho \nu L$, such behavior could be avoided by inversely matching the via diameters to the local pressure drop (see detailed discussion of this topic in Support Information). Lastly, the system should be designed to minimize required lubricant use by utilizing lubricant-spreading mechanisms present in particular scenario. For example, in the case of the hazmat suit the number of required vias could be decreased if majority of the oil is dispensed towards the top of the suit and oil spreads over majority of the surface through gravitational draining. In case of an airplane wing, as in dispensing of antifreeze by the commercial "Weeping wing" system,[187] the lubricant could be dispensed through vias in the leading edge and spread over the rest of the wing through air motion. In all, the proposed inside-out-in lubricant dispensing system provides another scalable route to refresh wetting properties of LIS and could facilitate translation of these materials into industrial use.

CHAPTER 6

CONCLUSIONS AND FUTURE WORK

6.1 Summary of the Dissertation

Many defense, healthcare, and energy applications can benefit from the development of surfaces that easily shed droplets of liquids of interest. Droplet movability across the surface is typically quantified in terms of contact angle hysteresis. Higher magnitude of hysteresis indicates higher droplet adhesion to the surface which can be lowered by tailoring surface chemistry or topography or both typically through surface modifications. Despite significant efforts, exterior surfaces are prone to physical damage, which in turn can degrade the surface modification that ultimately results in loss of desired surface wettability. Therefore, to avoid durability issues of surface modification techniques, this thesis focuses on altering bulk composition and interior of the material to tune how exterior surface would interact with liquids that is termed as 'bulk engineering'. In this dissertation, fundamental and applied aspects of engineering of two material systems with low contact angle hysteresis fabricated using bulk engineering are described.

In the first half of the thesis, in Chapter 2, water-shedding metal matrix-hydrophobic nanoparticle composites with high thermal conductivity for steam condensation rate enhancement are described. In this work, it is argued that metal matrix composites with hydrophobic nanoparticles could provide an attractive alternative to hydrophobic thin film materials for enhancing water condensation rate by promoting the dropwise mode. There are several key findings of my experimental and theoretical investigation. It is concluded that, in the case of such composites, diameter and spacing of hydrophobic nanoparticles are critical to alter the condensation mode and need to be much

smaller than average center-to-center spacing in-between closest neighboring drops prior to coalescence dominated growth stage (e.g. diameters of ~100 to 200 nm as in experiments). Calculations showed that a substantial heat transfer enhancement (two fold and higher) can be achieved even by using copper and aluminum matrix composites fully loaded with PTFE nanoparticles (maximum volume fraction ~ 0.64) to promote DWC if their thickness is below ~0.5 mm. Arguments are provided showing that using much higher nanoparticle density will not negate the heat transfer enhancement attained via DWC. Importantly I show that surfaces do not necessarily have to be hydrophobic to promote DWC, but rather they need to have a low CAH. Desired low CAH can be attained with significantly lower hydrophobic nanoparticle density than that required to make the surface hydrophobic. The likely explanation for this observation is that the nano-scale hydrophobic phase on the surface facilitates the droplet movement during coalesce and gravity assisted shedding. Hence it is hypothesized that contortions formed in the three phase contact line (TPCL) i.e. droplet perimeter affects the local energetics which in turn modifies the droplet movement on heterogeneous surface. This hypothesis is experimentally explored by investigating wettability of surfaces having chemical heterogeneity of different length scales, details of which are given in Chapter 3.

Specifically, in Chapter 3, the effect of number of contortions in the TPCL on CAH value was studied by varying the width of alternate hydrophilic-hydrophobic strip over three orders of magnitude (0.4 μm to 100 μm). It was concluded that the number of kinks do not have a significant impact on modifying the CAH value compared to the shape of the droplet where both number of kinks and shape of the droplet depend on the strip width. Furthermore, altering the droplet shape was shown to reduce in the pinning length of the

TPCL over two orders of magnitude, which results in near wetting isotropy for nano-striped surface. Loss in wetting heterogeneity was subsequently confirmed via performing series of droplet impact, condensation, and droplet sliding experiments. Two distinct mechanisms observed while TPCL receded parallel and perpendicular to strips during droplet evaporation are described. In particular, motion parallel to striping was continuous where TPCL motion had discontinuous stick-slip events in perpendicular direction. It was also pointed out that, contrary to the Shanahan's theory, pinning force acting on the TPCL was found to vary linearly with strip width while moving perpendicular to striping.

In the second half of the thesis, development of all-liquid shedding lubricant-swollen polymeric omniphobic protective gear for defense and healthcare applications is described. In chapter 4, it is exhibited that the protective gear if made from polymeric material fully saturated with lubricant can shed all liquids irrespective of their surface tensions even after multiple contact incidences with the foreign objects (mimicked by highly absorbing porous wipe). It is demonstrated that oil retention near the exterior surface as well as surface topology dictate whether lubricated fabrics remain omniphobic. In particular, oil soaked PDMS modified fabrics with flat topography was found to have more robust omniphobic characteristics even after 10 contact experiments compared to PDMS modified fabrics with micro-textured topology or nanoparticle coated fabrics previously proposed in the literature. Experiments also illustrated that the proposed material not only resist penetration of ethanol spray but also can be completely cleaned off from ethanol micro-droplets within a few seconds of moderate airflow. Although, fabrication of the robust and durable omniphobic lubricated polymeric fabrics is simple and easily scalable, two challenges need to be addressed before such system can be used in application.

Specifically, it was found that the time required for lubrication or re-lubrication was very high making them unsuitable for time sensitive healthcare or military applications. Furthermore, oil required for proposed system to work was very high. A solution to address these issue was put forth which is discussed in Chapter 5.

In Chapter 5, the “inside-out-in” system is introduced for rapid lubrication or re-lubrication of polymeric LIS. Specifically, the system consists of a subsurface lubricant (silicone oil) distribution network consists of millichannels in the PDMS matrix connected to the surface (exterior of the PDMS) using periodically spaced vias. Experiments showed that such system lubricates the exterior lubricant infused surface (LIS) nearly instantaneously resulting in a CAH below 5° and the threshold drop departure diameter below 0.3 mm. In addition, this system provides a possibility of prolonged LIS performance due to lubricant absorption into the exterior surface of the polymer over multiple oil pulses. However, inside-out-in system was prone to lubricant waste due to drainage of lubricant under gravity predominately because of slow absorption rate of silicone oil into PDMS. Therefore, the alternative approach of inside-out scheme, that consists of a subsurface millichannel distribution PDMS matrix, should be implemented for applications in which lubricant conservation is more important than the lubrication time. It was found that the response time for such system is extremely high and with the present design, part of the area of the exterior surface between the adjacent millichannels remain non-slippery. Therefore, there is a trade-off between lubrication time and amount of lubricant required to render the surface omniphobic. In all, the proposed inside-out-in lubricant dispensing system provides another scalable route to refresh wetting properties

of lubricant infused surfaces and could facilitate translation of these materials into industrial use.

6.2 Recommendations for Future Work

1. In the first half of the thesis, it was argued that, metal matrix hydrophobic nanoparticle composite with the size and center-to-center pitch significantly smaller than ~5 μm can promote sustained dropwise condensation. In turn, such composite with thickness <0.5 mm can double the value of heat transfer coefficient compared to film-wise condensation due to high thermal conductivity. Hence it will be interesting to fabricate such composites through co-electrodeposition and investigate their thermal properties. Conducting steady state condensation experiments will reveal if such composites can sustain DWC or surface roughness of the composites assists rapid dropwise to filmwise transition. Furthermore, testing mechanical properties of the composites will also be crucial if such composites are to be successfully deployed in an industrial setting.

2. The work in Chapter 3 revealed that, number of contortions in TPCL do not have a significant role in dictating the value of CAH as compared to droplet shape. Moreover, wetting anisotropy was found to nearly disappear for nano-scale striped surface which was later confirmed through condensation, droplet impact and water droplet sliding experiments. It was also pointed out that, pinning force acting on the TPCL while moving perpendicular to striping was found to contradict the Shanahan's theory. There is a clear need to systematically investigate the droplet motion on striped surface. In-situ investigation of pinning-depinning events of advancing and receding TPCL parallel and perpendicular to striping using confocal microscopy in conjunction with quantifying depinning force with the Wilhelmy plate apparatus can be exciting. Confocal microscopy

can also be used to study the heterogeneity length scale- contortion geometry dependency and quantify the local variation in static contact angle along the length of TPCL. Furthermore, while near wetting isotropy for heterogeneous surface was confirmed through variety of liquid-surface interaction experiments, it will be really interesting to see how such surfaces work in a biological setting. Specifically, studying effect of length scale of chemical heterogeneity on adhesion of biological agents can open new avenues in anti-biofouling surfaces or biofuels application.

3. Lubricant saturated PDMS modified fabric composite was shown to be a potentially robust omniphobic material for protective gear application in Chapter 4. In Chapter 5, Couple of methods for easy and rapid lubrication and re-lubrication of such material were proposed. First, methods such as dip-coating should be tested to modify larger surface areas with PDMS while keeping the exterior flat if such material is to be used in the real-life application. Furthermore, although proposed inside-out and inside-out-in methods look promising, they need to be improved. For instance, instead of using straight channels, spiral channels or mesh like channels should be tested in inside-out scheme to improve the lubricant transport to the exterior surface. For inside-out-in system, experiments need to be performed with a lubricant-polymer combination where diffusivity of lubricant in polymer is extremely high to investigate if it reduces the lubricant wastage.

This work resulted in following journal publications:

1. Damle, V. and Rykaczewski, K. Nano-striped chemically anisotropic surfaces have near isotropic wettability, (In submission).

2. Damle, V., Uppal, A., Xiaoda Sun, X., Burgin, T. P. and Rykaczewski, K. On rapid and scalable lubrication and replenishment of liquid infused materials, *Surface Innovations* ***2016***, 4 (2), 102-108.

3. Damle, V., Sun, X. and Rykaczewski, K. Can Metal Matrix-Hydrophobic Nanoparticle Composites Enhance Water Condensation by Promoting the Dropwise Mode?, *Advance Materials Interfaces* **2015**, 2, 1500202.

4. Damle, V., Chandrashekar, S., Tummala A., Kido, C., Roopesh, A., Sun, X., Doudrick, K., Chinn, J., Lee, J. R., Burgin, T. P., and Rykaczewski, K. "Insensitive" to Touch: Fabric-Supported Lubricant-Swollen Polymeric Films for Omniphobic Personal Protective Gear, *Applied Materials Interfaces* **2015**, 7 (7), 4224–4232.

Following conference presentations were also resulted from this dissertation:

1. Damle, V., Uppal, A., Xiaoda Sun, X., Burgin, T. P. and Rykaczewski, K. On rapid and scalable lubrication and replenishment of Hazardous Materials Suits. 2016 MRS Spring Meeting, Phoenix, AZ 3/2016.

2. Damle, V., Sun, X., and Rykaczewski, K., Condensation Dynamics on Mimicked Metal Matrix Hydrophobic Nanoparticle-Composites. 2015 MRS Spring Meeting, San Francisco, CA, 4/2015.

3. Damle, V., Sun, X., and Rykaczewski, K., Condensation Dynamics on Mimicked Metal Matrix Hydrophobic Nanoparticle-Composites. 67th APS DFD Meeting, San Francisco, CA, 12/2014.

4. Damle, V., Sun, X., and Rykaczewski, K., Metal Matrix Hydrophobic Nano-Composites for Sustainable Condensation Rate Enhancement, poster presented at 2014 Arizona Imaging and Microanalysis Society Meeting, Tempe, AZ, 3/2014.

REFERENCES

(1) Quéré, D. Non-Sticking Drops. *Reports Prog. Phys.* **2005**, *68* (11), 2495–2532.

(2) Quéré, D. Wetting and Roughness. *Annu. Rev. Mater. Res.* **2008**, *38* (1), 71–99.

(3) Wenzel, R. N. Resistance of Solid Surfaces to Wetting by Water. *J. Ind. Eng. Chem. (Washington, D. C.)* **1936**, *28*, 988–994.

(4) Tuteja, A.; Choi, W.; Ma, M.; Mabry, J. M.; Mazzella, S. A.; Rutledge, G. C.; McKinley, G. H.; Cohen, R. E. Designing Superoleophobic Surfaces. *Science* **2007**, *318* (5856), 1618–1622.

(5) Tuteja, A.; Choi, W.; Mabry, J. M.; McKinley, G. H.; Cohen, R. E. Robust Omniphobic Surfaces. *Proc. Natl. Acad. Sci. U. S. A.* **2008**, *105* (47), 18200–18205.

(6) Wong, T.-S.; Kang, S. H.; Tang, S. K. Y.; Smythe, E. J.; Hatton, B. D.; Grinthal, A.; Aizenberg, J. Bioinspired Self-Repairing Slippery Surfaces with Pressure-Stable Omniphobicity. *Nature* **2011**, *477* (7365), 443–447.

(7) Smith, J. D.; Dhiman, R.; Anand, S.; Reza-Garduno, E.; Cohen, R. E.; McKinley, G. H.; Varanasi, K. K. Droplet Mobility on Lubricant-Impregnated Surfaces. *Soft Matter* **2013**, *9* (6), 1772–1780.

(8) Paxson, A. T.; Yagüe, J. L.; Gleason, K. K.; Varanasi, K. K. Stable Dropwise Condensation for Enhancing Heat Transfer via the Initiated Chemical Vapor Deposition (iCVD) of Grafted Polymer Films. *Adv. Mater.* **2014**, *26* (3), 418–423.

(9) Rykaczewski, K.; Paxson, A. T.; Staymates, M.; Walker, M. L.; Sun, X.; Anand, S.; Srinivasan, S.; McKinley, G. H.; Chinn, J.; Scott, J. H. J.; Varanasi, K. K. Dropwise Condensation of Low Surface Tension Fluids on Omniphobic Surfaces. *Sci. Rep.* **2014**, *4*, 4158.

(10) Bovero, E.; Krahn, J.; Menon, C. Fabrication and Testing of Self Cleaning Dry Adhesives Utilizing Hydrophobicity Gradient. *J. Bionic Eng.* **2015**, *12* (2), 270–275.

(11) Zamuruyev, K. O.; Bardaweel, H. K.; Carron, C. J.; Kenyon, N. J.; Brand, O.; Delplanque, J. P.; Davis, C. E. Continuous Droplet Removal upon Dropwise Condensation of Humid Air on a Hydrophobic Micropatterned Surface. *Langmuir* **2014**, *30* (33), 10133–10142.

(12) Hu, J.; Xu, K.; Wu, Y.; Lan, B.; Jiang, X.; Shu, L. The Freezing Process of Continuously Sprayed Water Droplets on the Superhydrophobic Silicone Acrylate Resin Coating Surface. *Appl. Surf. Sci.* **2014**, *317*, 534–544.

(13) Zhang, H.; Zhao, Y.; Lv, R.; Yang, C. Freezing of Sessile Water Droplet for Various Contact Angles. *Int. J. Therm. Sci.* **2016**, *101*, 59–67.

(14) Kim, M. K.; Cha, H.; Birbarah, P.; Chavan, S.; Zhong, C.; Xu, Y.; Miljkovic, N. Enhanced Jumping-Droplet Departure. *Langmuir* **2015**, *31* (49), 13452–13466.

(15) Boreyko, J. B.; Hansen, R. R.; Murphy, K. R.; Nath, S.; Retterer, S. T.; Collier, C. P. Controlling Condensation and Frost Growth with Chemical Micropatterns. *Sci. Rep.* **2016**, *6*, 1–15.

(16) Wang, S.; Wang, T.; Ge, P.; Xue, P.; Ye, S.; Chen, H.; Li, Z.; Zhang, J.; Yang, B. Controlling Flow Behavior of Water in Microfluidics with a Chemically Patterned Anisotropic Wetting Surface. *Langmuir* **2015**, *31* (13), 4032–4039.

(17) Ghosh, A.; Beaini, S.; Zhang, B. J.; Ganguly, R.; Megaridis, C. M. Enhancing Dropwise Condensation through Bioinspired Wettability Patterning. *Langmuir* **2014**, *30* (43), 13103–13115.

(18) Öner, D.; McCarthy, T. J. Ultrahydrophobic Surfaces. Effects of Topography Length Scales on Wettability. *Langmuir* **2000**, *16* (20), 7777–7782.

(19) Paxson, A. T.; Varanasi, K. K. Self-Similarity of Contact Line Depinning from Textured Surfaces. *Nat. Commun.* **2013**, *4*, 1492.

(20) Raj, R.; Enright, R.; Zhu, Y.; Adera, S.; Wang, E. N. Unified Model for Contact Angle Hysteresis on Heterogeneous and Superhydrophobic Surfaces. *Langmuir* **2012**, *28* (45), 15777–15788.

(21) Oliver, J. F.; Huh, C.; Mason, S. G. The Apparent Contact Angle of Liquids on Finely-Grooved Solid Surfaces-A SEM Study. *J. Adhes.* **1976**, *8* (3), 223–234.

(22) Gauthier, A.; Rivetti, M.; Teisseire, J.; Barthel, E. Role of Kinks in the Dynamics of Contact Lines Receding on Superhydrophobic Surfaces. *Phys. Rev. Lett.* **2013**, *110* (4), 1–5.

(23) Rivetti, M.; Teisseire, J.; Barthel, E. Surface Fraction Dependence of Contact Angles Induced by Kinks in the Triple Line. *Phys. Rev. Lett.* **2015**, *115* (1), 1–5.

(24) Gennes, P.-G. de; Brochard-Wyart, F.; Quéré, D. *Capillarity and Wetting Phenomena: Drops, Bubbles, Pearls, Waves*; Springer, 2003.

(25) Gorzkowska-Sobas, A. A. *Chemical Warfare Agents and Their Interactions with Solid Surfaces*; Rapport 00574; Norwegian Defense Research Establishment: Kjeller, Norway, 2013.

(26) Center for Disease Control. I*nfection Prevention and Control Recommendations for Hospitalized Patients with Known or Suspected Ebola Virus Disease in U.S. Hospitals;* available at: http://www.cdc.gov/vhf/ebola/hcp/infection-prevention-and-control-recommendations.html. (accessed Nov 1, 2014)

(27) Brevett, C. A.; Pence, J. J.; Nickol, R. G.; Maloney, E. L.; Myers, J. P.; Giannaras, C. V.; Sumpter, K. B.; King, B. E.; Hong, S. H.; Durst, H. *Evaporation Rates of Chemical Warfare Agents Measured Using 5 cm Wind Tunnels III. Munition-Grade Sulfur Mustard on Concrete*; DTIC Document; US Army: Aberdeen Proving Ground, MD, 2010.

(28) Stebbins, A. A. Can Naval Surface Forces Operate Under Chemical Weapons Conditions? Master's Thesis, Naval Postgraduate School, Monterey, Calif., 2002.

(29) Schmidt, E. Schurig, W. Sellschopp, W. Forschung Im Ingenieurwesen. **1930**, *1*, 53.

(30) Rose, J. W. Dropwise Condensation Theory and Experiment: A Review. *Proc. Inst. Mech. Eng. Part A J. Power Energy* **2005**, *216* (2), 115–128.

(31) Müller-Steinhagen, H.; Zhao, Q. Investigation of Low Fouling Surface Alloys Made by Ion Implantation Technology. *Chem. Eng. Sci.* **1997**, *52* (19), 3321–3332.

(32) Rausch, M. H.; Fröba, a. P.; Leipertz, a. Dropwise Condensation Heat Transfer on Ion Implanted Aluminum Surfaces. *Int. J. Heat Mass Transf.* **2008**, *51* (5–6), 1061–1070.

(33) Rausch, M. H.; Leipertz, a.; Fröba, a. P. Dropwise Condensation of Steam on Ion Implanted Titanium Surfaces. *Int. J. Heat Mass Transf.* **2010**, *53* (1–3), 423–430.

(34) Bani Kananeh, A.; Rausch, M. H.; Fröba, A. P.; Leipertz, A. Experimental Study of Dropwise Condensation on Plasma-Ion Implanted Stainless Steel Tubes. *Int. J. Heat Mass Transf.* **2006**, *49* (25–26), 5018–5026.

(35) Blackman, L. C. F.; Dewar, M. J. S.; Hampson, H. An Investigation of Compounds Promoting the Dropwise Condensation of Steam. *J. Appl. Chem* **1957**, *7*, 160.

(36) Perkins, K. P. *DTIC Document*; 1979.

(37) Woodruff, D. W.; Westwater, J. W. Steam Condensation on Electroplated Gold: Effect of Plating Thickness. *Int. J. Heat Mass Transf.* **1979**, *22* (4), 629–632.

(38) O'neill, G. a.; Westwater, J. W. Dropwise Condensation of Steam on Electroplated Silver Surfaces. *Int. J. Heat Mass Transf.* **1984**, *27* (9), 1539–1549.

(39) Marto, P. J.; Looney, D. J.; Rose, J. W.; Wanniarachchi, a. S. Evaluation of Organic Coatings for the Promotion of Dropwise Condensation of Steam. *Int. J. Heat Mass Transf.* **1986**, *29* (8), 1109–1117.

(40) Qi, Z.; Dongchang, Z.; Jifang, L. Surface Materials with Dropwise Condensation Made by Ion Implantation Technology. *Int. J. Heat Mass Transf.* **1991**, *34* (11), 2833–2835.

(41) Azimi, G.; Dhiman, R.; Kwon, H.-M.; Paxson, A. T.; Varanasi, K. K. Hydrophobicity of Rare-Earth Oxide Ceramics. *Nat. Mater.* **2013**, *12* (4), 315–320.

(42) Anand, S.; Rykaczewski, K.; Subramanyam, S. B.; Beysens, D.; Varanasi, K. K. How Droplets Nucleate and Grow on Liquids and Liquid Impregnated Surfaces. *Soft Matter* **2015**, *11* (1), 69–80.

(43) Anand, S.; Paxson, A. T.; Dhiman, R.; Smith, J. D.; Varanasi, K. K. Enhanced Condensation on Lubricant-Impregnated Nanotextured Surfaces. *ACS Nano* **2012**, *6* (11), 10122–10129.

(44) Xiao, R.; Miljkovic, N.; Enright, R.; Wang, E. N. Immersion Condensation on Oil-Infused Heterogeneous Surfaces for Enhanced Heat Transfer. *Sci. Rep.* **2013**, *3*, 1988.

(45) Nosonovsky, M.; Hejazi, V.; Nyong, A. E.; Rohatgi, P. K. Metal Matrix Composites for Sustainable Lotus-Effect Surfaces. *Langmuir* **2011**, *27* (23), 14419–14424.

(46) Drelich, J.; Miller, J. D.; Kumar, A.; Whitesides, G. M. Wetting Characteristics of Liquid Drops at Heterogeneous Surfaces. *Colloids Surfaces A Physicochem. Eng. Asp.* **1994**, *93*, 1–13.

(47) Drelich, J.; Wilbur, J. L.; Miller, J. D.; Whitesides, G. M. Contact Angles for Liquid Drops at a Model Heterogeneous Surface Consisting of Alternating and Parallel Hydrophobic/Hydrophilic Strips. *Langmuir* **1996**, *12* (7), 1913–1922.

(48) Lopez, G. P.; Biebuyck, H. a; Frisbie, C. D.; Whitesides, G. M. Imaging of Features. *Science* **1993**, *260*, 647–649.

(49) Kumar, a; Whitesides, G. M. Patterned Condensation Figures as Optical Diffraction Gratings. *Science* **1994**, *263* (5143), 60–62.

(50) Morita, M.; Koga, T.; Otsuka, H.; Takahara, A. Macroscopic-Wetting Anisotropy on the Line-Patterned Surface of Fluoroalkylsilane Monolayers. *Langmuir* **2005**, *21* (3), 911–918.

(51) Parker, A. R.; Lawrence, C. R. Water Capture by a Desert Beetle. *Nature* **2001**, *414*, 33–34.

(52) Zhai, L.; Berg, M. C.; Cebeci, F.; Kim, Y.; Milwid, J. M.; Rubner, M. F.; Cohen, R. E.; Fevzi, C. Patterned Superhydrophobic Surfaces : Toward a Synthetic Mimic of the Namib Desert Beetle. *Nano Lett.* **2006**, *6* (6), 1213–1217.

(53) Varanasi, K. K.; Hsu, M.; Bhate, N.; Yang, W.; Deng, T. Spatial Control in the Heterogeneous Nucleation of Water. *Appl. Phys. Lett.* **2009**, *95* (9), 1–4.

(54) Mishchenko, L.; Hatton, B.; Bahadur, V.; Taylor, J. A.; Krupenkin, T.; Aizenberg, J. Design of Ice-Free Nanostructured Surfaces Based on Repulsion of Impacting Water Droplets. *ACS Nano* **2010**, *4* (12), 7699–7707.

(55) Mishchenko, L.; Khan, M.; Aizenberg, J.; Hatton, B. D. Spatial Control of Condensation and Freezing on Superhydrophobic Surfaces with Hydrophilic Patches. *Adv. Funct. Mater.* **2013**, *23* (36), 4577–4584.

(56) He, M.; Zhou, X.; Zeng, X.; Cui, D.; Zhang, Q.; Chen, J.; Li, H.; Wang, J.; Cao, Z.; Song, Y.; Jiang, L. Hierarchically Structured Porous Aluminum Surfaces for High-Efficient Removal of Condensed Water. *Soft Matter* **2012**, *8* (25), 6680.

(57) Anderson, D. M.; Gupta, M. K.; Voevodin, A. A.; Hunter, C. N.; Putnam, S. A.; Tsukruk, V. V.; Fedorov, A. G. Using Amphiphilic Nanostructures to Enable Long-Range Ensemble Coalescence and Surface Rejuvenation in Dropwise Condensation. *ACS Nano* **2012**, *6* (4), 3262–3268.

(58) Yao, C. W.; Garvin, T. P.; Alvarado, J. L.; Jacobi, a. M.; Jones, B. G.; Marsh, C. P. Droplet Contact Angle Behavior on a Hybrid Surface with Hydrophobic and Hydrophilic Properties. *Appl. Phys. Lett.* **2012**, *101* (11).

(59) Vonna, L.; Haidara, H. Soft Matter Structures on a Series of Self-Similar Micropatterned. *Soft Matter* **2013**, *9*, 765–771.

(60) Chen, X.; Ma, R.; Zhou, H.; Zhou, X.; Che, L.; Yao, S.; Wang, Z. Activating the Microscale Edge Effect in a Hierarchical Surface for Frosting Suppression and Defrosting Promotion. *Sci. Rep.* **2013**, *3*, 2515.

(61) Chen, X.; Wu, J.; Ma, R.; Hua, M.; Koratkar, N.; Yao, S.; Wang, Z. Nanograssed Micropyramidal Architectures for Continuous Dropwise Condensation. *Adv. Funct. Mater.* **2011**, *21* (24), 4617–4623.

(62) Hou, Y.; Yu, M.; Chen, X.; Wang, Z.; Yao, S. Recurrent Filmwise and Dropwise Condensation on a Beetle Mimetic Surface. *ACS Nano* **2015**, *9* (1), 71–81.

(63) Zhao, H.; Beysens, D. From Droplet Growth to Film Growth on a Heterogeneous Surface: Condensation Associated with a Wettability Gradient. *Langmuir* **1995**, *11* (2), 627–634.

(64) Medici, M.-G.; Mongruel, A.; Royon, L.; Beysens, D. Edge Effects on Water Droplet Condensation. *Phys. Rev. E* **2014**, *90* (6), 1–12.

(65) Beysens, D. Dew Nucleation and Growth. *Comptes Rendus Phys.* **2006**, *7* (9–10), 1082–1100.

(66) Beysens, D. The Formation of Dew. *Atmos. Res.* **1995**, *39*, 215–237.

(67) Beysens, D.; Knobler, C. M. Growth of Breath Figures. *Phys. Rev. Lett.* **1986**, *57* (12), 1433–1436.

(68) Beysens, D.; Knobler, C. M.; Schaffar, H. Scaling in the Growth of Aggregates on a Surface. *Phys. Rev. B* **1990**, *41* (14), 9814–9818.

(69) Enright, R.; Miljkovic, N.; Al-Obeidi, A.; Thompson, C. V; Wang, E. N. Condensation on Superhydrophobic Surfaces: The Role of Local Energy Barriers and Structure Length Scale. *Langmuir* **2012**, *28* (40), 14424–14432.

(70) Lixin, C.; Jiehui, Y. A New Treated Surface for Achieving Dropwsie Condensation. *Enhanc. Heat Transf.* **1998**, *5*, 1–8.

(71) Kumagai, S.; Tanaka, S.; Katsuda, H.; Shimada, R. On the Enhancement of Filmwise Condensation Heat Transfer By Means of the Coexistence With Dropwise Condensation Sections. *Exp. Heat Transf.* **1991**, *4* (1), 71–82.

(72) Cassie, B. D.; Baxter, S. Wettability Of Porous Surfaces. *Trans. Farad. Soc* **1944**, *5*, 546–551.

(73) Narhe, R. D.; Beysens, D. A. Nucleation and Growth on a Superhydrophobic Grooved Surface. *Phys. Rev. Lett.* **2004**, *93* (7), 1–4.

(74) Chen, C. H.; Cai, Q.; Tsai, C.; Chen, C. L.; Xiong, G.; Yu, Y.; Ren, Z. Dropwise Condensation on Superhydrophobic Surfaces with Two-Tier Roughness. *Appl. Phys. Lett.* **2007**, *90* (17), 1–4.

(75) Jung, Y. C.; Bhushan, B. Wetting Behaviour during Evaporation and Condensation of Water Microdroplets on Superhydrophobic Patterned Surfaces. *J. Microsc.* **2008**, *229* (1), 127–140.

(76) Boreyko, J. B.; Chen, C. H. Self-Propelled Dropwise Condensate on Superhydrophobic Surfaces. *Phys. Rev. Lett.* **2009**, *103* (18), 2–5.

(77) Zheng, Y.; Han, D.; Zhai, J.; Jiang, L. In Situ Investigation on Dynamic Suspending of Microdroplet on Lotus Leaf and Gradient of Wettable Micro- and Nanostructure from Water Condensation. *Appl. Phys. Lett.* **2008**, *92* (8), 31–34.

(78) Patankar, N. a. Supernucleating Surfaces for Nucleate Boiling and Dropwise Condensation Heat Transfer. *Soft Matter* **2010**, *6* (8), 1613.

(79) Rykaczewski, K.; Scott, J. H. J.; Fedorov, a. G. Electron Beam Heating Effects during Environmental Scanning Electron Microscopy Imaging of Water Condensation on Superhydrophobic Surfaces. *Appl. Phys. Lett.* **2011**, *98* (9), 10–13.

(80) Rykaczewski, K.; Scott, J. H. J. Methodology for Imaging Nano-to-Microscale Water Condensation Dynamics on Complex Nanostructures. *ACS Nano* **2011**, *5* (7), 5962–5968.

(81) Rykaczewski, K.; Scott, J. H. J.; Rajauria, S.; Chinn, J.; Chinn, A. M.; Jones, W. Three Dimensional Aspects of Droplet Coalescence during Dropwise Condensation on Superhydrophobic Surfaces. *Soft Matter* **2011**, *7* (19), 8749.

(82) Rykaczewski, K.; Osborn, W. a.; Chinn, J.; Walker, M. L.; Scott, J. H. J.; Jones, W.; Hao, C.; Yao, S.; Wang, Z. How Nanorough Is Rough Enough to Make a Surface Superhydrophobic during Water Condensation? *Soft Matter* **2012**, *8* (33), 8786.

(83) Rykaczewski, K. Microdroplet Growth Mechanism during Water Condensation on Superhydrophobic Surfaces. *Langmuir* **2012**, *28* (20), 7720–7729.

(84) Miljkovic, N.; Enright, R.; Wang, E. N. ARTICLE E Ff Ect of Droplet Morphology on Growth Dynamics and Heat Transfer during Condensation on Superhydrophobic Nanostructured Surfaces. *ACS Nano* **2012**, *6* (2), 1776–1785.

(85) Miljkovic, N.; Enright, R.; Nam, Y.; Lopez, K.; Dou, N.; Sack, J.; Wang, E. N. Jumping-Droplet-Enhanced Condensation on Scalable Superhydrophobic Nanostructured Surfaces. *Nano Lett.* **2013**, *13* (1), 179–187.

(86) Wier, K. A.; McCarthy, T. J. Condensation on Ultrahydrophobic Surfaces and Its Effect on Droplet Mobility: Ultrahydrophobic Surfaces Are Not Always Water Repellant. *Langmuir* **2006**, *22* (6), 2433–2436.

(87) Dorrer, C.; Rühe, J. Condensation and Wetting Transitions on Microstructured Ultrahydrophobic Surfaces. *Langmuir* **2007**, *23* (7), 3820–3824.

(88) Mockenhaupt, B.; Ensikat, H. J.; Spaeth, M.; Barthlott, W. Superhydrophobicity of Biological and Technical Surfaces under Moisture Condensation: Stability in Relation to Surface Structure. *Langmuir* **2008**, *24* (23), 13591–13597.

(89) Torresin, D.; Tiwari, M. K.; Del Col, D.; Poulikakos, D. Flow Condensation on Copper-Based Nanotextured Superhydrophobic Surfaces. *Langmuir* **2013**, *29* (2), 840–848.

(90) Chawla, K. K.; Chawla, N. *Metal-Matrix Composites*; Springer: New York, 2004.

(91) Park, H.; Russell, T. P.; Park, S. Spatial Control of Dewetting: Highly Ordered Teflon Nanospheres. *J. Colloid Interface Sci.* **2010**, *348* (2), 416–423.

(92) Gao, L.; McCarthy, T. J. "Artificial Lotus Leaf" prepared Using a 1945 Patent and a Commercial Textile. *Langmuir* **2006**, *22* (14), 5998–6000.

(93) Extrand, C. W. Contact Angles and Hysteresis on Surfaces with Chemically Heterogeneous Islands. *Langmuir* **2003**, *19* (9), 3793–3796.

(94) Viovy, J. L.; Beysens, D.; Knobler, C. M. Scaling Description for the Growth of Condensation Patterns on Surfaces. *Phys. Rev. A* **1988**, *37 (12)*, 4965.

(95) Narhe, R.; Beysens, D.; Nikolayev, V. S. Contact Line Dynamics in Drop Coalescence and Spreading. *Langmuir* **2004**, *20* (4), 1213–1221.

(96) Damle, V. G.; Sun, X.; Rykaczewski, K. Can Metal Matrix-Hydrophobic Nanoparticle Composites Enhance Water Condensation by Promoting the Dropwise Mode? *Adv. Mater. Interfaces* **2015**, *2 (16)*, 1500202.

(97) Kim, S.; Kim, K. J. Dropwise Condensation Modeling Suitable for Superhydrophobic Surfaces. *J. Heat Transfer* **2011**, *133* (8), 81502.

(98) Incropera F. P.; DeWitt D. P.; *Fundamentals of Heat and Mass Transfer* , John Wiley & Sons , New York 2002.

(99) Song, C.; Wang, P.; Makse, H. a. A Phase Diagram for Jammed Matter. *Nature* **2008**, *453* (7195), 629–632.

(100) Hu, H.; Yu, S.; Song, D. No-Loss Transportation of Water Droplets by Patterning a Desired Hydrophobic Path on a Superhydrophobic Surface. *Langmuir* **2016**, *32* (29), 7339–7345.

(101) Bliznyuk, O.; Jansen, H. P.; Kooij, E. S.; Zandvliet, H. J. W.; Poelsema, B. Smart Design of Stripe-Patterned Gradient Surfaces to Control Droplet Motion. *Langmuir* **2011**, *27* (17), 11238–11245.

(102) Kooij, E. S.; Jansen, H. P.; Bliznyuk, O.; Poelsema, B.; Zandvliet, H. J. W. Directional Wetting on Chemically Patterned Substrates. *Colloids Surfaces A Physicochem. Eng. Asp.* **2012**, *413*, 328–333.

(103) Shanahan, M. E. R. Simple Theory of Stick-Slip Wetting Hysteresis. *Langmuir* **1995**, *11* (3), 1041–1043.

(104) Qin, D.; Xia, Y.; Whitesides, G. M. Soft Lithography for Micro- and Nanoscale Patterning. *Nat. Protoc.* **2010**, *5* (3), 491–502.

(105) Jansen, H. P.; Bliznyuk, O.; Kooij, E. S.; Poelsema, B.; Zandvliet, H. J. W. Simulating Anisotropic Droplet Shapes on Chemically Striped Patterned Surfaces. *Langmuir* **2012**, *28* (1), 499–505.

(106) Bliznyuk, O.; Vereshchagina, E.; Kooij, E. S.; Poelsema, B. Scaling of Anisotropic Droplet Shapes on Chemically Stripe-Patterned Surfaces. *Phys. Rev. E* **2009**, *79* (4), 1–6.

(107) Xia, D.; Brueck, S. R. J. Strongly Anisotropic Wetting on Surfaces 2008. *Nano Lett.* **2008**, *8* (9), 2819–2824.

(108) Chen, Y.; He, B.; Lee, J.; Patankar, N. A. Anisotropy in the Wetting of Rough Surfaces. *J. Colloid Interface Sci.* **2005**, *281* (2), 458–464.

(109) Zhao, Y.; Lu, Q.; Li, M.; Li, X. Anisotropic Wetting Characteristics on Submicrometer-Scale Periodic Grooved Surface. *Langmuir* **2007**, *23* (11), 6212–6217.

(110) Furuta, T.; Sakai, M.; Isobe, T.; Matsushita, S.; Nakajima, A. Sliding of Water Droplets on Hydrophobic Surfaces with Various Hydrophilic Region Sizes. *Langmuir* **2011**, *27* (11), 7307–7313.

(111) Wu, J.; Xia, J.; Lei, W.; Wang, B. P. Pinning Mechanism of Advancing Sessile Droplet on Superhydrophobic Surfaces. *RSC Adv.* **2014**, *4* (67), 35649–35652.

(112) Bliznyuk, O.; Jansen, H. P.; Kooij, E. S.; Poelsema, B. Initial Spreading Kinetics of High-Viscosity Droplets on Anisotropic Surfaces. *Langmuir* **2010**, *26* (9), 6328–6334.

(113) Kusumaatmaja, H.; Vrancken, R. J.; Bastiaansen, C. W. M.; Yeomans, J. M. Anisotropic Drop Morphologies on Corrugated Surfaces. *Langmuir* **2008**, *24* (14), 7299–7308.

(114) Wang, X.-P.; Qian, T.; Sheng, P. Moving Contact Line on Chemically Patterned Surfaces. *J. Fluid Mech.* **2008**, *605*, 59–78.

(115) Gore, R. W.; Allen, S. B. Waterproof Laminate. US Patent 4,194,041, 1980.

(116) Zhang, J.; France, P.; Radomyselskiy, A.; Datta, S.; Zhao, J.; Van Ooij, W. Hydrophobic Cotton Fabric Coated by a Thin Nanoparticle Plasma Film. *J. Appl. Polym. Sci.* **2003**, *88* (6), 1473–1481.

(117) Lau, K. K. S.; Bico, J.; Teo, K. B. K.; Chhowalla, M.; Amaratunga, G. a J.; Milne, W. I.; McKinley, G. H.; Gleason, K. K. Superhydrophobic Carbon Nanotube Forests. *Nano Lett.* **2003**, *3* (12), 1701–1705.

(118) Ma, M.; Gupta, M.; Li, Z.; Zhai, L.; Gleason, K. K.; Cohen, R. E.; Rubner, M. F.; Rutledge, G. C. Decorated Electrospun Fibers Exhibiting Superhydrophobicity. *Adv. Mater.* **2007**, *19* (2), 255–259.

(119) Ma, M.; Mao, Y.; Gupta, M.; Gleason, K. K.; Rutledge, G. C. Superhydrophobic Fibers Produced by Electrospinning and Chemical Vapor Deposition. *Macromolecules* **2005**, *38*, 9742–9748.

(120) Zimmermann, J.; Reifler, F. a.; Fortunato, G.; Gerhardt, L. C.; Seeger, S. A Simple, One-Step Approach to Durable and Robust Superhydrophobic Textiles. *Adv. Funct. Mater.* **2008**, *18* (22), 3662–3669.

(121) Wang, T.; Hu, X.; Dong, S. A General Route to Transform Normal Hydrophilic Cloths into Superhydrophobic Surfaces. *Chem. Commun.* **2007**, *18*, 1849–1851.

(122) Daoud, W. a; Xin, J. H.; Tao, X. Superhydrophobic Silica Nanocomposite Coating by a Low-Temperature Process. *J. Am. Ceram. Soc.* **2004**, *87* (9), 1782–1784.

(123) Yu, M.; Gu, G.; Meng, W. D.; Qing, F. L. Superhydrophobic Cotton Fabric Coating Based on a Complex Layer of Silica Nanoparticles and Perfluorooctylated Quaternary Ammonium Silane Coupling Agent. *Appl. Surf. Sci.* **2007**, *253* (7), 3669–3673.

(124) Lafuma, A.; Quéré, D. Superhydrophobic States. *Nat. Mater.* **2003**, *2* (7), 457–460.

(125) Hoefnagels, H. F.; Wu, D.; De With, G.; Ming, W. Biomimetic Superhydrophobic and Highly Oleophobic Cotton Textiles. *Langmuir* **2007**, *23* (26), 13158–13163.

(126) Han, D.; Steckl, A. J. Superhydrophobic and Oleophobic Fibers by Coaxial Electrospinning. *Langmuir* **2009**, *25* (16), 9454–9462.

(127) Choi, W.; Tuteja, A.; Chhatre, S.; Mabry, J. M.; Cohen, R. E.; McKinley, G. H. Fabrics with Tunable Oleophobicity. *Adv. Mater.* **2009**, *21* (21), 2190–2195.

(128) Jung, Y. C.; Bhushan, B. Wetting Behavior of Water and Oil Droplets in Three-Phase Interfaces for Hydrophobicity/philicity and Oleophobicity/philicity. *Langmuir* **2009**, *25* (24), 14165–14173.

(129) Srinivasan, S.; Chhatre, S. S.; Mabry, J. M.; Cohen, R. E.; McKinley, G. H. Solution Spraying of Poly(methyl Methacrylate) Blends to Fabricate Microtextured, Superoleophobic Surfaces. *Polymer* **2011**, *52* (14), 3209–3218.

(130) Kota, A. K.; Kwon, G.; Tuteja, A. The Design and Applications of Superomniphobic Surfaces. *NPG Asia Mater.* **2014**, *6* (7), e109.

(131) Lafuma, a.; Quéré, D. Slippery Pre-Suffused Surfaces. *Europhys. Lett.* **2011**, *96* (5), 56001.

(132) Yao, X.; Hu, Y.; Grinthal, A.; Wong, T.-S.; Mahadevan, L.; Aizenberg, J. Adaptive Fluid-Infused Porous Films with Tunable Transparency and Wettability. *Nat. Mater.* **2013**, *12* (6), 529–534.

(133) Kim, P.; Kreder, M. J.; Alvarenga, J.; Aizenberg, J. Hierarchical or Not ? Effect of the Length Scale and Hierarchy of the Surface Roughness on Omniphobicity of Lubricant-Infused Substrates *Nano Lett.* **2013**, *13*, 1793–1799.

(134) Lalia, B. S.; Anand, S.; Varanasi, K. K.; Hashaikeh, R. Fog-Harvesting Potential of Lubricant-Impregnated Electrospun Nanomats. *Langmuir* **2013**, *29* (42), 13081–13088.

(135) Kim, P.; Wong, T. S.; Alvarenga, J.; Kreder, M. J.; Adorno-Martinez, W. E.; Aizenberg, J. Liquid-Infused Nanostructured Surfaces with Extreme Anti-Ice and Anti-Frost Performance. *ACS Nano* **2012**, *6* (8), 6569–6577.

(136) Rykaczewski, K.; Anand, S.; Subramanyam, S. B.; Varanasi, K. K. Mechanism of Frost Formation on Lubricant-Impregnated Surfaces. *Langmuir* **2013**, *29* (17), 5230–5238.

(137) Wilson, P. W.; Lu, W.; Xu, H.; Kim, P.; Kreder, M. J.; Alvarenga, J.; Aizenberg, J. Inhibition of Ice Nucleation by Slippery Liquid-Infused Porous Surfaces (SLIPS). *Phys. Chem. Chem. Phys.* **2013**, *15* (2), 581–585.

(138) Subramanyam, S. B.; Rykaczewski, K.; Varanasi, K. K. Ice Adhesion on Lubricant-Impregnated Textured Surfaces. *Langmuir* **2013**, *29* (44), 13414–13418.

(139) Zhu, L.; Xue, J.; Wang, Y.; Chen, Q.; Ding, J.; Wang, Q. Ice-Phobic Coatings Based on Silicon-Oil-Infused Polydimethylsiloxane. *ACS Appl. Mater. Interfaces* **2013**, 5, 4053–4062.

(140) Epstein, a. K.; Wong, T.-S.; Belisle, R. a.; Boggs, E. M.; Aizenberg, J. From the Cover: Liquid-Infused Structured Surfaces with Exceptional Anti-Biofouling Performance. *Proc. Natl. Acad. Sci.* **2012**, *109* (33), 13182–13187.

(141) Howell, C.; Vu, T. L.; Lin, J. J.; Kolle, S.; Juthani, N.; Watson, E.; Weaver, J. C.; Alvarenga, J.; Aizenberg, J. Self-Replenishing Vascularized Fouling-Release Surfaces. *ACS Appl. Mater. Interfaces* **2014**, *6*, 13299–13307.

(142) Subramanyam, S.; Azimi, G.; Varanasi, K. Designing Lubricant-Impregnated Textured Surfaces to Resist Scale Formation. *Adv. Mater. Interfaces* **2014**, *1* (2), 1300068.

(143) Solomon, B.; Khalil, K.; Varanasi, K. Lubricant-Impregnated Surfaces for Drag Reduction in Viscous Laminar Flow. *Langmuir* **2014**, *30*, 10970–10976.

(144) Eifert, A.; Paulssen, D.; Varanakkottu, S. N.; Baier, T.; Hardt, S. Simple Fabrication of Robust Water-Repellent Surfaces with Low Contact-Angle Hysteresis Based on Impregnation. *Adv. Mater. Interfaces* **2014**, *1*, 1300138.

(145) Lee, C.; Kim, H.; Nam, Y. Drop Impact Dynamics on Oil-Infused Nanostructured Surfaces. *Langmuir* **2014**, *30* (28), 8400–8407.

(146) Carlson, a.; Kim, P.; Amberg, G.; Stone, H. a. Short and Long Time Drop Dynamics on Lubricated Substrates. *Europhys. Lett.* **2013**, *104* (3), 34008.

(147) Khalil, K. S.; Mahmoudi, S. R.; Abu-Dheir, N.; Varanasi, K. K. Active Surfaces: Ferrofluid-Impregnated Surfaces for Active Manipulation of Droplets. *Appl. Phys. Lett.* **2014**, *105* (4), 41604.

(148) Boreyko, J. B.; Polizos, G.; Datskos, P. G.; Sarles, S. a; Collier, C. P. Air-Stable Droplet Interface Bilayers on Oil-Infused Surfaces. *Proc. Natl. Acad. Sci. U. S. A.* **2014**, *111* (21), 7588–7593.

(149) Mruetusatorn, P.; Boreyko, J. B.; Venkatesan, G. a; Sarles, S. a; Hayes, D. G.; Collier, C. P. Dynamic Morphologies of Microscale Droplet Interface Bilayers. *Soft Matter* **2014**, *10* (15), 2530–2538.

(150) Shillingford, C.; MacCallum, N.; Wong, T.-S.; Kim, P.; Aizenberg, J. Fabrics Coated with Lubricated Nanostructures Display Robust Omniphobicity. *Nanotechnology* **2014**, *25* (1), 14019.

(151) Damle, V. G.; Tummala, A.; Chandrashekar, S.; Kido, C.; Roopesh, A.; Sun, X.; Doudrick, K.; Chinn, J.; Lee, J. R.; Burgin, T. P.; Rykaczewski, K. "Insensitive" to Touch: Fabric-Supported Lubricant-Swollen Polymeric Films for Omniphobic Personal Protective Gear. *ACS Appl. Mater. Interfaces* **2015**, *7* (7), 4224–4232.

(152) Chinn, J.; Helmrich, F.; Guenther, R.; Wiltse, M.; Hurst, K.; Ashurst, Robert, W.; Park, M. Durable Super-Hydrophobic Nano-Composite Films. *NSTI-Nanotech* **2010**, *1*, 612–615.

(153) Milne, A. Anti-Fouling Marine Compositions. US Patent 4,025,693, 1977.

(154) Edwards, D. P.; Nevell, T. G.; Plunkett, B. a.; Ochiltree, B. C. Resistance to Marine Fouling of Elastomeric Coatings of Some Poly(dimethylsiloxanes) and Poly(dimethyldiphenylsiloxanes). *Int. Biodeterior. Biodegradation* **1994**, *34* (3–4), 349–359.

(155) Nevell, T. G.; Edwards, D. P.; Davis, a J.; Pullin, R. a. The Surface Properties of Silicone Elastomers Exposed to Seawater. *Biofouling* **1996**, *10* (1–3), 199–212.

(156) Truby, K.; Wood, C.; Stein, J.; Cella, J.; Carpenter, J.; Kavanagh, C.; Swain, G.; Wiebe, D.; Lapota, D.; Meyer, A.; Holm, E.; Wendt, D.; Smith, C.; Montemarano, J. Evaluation of the Performance Enhancement of Silicone Biofouling-release Coatings by Oil Incorporation. *Biofouling* **2000**, *15* (1–3), 141–150.

(157) Kavanagh, C. J.; Swain, G. W.; Kovach, B. S.; Stein, J.; Darkangelo-Wood, C.; Truby, K.; Holm, E.; Montemarano, J.; Meyer, A.; Wiebe, D. The Effects of Silicone Fluid Additives and Silicone Elastomer Matrices on Barnacle Adhesion Strength. *Biofouling* **2003**, *19* (6), 381–390.

(158) MacCallum, N.; Howell, C.; Kim, P.; Sun, D.; Friedlander, R.; Ranisau, J.; Ahanotu, O.; Lin, J. J.; Vena, A.; Hatton, B.; Wong, T.-S.; Aizenberg, J. Liquid-Infused Silicone As a Biofouling-Free Medical Material. *ACS Biomater. Sci. Eng.* **2015**, *1* (1), 43–51.

(159) Callow, M. E.; Pitchers, R.; Santos, R. *In Biodeterioration 7*; Springer, 1988.

(160) Rice, S. L.; Diaz, A. F.; Minor, J. C.; Perry, P. A. Absorption of Silicone Oil by a Dimethylsiloxane Elastomer. *Rubber Chem. Technol.* **1988**, *61* (2), 194–204.

(161) Verbraecken, J.; Van De Heyning, P.; De Backer, W.; Van Gaal, L. Body Surface Area in Normal-Weight, Overweight, and Obese Adults. A Comparison Study. *Metabolism.* **2006**, *55* (4), 515–524.

(162) Ono, T.; Sugimoto, T.; Shinkai, S.; Sada, K. Molecular Design of Superabsorbent Polymers for Organic Solvents by Crosslinked Lipophilic Polyelectrolytes. *Adv. Funct. Mater.* **2008**, *18* (24), 3936–3940.

(163) Xiao, L.; Li, J.; Mieszkin, S.; Di Fino, A.; Clare, A. S.; Callow, M. E.; Callow, J. A.; Grunze, M.; Rosenhahn, A.; Levkin, P. A. Slippery Liquid-Infused Porous Surfaces Showing Marine Antibiofouling Properties. *ACS Appl. Mater. Interfaces* **2013**, *5* (20), 10074–10080.

(164) Manna, U.; Lynn, D. M. Fabrication of Liquid-Infused Surfaces Using Reactive Polymer Multilayers: Principles for Manipulating the Behaviors and Mobilities of Aqueous Fluids on Slippery Liquid Interfaces. *Adv. Mater.* **2015**, *27* (19), 3007–3012.

(165) Li, J.; Kleintschek, T.; Rieder, A.; Cheng, Y.; Baumbach, T.; Obst, U.; Schwartz, T.; Levkin, P. A. Hydrophobic Liquid-Infused Porous Polymer Surfaces for Antibacterial Applications. *ACS Appl. Mater. Interfaces* **2013**, *5* (14), 6704–6711.

(166) Charpentier, T. V. J.; Neville, A.; Baudin, S.; Smith, M. J.; Euvrard, M.; Bell, A.; Wang, C.; Barker, R. Liquid Infused Porous Surfaces for Mineral Fouling Mitigation. *J. Colloid Interface Sci.* **2015**, *444*, 81–86.

(167) Manabe, K.; Kyung, K. H.; Shiratori, S. Biocompatible Slippery Fluid-Infused Films Composed of Chitosan and Alginate via Layer-by-Layer Self-Assembly and Their Antithrombogenicity. *ACS Appl. Mater. Interfaces* **2015**, *7* (8), 4763–4771.

(168) Qiu, R.; Zhang, Q.; Wang, P.; Jiang, L.; Hou, J.; Guo, W.; Zhang, H. Fabrication of Slippery Liquid-Infused Porous Surface Based on Carbon Fiber with Enhanced Corrosion Inhibition Property. *Colloids Surfaces A Physicochem. Eng. Asp.* **2014**, *453* (1), 132–141.

(169) Yang, S.; Qiu, R.; Song, H.; Wang, P.; Shi, Z.; Wang, Y. Slippery Liquid-Infused Porous Surface Based on Perfluorinated Lubricant/iron Tetradecanoate: Preparation and Corrosion Protection Application. *Appl. Surf. Sci.* **2015**, *328*, 491–500.

(170) Zhu, H.; Hou, J.; Qiu, R.; Zhao, J.; Xu, J. Perfluorinated Lubricant/ Polypyrrole Composite Material: Preparation and Corrosion Inhibition Application. *J. Appl. Polym. Sci.* **2014**, *131* (9), 1–9.

(171) Wang, P.; Lu, Z.; Zhang, D. Slippery Liquid-Infused Porous Surfaces Fabricated on Aluminum as a Barrier to Corrosion Induced by Sulfate Reducing Bacteria. *Corros. Sci.* **2015**, *93*, 159–166.

(172) Tao, P.; Shang, W.; Song, C.; Shen, Q.; Zhang, F.; Luo, Z.; Yi, N.; Zhang, D.; Deng, T. Bioinspired Engineering of Thermal Materials. *Adv. Mater.* **2015**, *27* (3), 428–463.

(173) Song, T.; Liu, Q.; Liu, J.; Yang, W.; Chen, R.; Jing, X.; Takahashi, K.; Wang, J. Fabrication of Super Slippery Sheet-Layered and Porous Anodic Aluminium Oxide Surfaces and Its Anticorrosion Property. *Appl. Surf. Sci.* **2015**, *355*, 495–501.

(174) Liu, Q.; Yang, Y.; Huang, M.; Zhou, Y.; Liu, Y.; Liang, X. Durability of a Lubricant-Infused Electrospray Silicon Rubber Surface as an Anti-Icing Coating. *Appl. Surf. Sci.* **2015**, *346*, 68–76.

(175) Howell, C.; Vu, T. L.; Johnson, C. P.; Hou, X.; Ahanotu, O.; Alvarenga, J.; Leslie, D. C.; Uzun, O.; Waterhouse, A.; Kim, P.; Super, M.; Aizenberg, M.; Ingber, D. E.; Aizenberg, J. Stability of Surface-Immobilized Lubricant Interfaces under Flow. *Chem. Mater.* **2015**, *27* (5), 1792–1800.

(176) Wexler, J. S.; Jacobi, I.; Stone, H. A. Shear-Driven Failure of Liquid-Infused Surfaces. *Phys. Rev. Lett.* **2015**, *114* (16), 1–5.

(177) Cui, J.; Daniel, D.; Grinthal, A.; Lin, K.; Aizenberg, J. Dynamic Polymer Systems with Self-Regulated Secretion for the Control of Surface Properties and Material Healing. *Nat. Mater.* **2015**, *14*, 790–795.

(178) Okada, I.; Shiratori, S. High-Transparency, Self-Standable Gel-SLIPS Fabricated by a Facile Nanoscale Phase Separation. *ACS Appl. Mater. Interfaces* **2014**, *6* (3), 1502–1508.

(179) Wei, Q.; Schlaich, C.; Prévost, S.; Schulz, A.; Böttcher, C.; Gradzielski, M.; Qi, Z.; Haag, R.; Schalley, C. A. Supramolecular Polymers as Surface Coatings: Rapid Fabrication of Healable Superhydrophobic and Slippery Surfaces. *Adv. Mater.* **2014**, *26* (43), 7358–7364.

(180) Chen, L.; Geissler, A.; Bonaccurso, E.; Zhang, K. Transparent Slippery Surfaces Made with Sustainable Porous Cellulose Lauroyl Ester Films. *ACS Appl. Mater. Interfaces* **2014**, *6* (9), 6969–6976.

(181) Bohn, H. F.; Federle, W. Insect Aquaplaning: Nepenthes Pitcher Plants Capture Prey with the Peristome, a Fully Wettable Water-Lubricated Anisotropic Surface. *Proc. Natl. Acad. Sci. U. S. A.* **2004**, *101* (39), 14138–14143.

(182) Okiishi, M.; Munson, B.; Young, D. *Fundamentals of Fluid Mechanics*; Wiley: Hoboken, NJ, USA, 2006.

(183) Liu, S.; Sun, X.; Hildreth, O. J.; Rykaczewski, K. Design and Characterization of a Single Channel Two-Liquid Capacitor and Its Application to Hyperelastic Strain Sensing. *Lab on Chip* **2015**, *15*, 1376–1384.

(184) Juchniewicz, M.; Stadnik, D.; Biesiada, K.; Olszyna, A.; Chudy, M.; Brzózka, Z.; Dybko, A. Porous Crosslinked PDMS-Microchannels Coatings. *Sensors Actuators, B Chem.* **2007**, *126* (1), 68–72.

(185) Zhu, X.; Wu, G.; Dong, R.; Chen, C.-M.; Yang, S. Capillarity Induced Instability in Responsive Hydrogel Membranes with Periodic Hole Array. *Soft Matter* **2012**, *8*, 8088-8093.

(186) Wu, G.; Xia, Y.; Yang, S. Buckling, Symmetry Breaking, and Cavitation in Periodically Micro-Structured Hydrogel Membranes. *Soft Matter* **2014**, *10* (9), 1392.

(187) Ryerson, C. C. Assessment of Superstructure Ice Protection as Applied to Offshore Oil Operations Safety: Problems, Hazards, Needs, and Potential Transfer Technologies. *Erdc/Crrel Tr-08-14;* US Army Corps of Engineers Engineer Research and Development Center, Hanover, NH, US, **2008**.